ON THE INVESTIGATION OF A NOVEL X-RAY IMAGING TECHNIQUE IN RADIATION ONCOLOGY

BENJAMIN JAMES COOPER

A thesis submitted to fulfil
the requirements for the degree of
Doctor of Philosophy
Faculty of Medicine
The University of Sydney

THE UNIVERSITY OF
SYDNEY

December 2018

Benjamin James Cooper: *On the investigation of a novel x-ray imaging technique in radiation oncology* , © December 2018

“All truths are easy to understand once they are discovered;
the point is to discover them.”

— Galileo Galilei

DECLARATION

I, Benjamin James Cooper, certify that this thesis is my own work and has not been submitted in any form for another degree or diploma at any university or other institute of tertiary education. Work that has been carried out with assistance from other researchers and students is acknowledged appropriately. Information derived from the published and unpublished work of others has been acknowledged in the text with a list of references given at the end of each chapter. Some chapters have been published in peer-reviewed journals and other chapters are under review for publication. These are noted in the *Publications* section following.

Sydney, Australia, December 2018

Benjamin James Cooper

ABSTRACT

Radiation therapy is indicated for nearly 50% of cancer patients in Australia. Radiation therapy requires accurate delivery of ionising radiation to the neoplastic tissue and pre-treatment *in situ* x-ray imaging plays an important role in meeting treatment accuracy requirements. Four dimensional cone-beam computed tomography (4D CBCT) is one such pre-treatment imaging technique that can help to visualise tumour target motion due to breathing at the time of radiation treatment delivery. Measuring and characterising the target motion can help to ensure highly accurate therapeutic x-ray beam delivery.

In this thesis, a novel pre-treatment x-ray imaging technique, called *Respiratory Triggered 4D cone-beam Computed Tomography* (RT 4D CBCT), is conceived and investigated. Specifically, the aim of this work is to progress the 4D CBCT imaging technology by investigating the use of a patient's breathing signal to improve and optimise the use of imaging radiation in 4D CBCT to facilitate the accurate delivery of radiation therapy.

These investigations are presented in three main studies:

1. Introduction to the concept of respiratory triggered four dimensional cone-beam computed tomography.

2. A simulation study exploring the behaviour of RT 4D CBCT using patient-measured respiratory data.

3. The experimental realisation of RT 4D CBCT working in a real-time acquisitions setting.

The major finding from this work is that RT 4D CBCT can provide target motion information with a 50% reduction in the x-ray imaging dose applied to the patient.

PUBLICATIONS

Chapter 3 is a book chapter for which I was primary author. It is entitled: "Motion Management in Stereotactic Body Radiation Therapy" to be published in the book: "Stereotactic Radiosurgery and Stereotactic Body Radiation Therapy: A Comprehensive Guide".

The following works have been published in peer-reviewed academic journals and form the major composition of chapters 4 and 5 within this thesis. My contribution to these publications is at least 80%.

Cooper, B. J., O'Brien, R. T., Balik, S., Hugo, G. D., and Keall, P. J. (2013). Respiratory triggered 4D cone-beam computed tomography: A novel method to reduce imaging dose. *Medical Physics*, **40**(4), 041901.

Cooper, B. J., O'Brien, R. T., Kipritidis, J., Shieh, C. C., and Keall, P. J. (2015). Quantifying the image quality and dose reduction of respiratory triggered 4D cone-beam computed tomography with patient-measured breathing. *Physics in Medicine and Biology*, **60**(24), 9493.

The following work is under review for publication with the journal *Physics in Medicine and Biology* (December 2018) and forms the major composition of chapter 6 within this thesis. My contribution to these publications is at least 80%.

Cooper, B. J., O'Brien R. T., Shieh C. C., and Keall, P. J. Real-time respiratory triggered four dimensional cone-beam CT halves imaging dose compared to

conventional 4D CBCT.

The following work has been published and is relevant to the body of work completed during this thesis and appears as an appendix. Although not the primary author, I am second author.

O'Brien, R. T., Cooper, B. J., Kipritidis, J., Shieh, C. C., and Keall, P. J. (2014). Respiratory motion guided four dimensional cone beam computed tomography: encompassing irregular breathing. *Physics in Medicine and Biology*, **59**(3), 579.

PRESENTATIONS

The presentations listed below have been presented as findings directly arising from or related to this thesis.

Cooper B. J. and Keall P. J., Improving Linear Accelerator based Gated Cone-beam Computed Tomography, *Canberra Health Annual Research Meeting (CHARM)*, Canberra, June 2011.

Cooper B. J., O'Brien R. T., and Keall P. J., Respiratory Signal Triggered 4D Cone-Beam Computed Tomography on a Linear Accelerator. *The American Association of Physicists in Medicine 54th Annual Meeting*, Charlotte, July 2012.

Cooper B. J., Reducing imaging dose in 4D Cone-beam Computed Tomography using patient respiratory signals. *Combined Scientific Meeting 2014 (invited speaker)*, Melbourne, September 2014.

Cooper B. J., O'Brien R. T., Shieh C. C., Keall P. J., Hack a linac: Saving on imaging dose for in-room 4D-CBCT. *Canberra Hospital Research Day 2018*, Canberra, May 2018.

ACKNOWLEDGEMENTS

Insanity is how one person described to me the idea of doing a part time PhD. Perhaps there is an element of truth in that. Along with that, there is a definite element of unrelenting curiosity that has kept me going with this PhD. Whatever this PhD might be, the fact that Paul Keall had returned to Australia after his North American adventures and that I had received a positive response from Paul, where I essentially invited myself to be his PhD student, certainly has a lot to do with it ...

Upon reflection, perhaps it was Paul who was crazy to take me on as such a long term part time PhD student! Thank you, Paul, for your patience with me for so very many years. Your teaching and guidance in how to do research has been unique and incredibly valued. To this day I still feel lucky that you have been my supervisor and mentor.

I've also had remarkable luck to have Ricky O'Brien as my other supervisor without whom I would not have gotten very far in getting my C# computer code to run. Not to mention that any time I needed help, Ricky would always come up with the goods.

Then there are all the Image X Institute folks (or Radiation Physics Lab folks back in the day) who have listened to my verbose presentations and/or discussions and have always offered useful feedback. I must especially thank Chun-Chien (Andy) Shieh and John Kipritidis who have given me great ideas, amazing help and suggestions over the course of the project.

I could not have done this PhD without the support of my employer, Canberra Health Services. The protected time given for my study has been an essential requirement that has allowed me to pursue this PhD. I also give my personal thanks

to Sean Geoghegan without whose incredible encouragement and support, I doubt I would ever have undertaken this doctorate.

The PhD roller-coaster ride has not just been my mine alone - I've taken Jo and my kids Hamish and Rowan along the journey too. Thanks Jo, Hamish and Rowan for coming along with me, for all the twists and turns, the highs and lows, and holding out right to the end of the ride. Your patience has been truly amazing!

Mike Dyer, perhaps my oldest friend, and embedded systems designer extraordinaire, thanks for your expert advice on the step-down and step-up circuit design I needed to get right when connecting to the X-ray generator control circuits.

CONTENTS

1 OVERVIEW OF THIS THESIS 1

2 LITERATURE REVIEW 3

2.1 Radiation as a clinical therapy 3

2.1.1 Radiobiology 4

2.2 Imaging in Radiation Therapy 8

2.2.1 Role of imaging in cancer diagnosis 8

2.2.2 The role of imaging in Radiation Therapy Treatment Planning 9

2.3 Motivation for this work 17

3 MOTION MANAGEMENT IN STEREOTACTIC BODY RADIATION THERAPY 22

4 RESPIRATORY TRIGGERED 4D CONE-BEAM COMPUTED TOMOGRAPHY: A NOVEL METHOD TO REDUCE IMAGING DOSE 70

5 QUANTIFYING THE IMAGE QUALITY AND DOSE REDUCTION OF RESPIRATORY TRIGGERED 4D CONE-BEAM COMPUTED TOMOGRAPHY WITH PATIENT-MEASURED BREATHING 80

6 REAL-TIME RESPIRATORY TRIGGERED FOUR DIMENSIONAL CONE-BEAM CT HALVES IMAGING DOSE COMPARED TO CONVENTIONAL 4D CBCT 102

7 CONCLUSION 120

7.1 Future Directions 122

8 APPENDIX 1 126

ACRONYMS

4D Four-dimensional

ABC Active Breathing Control

CBCT Cone-beam Computed Tomography

CT Computed Tomography

CTV Clinical Target Volume

DIBH Deep Inspiration Breath Hold

DRR Digitally Reconstructed Radiograph

EPID Electronic Portal Imaging Device

ERW Edge Response Width

FBCT Fan-beam Computed Tomography

FDK Feldkamp-Davis-Kress

FDG Fluoro Deoxy-Glucose

GTV Gross Tumour Volume

IGRT Image Guided Radiation Therapy

ITV Internal Target Volume

kV Kilovoltage

Linac Linear accelerator

MLC Multi Leaf Collimator

MRI Magnetic Resonance Imaging

MU Monitor Unit

MV Megavoltage

NTCP Normal Tissue Complication Probability

OAR Organ At Risk

PET Positron Emission Tomography

PTV Planning Treatment Volume

RMG Respiratory Motion Guided

RPM Real-time Position Management

RT Respiratory Triggered

RTTPS Radiation Therapy Treatment Planning System

SBRT Stereotactic Body Radiation Therapy

TCP Tumour Control Probability

VMAT Volumetric Modulated Arc Therapy

V20 Volume of tissue receiving 20 Gy

1

OVERVIEW OF THIS THESIS

This thesis is about the conception and development of a novel imaging technique, respiratory triggered four dimensional cone-beam computed tomography (RT 4D CBCT), and its place in the art of treating moving tumour targets with medical linear accelerators. This needs a bit of unpacking. *4D CBCT* is an x-ray imaging technique for visualising the three dimensional anatomy inside a patient and how it moves in time (the fourth dimension). This forms a kind of "movie" of how anatomy changes over the course of time. This is particularly useful when attempting to treat tumours in the lung or right below the diaphragm because it gives the treatment staff and doctors "eyes" to see they are going to hit the right target. The *RT* part makes use of a patient's respiratory signal - the rising and falling motion - to decide when to acquire x-ray images. This work investigates this RT 4D CBCT technique in detail.

I have undertaken this work as a part time PhD student - my professional job is as a radiation oncology medical physicist. As such, I have the benefit of having an understanding of the potential clinical application for improving the plight of cancer patients receiving radiation therapy, even just a small improvement, with the efforts of the work herein.

Chapter 2 is a literature review giving a historical perspective on radiation as a therapeutic agent in cancer, the central role that imaging plays in numerous aspects of radiation oncology, and the particular challenges that are posed when dealing with tumours that move, for e.g. in the lung, and how these challenges are motivation for this work.

Chapter 3 is a detailed review chapter focusing on tumour motion management in stereotactic body radiation therapy, particularly lung tumour motion.

Chapter 4 introduces the concept of respiratory triggered four dimensional cone-beam computed tomography.

Chapter 5 is a simulation study that further explores the behaviour of respiratory triggered four dimensional cone-beam computed tomography using patient-measured respiratory data.

Chapter 6 is the culmination of the project that builds on the previous two chapters where respiratory triggered four dimensional cone-beam computed tomography is experimentally realised, working in a real-time acquisitions setting.

Chapter 7 is the summary of the project findings. There is a discussion on possible future directions for next steps and further work.

Chapter 8 is an appendix containing a publication relevant to the body of work completed during this thesis for which I am second author.

2

LITERATURE REVIEW

Almost immediately following the discovery of x-ray radiation by Wilhelm Röntgen in 1895 (Röntgen, 1895), its use as a therapeutic agent for cancer treatment has been pursued. The earliest use of x-rays for treatment was reported by Emil Grubbé where he claimed "I was the first person to apply x-rays to pathologic lesions on living human subjects for therapeutic purposes" (Grubbé, 1933). Grubbé was a manufacturer of incandescent lamps, Geissler and Crookes' tubes but he was also an undergraduate medical student in Chicago's Hahnemann Medical College. On January 27, 1896, J. E. Gilman, a professor at Grubbé's college, suggested that x-rays might be used to treat cancer after seeing the erythema on Grubbé's hand from placing it in the x-ray beam. Grubbé quotes Gilman as saying "any physical agent capable of doing so much damage to normal cells and tissues might offer possibilities, if used as a therapeutic agent, in the treatment of pathologic conditions in which pronounced irritative, blistering, or even destructive effects might be desirable." (Grubbé, 1933). On January 28, 1896, Dr R. Ludlam, a colleague of Gilman's, referred a patient with carcinoma of the left breast to Grubbé for the application of x-rays (Grubbé, 1933), and with that, external beam radiation therapy was born.

2.1 RADIATION AS A CLINICAL THERAPY

Early European practitioners of radiation therapy, or "Röntgen Therapeutists" include Schiff, Freund, Béclére, and several others (MacKee, 1922) but Henri Coutard was instrumental to the progression of radiation therapy for his clinical observations of the cancerous and surrounding normal tissues during x-ray therapy. His work could be considered as a precursor to the field of radiobiology. Some of the salient observations he made (Coutard, 1934) include:

1. undifferentiated cancers (epitheliomas) generally responded well given total doses of 6000 r[1] to 8000 r over 30 to 40 days;

2. in treating differentiated epitheliomas, giving smaller daily doses (175, 200, 225, 250 r) over 30 up to 90 days preserved the non-cancerous vasculo-connective tissue and could obtain "disappearance of cancers which up to then we had considered radioresistant";

3. the two principal factors in x-ray therapy are the energy (dose) and the time;

4. the protective action to normal tissues by stretching out treatment time;

5. the "cure of cancer by x-rays" is difficult and dangerous;

6. sometimes a small margin exists between the dose which will determine a cure and the dose that will provoke an injury;

7. daily examination of the patient is necessary and that modification of the treatment regimen is often required.

It is remarkable that all of these observations are arguably still relevant to today's practice of radiation therapy.

2.1.1 Radiobiology

It is the primary goal of radiation therapy to maximise tumour cell death with as little normal tissue damage as possible. Understanding how x-ray energy affects both cancerous and normal healthy tissue is a necessary field of study in order to pursue this goal and improve patient outcomes - this field of study is termed radiobiology. It is likely that the earliest observations of the radiobiological effects of x-rays on cells came from the collective works of Albers-Schönberg, Bergonié ,

1 r denotes 1 rad which is 1 cGy

Regaud and Tribondeau which at the time significantly contributed to the knowledge of the biological response to radiation by studying the histological features of irradiated testes in numerous animal models (Vogin and Foray, 2013).

Radiobiology, the study of cellular response to radiation, has evolved since those early days with several models proposed. Perhaps the most enduring model, the *linear-quadratic (LQ) model* is a model of cell survival after exposure to radiation. Douglas and Fowler made a detailed study of the skin reactions in albino mice where the total x-ray dose, overall time, and number of fractions were varied in order to achieve a constant level of damage in normal tissue. (Douglas and Fowler, 1976).

A major result from this work is the equation for the cell survival:

$$S = e^{-(\alpha D+\beta D^2)} \tag{2.1}$$

where S is surviving fraction, D is total x-ray dose (units of Gy) and α and β are linear and quadratic constants (units of Gy^{-1} and Gy^{-2} respectively) which are characteristic of the cells in question - either normal cells or tumour cells.

It is regarded as the most commonly used model for quantitative predictions of dose / fractionation dependencies in radiotherapy (Brenner, 2008). Moreover, the surviving fraction (S) of tumour cells is a key term used in the formulation for tumour control probability (TCP). In its simplest form, the probability of gaining tumour "control", is given as:

$$TCP = (1-S)^N \tag{2.2}$$

where N is the number of clonogens, or tumour cells that have the capability to initiate tumour regrowth (Brenner, 1993).

For tumours, the β term in equation 2.1 can be neglected:

$$TCP = (1-e^{-(\alpha D)})^N \tag{2.3}$$

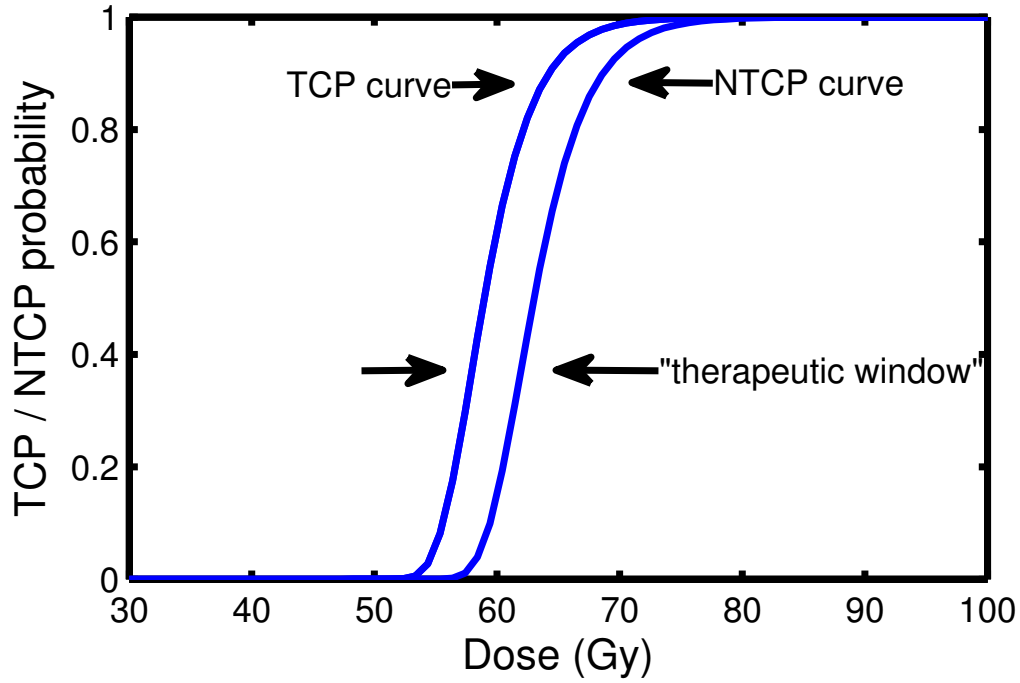

Figure 2.1: Example plot of Tumour Control Probability (TCP) and Normal Tissue Complication Probability (NTCP) versus x-ray dose (Gy).

For small S (we want a low survival of tumour cells) and re-writing the number of clonogens as a product of clonogen density ρ and tumour volume V, i.e. $N = \rho V$ (Webb and Nahum, 1993) :

$$1 - e^{-(\alpha D)} \approx \exp(-e^{-(\alpha D)}), \tag{2.4}$$

$$TCP = \exp(-e^{-(\alpha D)})^N \tag{2.5}$$

$$TCP = \exp(-\rho V e^{-(\alpha D)}) \tag{2.6}$$

This leads to an expression for tumour control probability as a function of clonogenic cell density ρ, tumour volume V, the tumour's characteristic "α", and total dose D. An example plot of the characteristic shape of a TCP versus D is shown (left, Figure 2.1), along with a typical Normal Tissue Complication probability (NTCP) versus D (right, Figure 2.1). It is clear that there is only a narrow "therapeutic window" of dose that can maximise probability of tumour control without causing a high probability of normal tissue complication or toxicity.

It might be tempting to think that one could solve equation 2.6 for D, assuming a TCP approaching 1, i. e. complete tumour control, and plugging in the tumour volume, clonogenic cell density, and the tumour's α value. Unfortunately, there are number of issues that complicate this including:

1. non-uniform clonogenic cell density;
2. non-uniform dose;
3. non-uniform α values for clonogens;
4. constraints on total tumour dose due to the toxicity limits of dose to surrounding normal tissues (NTCP).

Webb and Nahum mathematically modelled the effects of these items. A simple assumption was made where the clonogenic cell density falls off gradually towards zero density at the boundary of a model spherical tumour. A striking result is that even in the (theoretical) best case scenario where the density changes by several orders towards the boundary, the "dose may be safely reduced by only a few Gy" where the clonogens become less dense, and thus "it is absolutely vital that adequate margins are employed at the edge of the tumour" (Webb and Nahum, 1993).

Fractionation is where a tumourcidal dose - 60 Gy for example - is broken into a number of smaller sized dose fractions. A typical fractionation for this example might be 30 fractions that are delivered daily at a rate of 2 Gy per fraction. For different fractionation schemes, it can be useful to know what would be an equivalent dose effect delivered in infinitely small fractions: this is called the *biologically effective dose* or BED and can be defined mathematically (Fowler, 1989):

$$\mathrm{BED} = nd\left(1+\frac{d}{\alpha/\beta}\right) \tag{2.7}$$

where n is the number of fractions, d is the fractional dose, α and β are defined as previously (2.1).

2.2 IMAGING IN RADIATION THERAPY

Imaging is at the heart of radiation therapy for deep seated tumours. It is a critical pillar upon which nearly all modern radiation therapy relies. Imaging typically plays important roles: in diagnosis, in radiation treatment planning, in patient position set-up verification, and in motion management. The remainder of this section broadly discusses the role of imaging in diagnosis and treatment planning; the next section will discuss the role of imaging in patient position verification and motion management is discussed in Chapter 3 in detail.

2.2.1 Role of imaging in cancer diagnosis

During the course of medical investigations and diagnosis for most cancers, and almost certainly for all deep seated tumours, radiological imaging is essential to determine staging, topographical localisation, and extension of the disease into neighbouring tissues. More than any other treatment modality, radiotherapy relies directly on radiological imaging to acquire such data (Van den Berge et al., 2000). X-ray Computed Tomography (CT), Magnetic Resonance Imaging (MRI), Positron Emission Tomography (PET), and Single Photon Emission Tomography (SPECT) are the imaging techniques that are employed for cancer diagnosis and staging with CT being the most common.

The ability to "look inside" a patient, as if sliced like a loaf of bread, was realised with Hounsfield's invention of the CT scanner (Hounsfield, 1973). The CT machine acquires sets of images, or to extend the loaf of bread analogy, "slices", that are incrementally "cut" across the long axis of the patient, typically in the head-to-feet direction (see Figure 2.2).

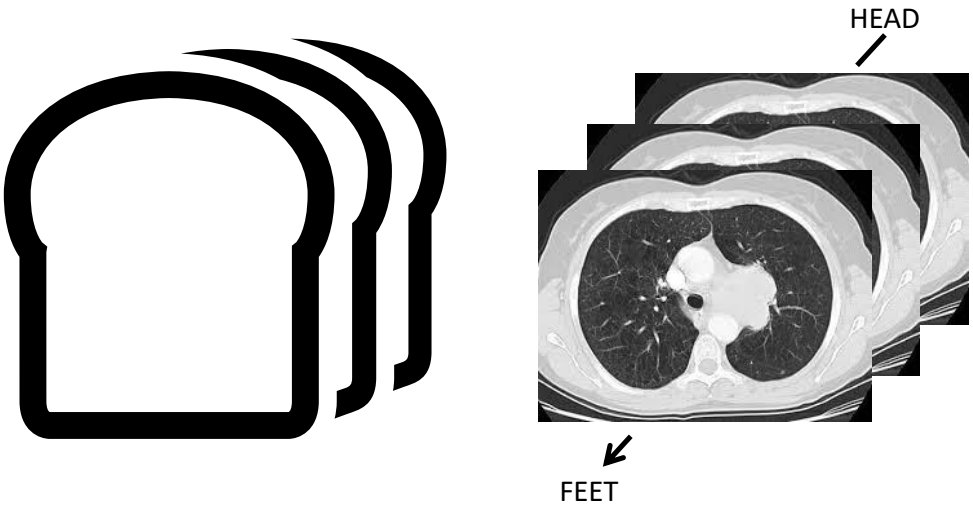

Figure 2.2: Like slices in a loaf of bread (left), a CT image set consists of image "slices" along the head-to-feet long axis of the body (right).

2.2.2 The role of imaging in Radiation Therapy Treatment Planning

Until the CT machine was invented, clinicians were not afforded the rich anatomical information resulting from CT and were restricted to planar x-ray images for anatomical based location of tumour regions. Not long after CT was invented, prospective studies into its use for tumour localisation for treatment planning in radiation therapy were initiated (Stanley et al., 1976). A study with 98 CT body scans of radiotherapy patients showed that the tumour could be delineated clearly (63%) or suggestive of tumour extent (33%) with only 4% of scans not showing the tumour. Additionally, 75 of the 98 scans revealed information leading to any one, or a combination of: changing treatment volumes; changes in acceptable irradiation of normal tissue; or changing treatment margins to improve coverage (Munzenrider et al., 1977). Similarly, Dobbs *et al.* reported that 33% of a 320 patient cohort had their treatment plans altered after comparing conventional tumour localisation with CT based tumour localisation (Dobbs et al., 1983). Another way to think about this is that without CT, the radiation oncologist is trying to "shoot in the dark".

Although not directly related to this thesis, it would be remiss not to mention MRI and FDG-PET. A 2009 survey of 394 radiation oncologists in the United States reported that when advanced imaging was required for delineation of tumours, FDG-PET and MRI were used at rates of 76% and 72% respectively (Simpson et al., 2009).

Historically, radiation therapy treatment planning utilised planar x-ray radiographs of the relevant clinical treatment site. From these images, the planned treatment beam dimensions and shapes were determined, often using nothing more than bony anatomical landmarks. There are several limitations with this approach:

1. Radiographs can essentially resolve skeletal bone with fairly poor resolution of soft tissue;

2. The 2D nature of a radiograph cannot reveal the complex 3D structure of potentially radio-sensitive organs and tissues close to the tumour;

3. Ability to refine the treatment plan (and potentially improve patient outcomes) is hampered by needing to "play it safe" with prescribed x-ray dose to avoid unwanted normal tissue damage.

With the emergence of the imaging capabilities from CT, a more detailed picture for tumour delineation and neighbouring radio-sensitive organs in treatment planning was realised. Another benefit from using CT was the opportunity for more accurate x-ray dosimetry modelling and calculation, taking into account tissue heterogeneities along the radiological path to the treatment volume (Webb, 1988).

2.2.2.1 *Treatment Planning*

Once it has been established that a patient is to receive radiation therapy, the current standard practice is for radiation oncology patients to have a treatment planning CT scan, in addition to any diagnostic radiological imaging. It is vital that the patient is positioned in the CT scanner in the same position as intended for the radiation treatment. The treatment planning CT scan is used directly

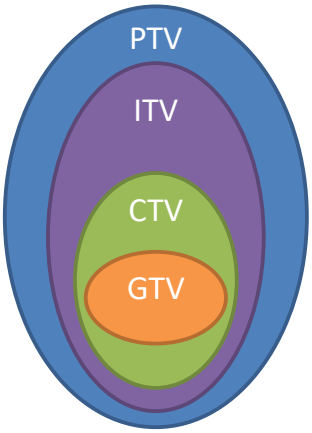

Figure 2.3: Schematic showing ICRU defined volumes and their relative sizes.

to build a computerised "virtual patient" model using specialised software packages called "radiation therapy treatment planning systems" (RTTPS). This virtual patient model allows the radiation oncologists and radiation therapists to "see inside" and visualise the tumour and its spatial relationship to all the surrounding tissues, organs, and anatomy.

2.2.2.2 *The problem of delineation and outlining - where's the tumour?*

Radiation oncology patients receive a treatment planning CT scan upon which radiation therapists and radiation oncologists must digitally "draw" the outline contour of the tumour, or treatment target, and any nearby radio-sensitive tissues and organs, termed *Organs at Risk* (OARs). The International Commission on Radiological Units (ICRU) define a naming convention for target outlines, or volumes as follows:

- GTV : Gross tumour volume
- CTV : Clinical target volume
- ITV : Internal target volume
- PTV : Planning target volume

These definitions (see Figure 2.3) have helped to standardise planning practices, but there are a number of problems. The purpose of the ITV is to simply add an internal margin encompassing the excursion of the CTV due to organ motion. Unfortunately for patients with tumours in the lower lobe of the lung, these excursions are in the order of 10 mm, and can be as high as 30 mm as reported by numerous investigators and summarised by Giraud who observed : " ... the addition of various geometric margins leads to irradiation of a large volume of healthy tissue, increasing the risk of complications, and therefore limiting the possibility of dose escalation" (Giraud and Houle, 2013). The imaging fidelity and quality of a CT scan relies on the assumption that the object being imaged is stationary. This assumption breaks down for thoracic scans of a free-breathing patient resulting in non-physical artefacts such as unattached and isolated portions of diaphragm extending into lung tissue with a jagged appearance. (Balter et al., 1996). The limitations of CT imaging have led to difficulties for radiation oncologists to outline lung tumour GTVs accurately. Inter-observer variability is where two or more clinicians outline a GTV on the same source CT image dataset. Jameson *et al.* studied the inter-observer variability in outlining a lung tumour and demonstrated some large variations in contours (Jameson et al., 2014). Without auto-contouring aids to guide the clinician in non-small-cell lung cancer, the inter-observer variability is higher (van Baardwijk et al., 2007). In the absence of supporting tools, FDG based PET-CT imaging sets, a suboptimal solution is to apply a population-based average safety margin to the CTV. This approach can limit the prescribed dose due to a higher volume of irradiated lung, also limiting the opportunity to escalate tumour dose that can lead to better patient outcomes (Machtay et al., 2012). Once target(s) (PTVs) have been "drawn" and defined by the clinician and radiation therapy planning team, the main function of the RTTPS is to facilitate the tailor-made design or treatment plan for a particular patient's disease; to model and visualise the x-ray dose distribution (energy deposition), often shown as a colourful overlay on top of the cross sectional anatomy from the CT image. In this way, it is possible to "try

out" different treatment plans (beam combinations) and to see how the x-ray dose will be distributed differently.

2.2.2.3 *4D CT : opportunities and challenges*

Just as Webb observed the "inability of plane radiography to visualise the tumour" (Webb, 1988), Hugo and Rosu stated that "it is now possible to deal with a '4D' model of the patient, consisting of three spatial dimensions plus time as the fourth dimension" (Hugo and Rosu, 2012). Just as the CT scanner unveiled a detailed three dimensional representation of the tumour and organs inside the patient, 4D CT adds the dimension of time to get time-resolved images of the more complex dynamics of a living, breathing patient. The basic idea of 4D CT is that the respiratory signal is recorded simultaneously with the scan acquisition such that a representative patient "breath" is acquired with the CT scanner, in effect adding a fourth dimension of time resolved images. The respiratory signal information informs the CT scanning system of the patient's respiratory phase during image acquisition. This method of 4D CT acquisition is termed *retrospective* as both the measured respiratory signal and attenuation sinogram are correlated and post-processed during the image reconstruction to produce the final 4D CT images. Much like playing back a movie, the 4D CT results in a short movie loop, or "cine", of one composite breathing cycle. Although the movie loop appears to be a single breath, it is in fact composed of many breaths acquired over the course of the scan, giving a kind of average breath. The movie loop is typically composed of 10 time sequenced image frames covering the full respiration cycle (breathe in, breathe out). There have been numerous pioneering efforts and implementations of respiratory based 4D CT and its use in radiation therapy (Ford et al., 2003; Low et al., 2003; Keall et al., 2004; Pan et al., 2004). One early implementation involved modifying a CT scanner that supported dynamic cardiac imaging and "tricking" the scanner into acquiring images based on a respiratory signal instead of an ECG (electro-cardiogram) signal (Keall et al., 2004). Respiratory signals may be supplied by a number of different methods (e.g. spirometry, pressure sensitive chest belts)

however the output signals from all methods ultimately represent the periodic motion of the lung as it expands and contracts over time. Varian[2] manufacture the *Real-time Position Management* (RPM) system which has been widely used for generating surrogate lung motion signals in the radiation oncology setting. RPM is a simple and non-invasive system employing an infra-red camera system tracking reflective marker dots placed on the patient's chest. There are limitations to this - mainly regarding that it is only a surrogate for lung motion, not a direct measurement. Nevertheless, the movements of the tumour as measured with the 4D CT is typically used for delineation of the ITV. Another use of the measured tumour motion data is to model the effect of respiratory motion directly in the dose calculations (Giraud and Houle, 2013) allowing estimations of the effects of respiratory motion on TCP and NTCP (McCarter and Beckham, 2000; Warkentin et al., 2004). Better spatio-temporal information about tumour motion is an essential step in efforts to improve and sharpen the radiation delivery to the tumour.

2.2.2.4 *4D CT : clinical benefits in lung radiation therapy*

Logic suggests that irradiating a lower volume of lung tissue lowers the chance of damaging healthy lung tissue, i.e. lowers NTCP. Evidence for this is shown by Marks *et al.* who summarised the probability of radiation pneumonitis, a type of lung injury from radiation therapy, versus mean lung dose from a wide range of clinical data sources. There is strong evidence that higher mean lung dose increases the chance of radiation pneumonitis. (Marks et al., 2010). Machtay *et al.* combined data from several trials and demonstrated that a 1 Gy increase in Biologically Equivalent Dose (BED) in radiotherapy gave a 4% statistically significant improvement in survival for locally advanced non-small-cell lung carcinoma (Machtay et al., 2012). To use Coutard's words again (Section 2.1): "[there exists] a small margin between the dose which will determine a cure and the dose that will provoke injury". In other words, there is a tension between giving a high dose to the tumour, associated with higher tumour cell kill and a better chance of patient survival, and

2 Varian Medical Systems, Inc. 3100 Hansen Way, Palo Alto, CA 94304-1038, USA

avoiding a higher overall mean lung dose which has a higher chance of lung injury. The clinical benefit of 4D CT is that lung cancer tumours moving due to respiratory motion can be measured and characterised when designing a treatment plan for lung cancer patients undergoing radiation therapy. 4D CT gives the clinician a better understanding of how lung tumour targets move during respiration. Remembering the result demonstrated by Webb and Nahum stating "it is absolutely vital that adequate margins are employed at the edge of the tumour" (Webb and Nahum, 1993), then knowing how the edge of the tumour moves with 4D CT is a critical step to better treatment planning striving for lower mean lung dose (lower chance of pneumonitis (Marks et al., 2010)) and or higher tumour dose (improved patient survival (Machtay et al., 2012)).

2.2.2.5 *The role of cone-beam CT during treatment*

Cone-beam computed tomography (CBCT) during treatment enables high precision image guided radiation therapy through its ability to produce superior relative spatial anatomical information compared to planar x-ray imaging. Similarly to conventional computed tomography (CT), in CBCT an x-ray source and detector system "orbits" around the object to be imaged, gathering x-ray projection attenuation information along the way which is later reconstructed into a CT slice (see Figure 2.4). CBCT differs from conventional CT in that the x-ray source is projected to create a cone of x-rays onto the area of the patient to be imaged, rather than a fan-beam as is used in conventional CT. For example, the gantry mounted imaging system on a linear accelerator might collect anywhere from 350 to 660 radiographs or "projections" in series during its arc around the patient to produce a CBCT dataset. This results in an imaging dose of 7.7 mGy for a low dose thorax protocol using about 670 projections (Kim et al., 2010). Figure 2.5 illustrates how a typical CBCT is acquired on a linear accelerator.

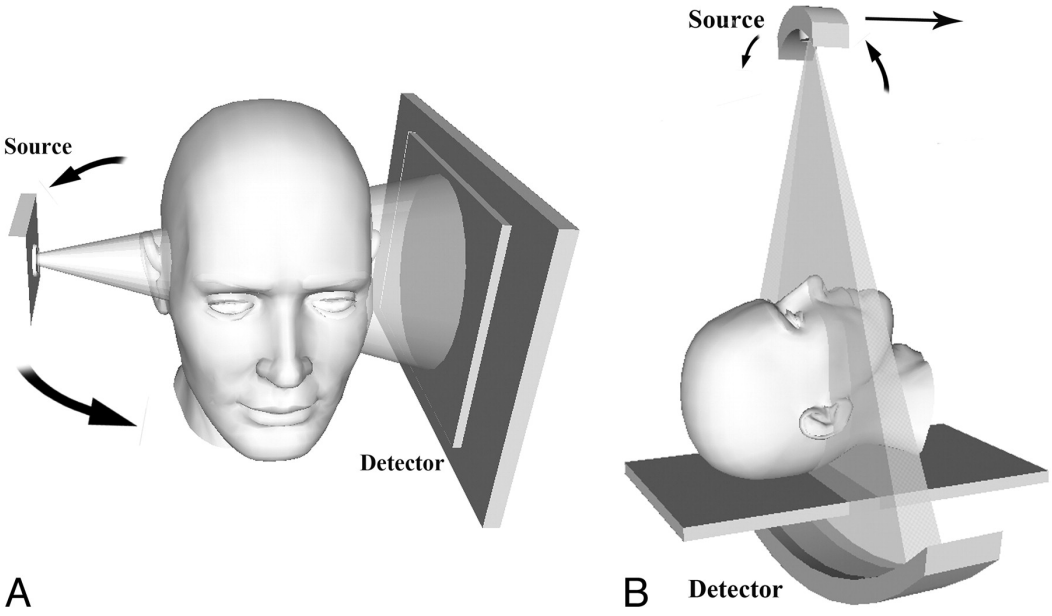

Figure 2.4: Cone-beam CT schematic (A) compared to conventional CT (B).
Image credit Miracle and Mukherji (2009)

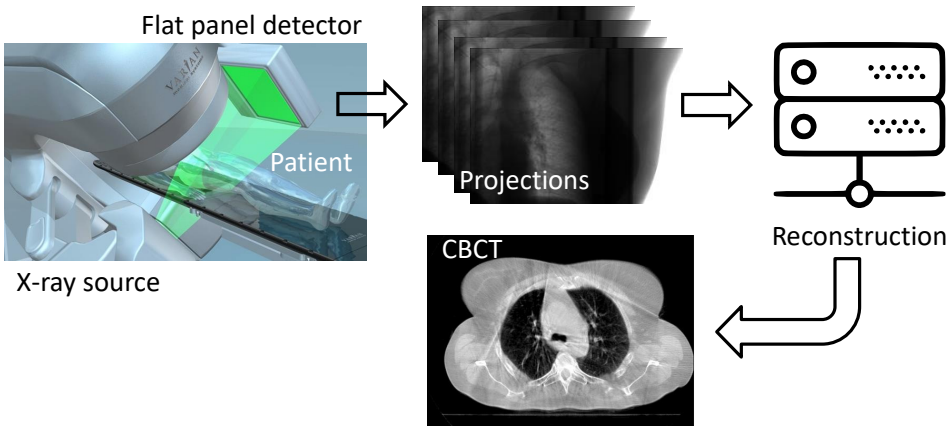

Figure 2.5: Cone-beam CT imaging acquisition.

2.2.2.6 *Four dimensional cone-beam CT*

Four dimensional cone-beam CT is analogous to 4D CT (see Section 2.2.2.4) but with some fundamental differences. Apart from the relatively large area x-ray field to produce the cone-beam projections, the angular velocity of the gantry mounted imaging system is restricted to only one revolution per minute. In contrast, the x-ray source – detector system in a modern CT scanner is capable of several revolutions per second. Nevertheless, 4D CBCT is used to ensure that the planned treatment will be delivered accurately, even with the added complication of treating a moving tumour target due to respiration. A detailed description of clinical 4D CBCT is given in Chapter 3. The imaging dose increases with 4D imaging: a typical thorax 4D CBCT might require up to 1320 projections, or roughly 15.2 mGy.

2.3 MOTIVATION FOR THIS WORK

Imaging is an essential component for accurate radiation treatment, both in the planning and treatment phase. 4D CBCT has an important role to play in pre-treatment verification of the extent of tumour motion due to respiration which is particularly important for hypo-fractionated SBRT lung radiation therapy (Benedict et al., 2010). The next chapter goes into some detail about motion management in radiation therapy and its particularly important role in lung radiation therapy.

Improving the dose efficiency of imaging x-ray exposure to patients in acquiring 4D CBCT image sets is a central motivation for this project. The established trend in radiation therapy is that as x-ray imaging improvements become available, the adoption of those technologies in standard treatment practices tends to grow (Simpson et al., 2010).

The rest of the thesis chapters describe a novel in-room 4D CBCT imaging technique, coined "Respiratory Triggered Four Dimensional Cone-beam Computed Tomography" (RT 4D CBCT): Chapter 4 is the hypothesis and concept; Chapter 5 is a detailed *in silico* study; and Chapter 6 is a working prototype of RT 4D CBCT.

These works investigate the possibilities of reducing patient x-ray imaging dose through the selective use of x-ray projections based on the patient's respiratory signal.

REFERENCES

Balter J M, Haken R K T, Lawrence T S, Lam K L and Robertson J M 1996 *International Journal of Radiation Oncology*Biology*Physics* **36**(1), 167 – 174.
URL: *http://www.sciencedirect.com/science/article/pii/S0360301696002751*

Benedict S H, Yenice K M, Followill D, Galvin J M, Hinson W, Kavanagh B, Keall P, Lovelock M, Meeks S and Papiez L 2010 *Medical physics* **37**(8), 4078–4101.

Brenner D J 1993 *International Journal of Radiation Oncology* Biology* Physics* **26**(1), 171–179.

Brenner D J 2008 *in* 'Seminars in radiation oncology' Vol. 18 Elsevier pp. 234–239.

Coutard H 1934 *The Lancet* **224**(5784), 1e1e25–48.

Dobbs H J, Parker R, Hodson N, Hobday P and Husband J E 1983 *Radiotherapy and oncology* **1**(2), 133–141.

Douglas B and Fowler J 1976 *Radiation research* **66**(2), 401–426.

Ford E C, Mageras G S, Yorke E and Ling C C 2003 *Medical Physics* **30**(1), 88.

Fowler J F 1989 *The British journal of radiology* **62**(740), 679–694.

Giraud P and Houle A 2013 *ISRN Pulmonology* **2013**.

Grubbé, Emil H 1933 *Radiology* **21**(2), 156–162.

Hounsfield G N 1973 *The British journal of radiology* **46**(552), 1016–1022.

Hugo G D and Rosu M 2012 *Zeitschrift für Medizinische Physik* **22**(4), 258–271.

Jameson M G, Kumar S, Vinod S K, Metcalfe P E and Holloway L C 2014 *Radiotherapy and Oncology* **112**(3), 332–336.

Keall P J, Starkschall G, Shukla H, Forster K M, Ortiz V, Stevens C W, Vedam S S, George R, Guerrero T and Mohan R 2004 *Phys Med Biol* **49**(10), 2053–2067.

Kim S, Yoo S, Yin F F, Samei E and Yoshizumi T 2010 *Medical Physics* **37**(7), 3648.

Low D A, Nystrom M, Kalinin E, Parikh P, Dempsey J F, Bradley J D, Mutic S, Wahab S H, Islam T, Christensen G et al. 2003 *Medical physics* **30**(6), 1254–1263.

Machtay M, Bae K, Movsas B, Paulus R, Gore E M, Komaki R, Albain K, Sause W T and Curran W J 2012 *International Journal of Radiation Oncology* Biology* Physics* **82**(1), 425–434.

MacKee G M 1922 *X Rays and Radium in the Treatment of Diseases of the Skin* The British Institute of Radiology.

Marks L B, Bentzen S M, Deasy J O, Kong F M S, Bradley J D, Vogelius I S, El Naqa I, Hubbs J L, Lebesque J V and Timmerman R D 2010 *International Journal of Radiation Oncology* Biology* Physics* **76**(3), S70–S76.

McCarter S and Beckham W 2000 *Physics in Medicine & Biology* **45**(4), 923.

Miracle A and Mukherji S 2009 *American Journal of Neuroradiology* **30**(6), 1088–1095.
URL: *http://www.ajnr.org/content/30/6/1088*

Munzenrider J E, Pilepich M, Rene-Ferrero J B, Tchakarova I and Carter B L 1977 *Cancer* **40**(1), 170–179.

Pan T, Lee T Y, Rietzel E and Chen G T 2004 *Medical physics* **31**(2), 333–340.

Röntgen W 1895 *Sitzungsber. Phys. Med. Gesell.* .

Simpson D R, Lawson J D, Nath S K, Rose B S, Mundt A J and Mell L K 2009 *Journal of the American College of Radiology* **6**(12), 876–883.

Simpson D R, Lawson J D, Nath S K, Rose B S, Mundt A J and Mell L K 2010 *Cancer* **116**(16), 3953–60.
URL: *http://www.ncbi.nlm.nih.gov/pubmed/20564090*

Stanley R, Sagel S S and Levitt R 1976 *American Journal of Roentgenology* **127**(1), 53–67.

van Baardwijk A, Bosmans G, Boersma L, Buijsen J, Wanders S, Hochstenbag M, van Suylen R J, Dekker A, Dehing-Oberije C, Houben R, Bentzen S M, van Kroonenburgh M, Lambin P and De Ruysscher D 2007 *Int J Radiat Oncol Biol Phys* **68**(3), 771–8.
URL: *https://www.ncbi.nlm.nih.gov/pubmed/17398018*

Van den Berge D L, De Ridder M and Storme G A 2000 *European journal of radiology* **36**(1), 41–48.

Vogin G and Foray N 2013 *International journal of radiation biology* **89**(1), 2–8.

Warkentin B, Stavrev P, Stavreva N, Field C and Fallone B G 2004 *Journal of Applied Clinical Medical Physics* **5**(1), 50–63.

Webb S 1988 *The physics of medical imaging* CRC Press.

Webb S and Nahum A 1993 *Physics in medicine and biology* **38**(6), 653.

3

MOTION MANAGEMENT IN STEREOTACTIC BODY RADIATION THERAPY

Motion management in radiation therapy is the focus of this chapter. The sources of motion, along with strategies to mitigate and detect motion is presented in detail. I was the lead and primary author of this review chapter (sections 1–4) with my co-authors listed below. The work presented will become a chapter in the book "Stereotactic Radiosurgery and Stereotactic Body Radiation Therapy: A Comprehensive Guide" to be published by Springer.

The co-authors are:
Rong, Y. and Keall, P.

MOTION MANAGEMENT IN STEREOTACTIC BODY RADIATION THERAPY

Authors

Benjamin J. Cooper

Medical Physics and Radiation Engineering, Canberra Hospital, Yamba Drive, Garran ACT 2605, Australia

Email: ben.cooper@act.gov.au

Yi Rong, PhD

Department of Radiation Oncology, University of California Davis Comprehensive Cancer Center, 4501 X Street, Suite 0152, Sacramento, California 95817, United States

Email: yrong@ucdavis.edu

Prof. Paul J. Keall

ACRF Image X Institute, Sydney Medical School, The University of Sydney,
Room 218, Biomedical Building C81, 1 Central Ave, Australian Technology Park, Eveleigh NSW 2015, Australia

Email: paul.keall@sydney.edu.au

MOTION MANAGEMENT IN STEREOTACTIC BODY RADIATION THERAPY

Abstract

Motion management in stereotactic body radiation therapy poses some complex challenges and yet takes on an essential role in the execution of a successful stereotactic radiation treatment. In this chapter we will discuss sources of motion and techniques that have been developed to address them. The management of motion due to respiration is discussed in some detail, including numerous technologies and techniques that have been developed. Concepts for motion management, from the treatment planning stage to the treatment execution stage, are discussed. Both historical and emerging technologies are discussed including considerations regarding, complexity, efficacy, and suitability to the clinical treatment site. Technical descriptions are given for the typical systems employed for monitoring and measuring motion in stereotactic body radiation therapy, including both x-ray radiation and non-x-ray radiation-based systems.

Key words

stereotactic body radiation therapy; SBRT; respiratory; motion management; tumor tracking; breath hold; motion monitoring;

1 SCOPE

In this chapter we build on the physics and immobilization outlined in previous chapters. Within the context of Stereotactic Body Radiation Therapy (SBRT) we describe (1) the sources of motion, (2) concepts for motion management, and (3) systems used for monitoring and measuring motion. The main focus is on gantry-mounted linear accelerator systems and accompanying subsystems. The emerging field of integrated MRI-linear accelerators will be discussed briefly. There is overlap between motion management for photons and protons. In

this chapter we focus on photon SBRT, and the proceeding chapter will explain proton SBRT in more detail. Broadly speaking, sources of organ motion arise from voluntary patient movement (moving a limb, for example) and involuntary movement (respiration, cardiovascular system, gastro-intestinal system and urinary system). The focus of this chapter will be on respiratory motion management, described as having the highest need for SBRT in AAPM TG 101 [1].

2 INTRODUCTION

Motion is an unavoidable part of radiation therapy. How much motion might be expected is very closely dependent on the clinical location of the treatment target. For example, cranial tumors (above the base of skull) exhibit very little movement with respect to the bony cranium (covered in a previous chapter); whereas lung tumors may exhibit relatively large motions with respect to surrounding bony anatomy (vertebrae, ribs, etc.). The success of Stereotactic Body Radiation Therapy critically depends on the ability to manage patient motion. Often the treatment targets are small and the planned dose distributions have steep gradients with potentially very high doses delivered in a small number of fractions (Figure 1a). If the geometric error between the target and the beam is more than that allowed for in planning, there will be a geographic miss with an under dose in the target and higher dose in normal tissues (Figure 1b). Therefore, a comprehensive motion management strategy is an integral part of any SBRT program.

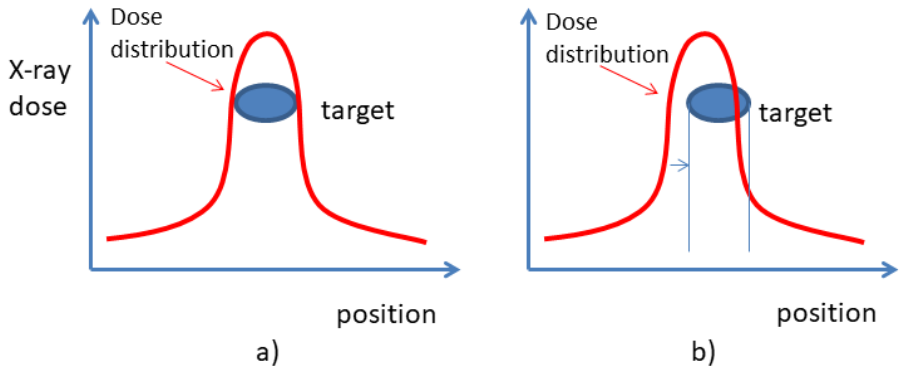

Figure 1. Steep dose distributions in SBRT must coincide with targets accurately (a); ideal target dose and (b) a small deviation between the dose distribution and the target can lead to a geographical miss.

2.1 Respiratory Motion Management

One of the simplest methods to deal with respiratory motion is to apply a treatment margin based on the range of internal motion due to respiration (e.g. lung cancer) with the goal of covering any tumor motion within the planned treatment volume (PTV). This is not an optimal solution for a number of reasons. Firstly, non-target, healthy tissue is getting the prescribed dose of radiation which is undesirable. Secondly, a consequence of using a large enough margin in the PTV to account for any tumor excursions during respiration puts an upper limit on the prescription dose because of concerns for normal tissue complications (toxicity). A patient receiving radiation therapy must first have a planning CT acquired. This must be performed with the patient set up in the same position as that in which the patient will be treated. Historically, a 3D-CT scan would be used giving rise to imaging artefacts (doubling, jagged edges, nonphysical features) due to motion from respiration [2, 3]. A four dimensional CT (4D-CT) allows respiratory motion to be elucidated; however, there are other challenges that arise from using 4D-CT including irregular breathing. There are various planning techniques that incorporate the respiratory motion information from 4D-CTs into

planning (some of the more common techniques are discussed in section 4.1). A fundamental problem with treatment planning is that the planning CT (either 3D or 4D) only gives information about the patient's anatomy on that day; in general the anatomy will be in a slightly (or grossly) different position on the day of treatment, usually several days or possibly even weeks after the planning CT scan acquisition. How can we be sure that the treatment plan will still be valid on the day of treatment? This is where respiratory motion management has a central role to play. A general workflow is presented (Figure 2):

1. Measure and plan for target motion during planning with 4D-CT scan
2. Monitor target motion at treatment
3. Compare target motion measured at planning (1) with target motion at treatment (2)
4. Is target motion acceptable?
5. Yes – continue treatment, loop back to (2)
6. a. No – Intervene, either by real time treatment adaptation and loop from (2), or
   b. stop treatment and reset patient (e.g. re-position, re-establish regular breathing) and loop from (2).

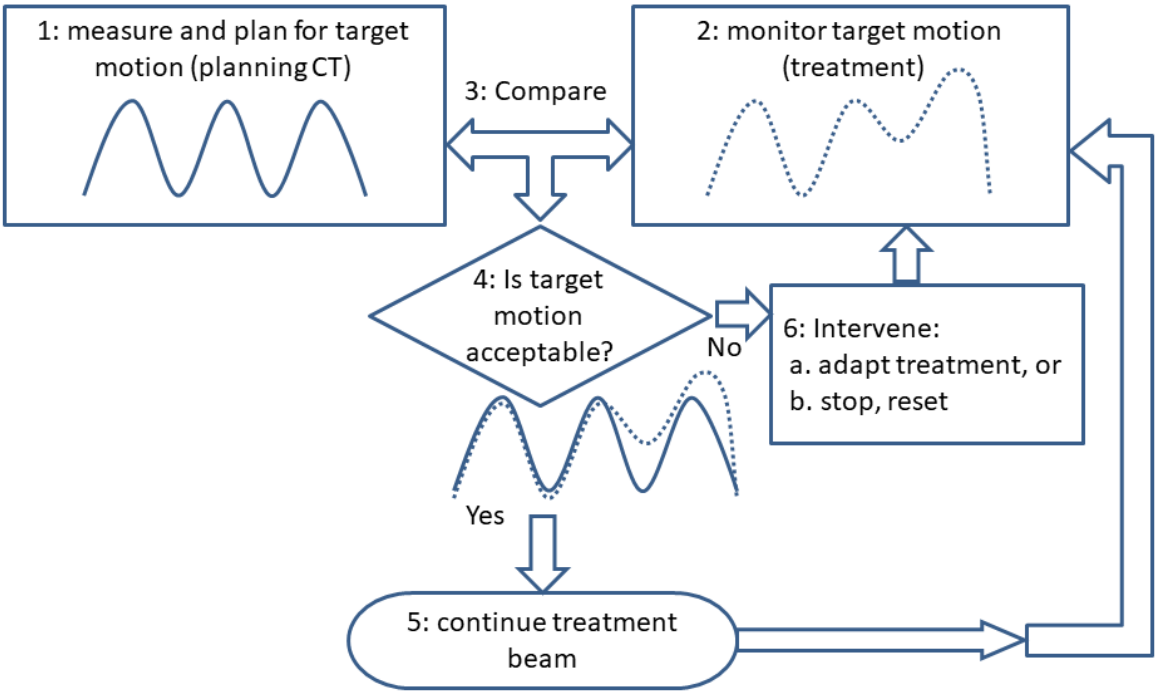

Figure 2. Generalized motion management workflow schematic.

3 Sources of Motion

3.1 Voluntary motion

Before considering internal tumor motion sources, it is important to consider the whole patient as a source of motion, in the sense that the patient as a whole body is moved into position prior to treatment. In general, image guidance, whereby radiological images taken during the treatment session, must be employed for SBRT. For large dose, hypofractionated treatments, it may be necessary to take intra-fraction guidance images during the treatment delivery. Details regarding immobilization can be found elsewhere within the book.

3.2 Involuntary Motion

3.2.1 Respiration

The most significant source of motion in thoracic and abdominal SBRT is respiration. Respiration is characterized as largely involuntary (i.e. automatic) but with some voluntary

control (e.g. holding one's breath). The involuntary neural control of respiration is a complex interplay between chemoreceptors responsive to the partial pressures of oxygen, carbon dioxide, acidity in the blood [4]. Keall *et al.* have tabulated lung tumor motion from 14 investigators in the report from AAPM TG 76 [5]. To give the reader a feel for the magnitude of motion reported in lung tumor motion, Table 1 reports the mean and maximum range in millimeters based on the motion data reported in table 1 of the TG 76 report [5].

Table 1. Mean and maximum ranges of lung tumor motion in millimeters in three dimensions: SI is superior-inferior; AP is anterior-posterior; LR is left-right.

Direction of lung tumor motion					
SI		AP		LR	
Mean	Max.	Mean	Max.	Mean	Max.
8.4	50	3.5	22	4.6	16

The range of target motion due to respiration is very variable and patient specific. As such, each individual patient should be assessed for developing the best motion management strategy in SBRT.

Generally speaking, respiration may be characterized by several parameters: (1) "tidal volume" – how deep or shallow is the respiration; (2) "regularity" – how much does period and amplitude vary over the course of a treatment beam; (3) respiratory period (time from end exhale, to inhale, to end exhale again, for e.g.). A mathematical model that parameterizes respiratory motion $\boldsymbol{z}$ as a function of time $\boldsymbol{t}$ has been described [6]

$$\boldsymbol{z(t) = z_0 - b\cos^{2n}\left(\frac{\pi t}{\tau} - \phi\right)} \qquad \text{eq 1}$$

where $\boldsymbol{z_0}$ is position at exhale, $\boldsymbol{b}$ is the amplitude of motion (thus $\boldsymbol{z_0 - b}$ is position at inhale), $\boldsymbol{\tau}$ is respiration period, $\boldsymbol{n}$ is a 'fitting parameter' and $\boldsymbol{\phi}$ is initial phase in radians.

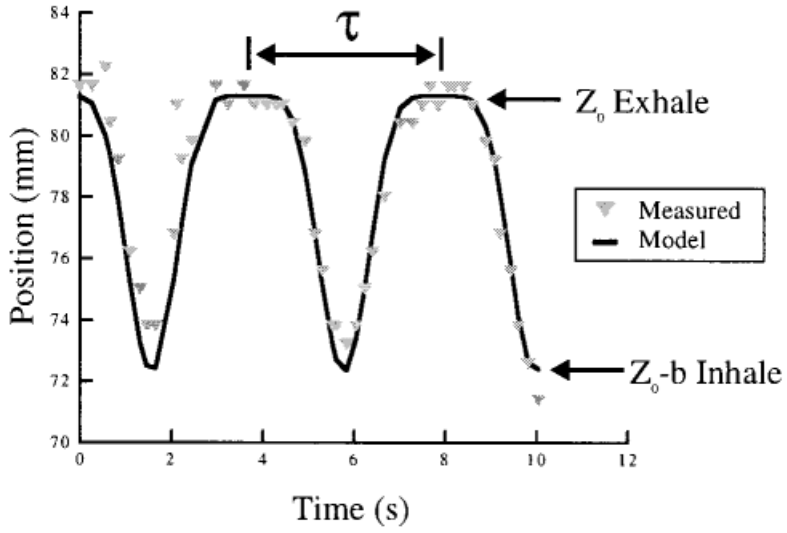

Figure 3. Example of the mathematical motion model (solid line) fitted to diaphragm position measurements (inverted triangles) [6]

This model is a useful starting point for respiratory motion modeling, however it makes certain assumptions of constant respiratory periodicity and consistent amplitude which is not true in the general case for respiration because of its voluntary / involuntary nature as previously mentioned.

George *et al.* applied this model to the study of 331 respiratory traces from 24 patients. Extending this model, it was reported that rather than fixed values for $\boldsymbol{z_0}$, $\boldsymbol{b}$, and $\boldsymbol{\tau}$, respiration may be modelled more realistically with a statistical distribution of those values [7].

Seppenwoolde *et al.* successfully modelled 20 patients' 3D tumor trajectories through a method of finding the best-fit parameters for all three cardinal directions (SI, AP, LR) using real-time 3D fluoroscopic positional data of implanted gold seeds [8]. Nearly half of the patients exhibited tumor trajectories with a 1-5 mm hysteresis (i.e. the tumor path during inhale and exhale were different). For a third of patients, cardiac motion affected trajectories

by 1-4 mm. Both these effects highlight the complexity of respiratory induced tumor motion and underscore the notion that is a useful but limited parametric model for tumor motion and cannot be expected to model all respiratory patterns. Figure 4 summarizes the 21 tumor trajectories from the study, illustrating the variety of complex tumor motion [8].

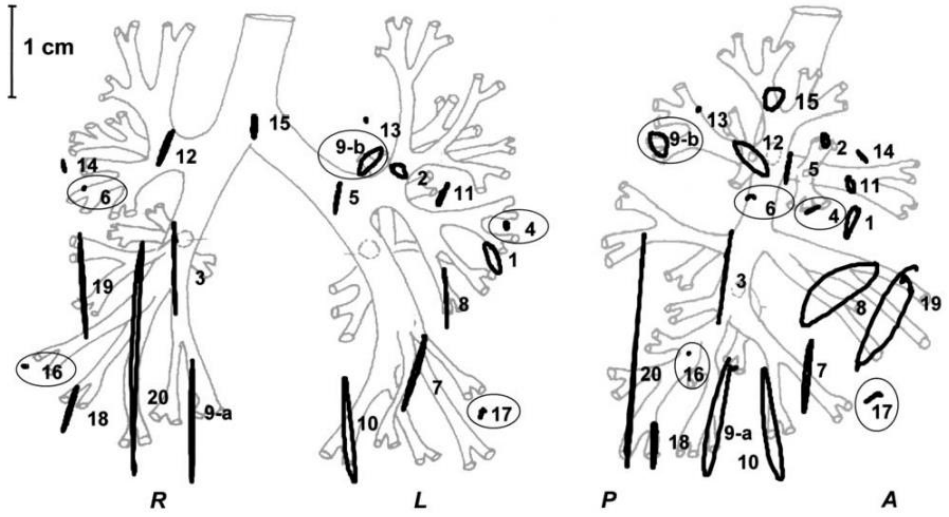

Figure 4. Coronal (left) and sagittal (right) projections of 21 tumor trajectories (dark lines, numbered). Circled numbers represent tumor attachment to bony structures [8].

In an effort to address these deficiencies, Ruan *et al.* proposed an algorithm for real-time profiling of respiratory motion where features such as baseline drift, phase variation and fundamental pattern change can be decomposed from the signal, helping to characterize the real-time changes in respiration, potentially during treatment, which in turn can facilitate clinical decisions / response actions to mitigate treatment degradation [9].

A further complication is the consistency of patient breathing. Shah *et al.* investigated the use of electromagnetic transponder implants from the commercially available Calypso™ system. The motion trace from 'Patient 2' (Figure 5) indicates the potential for both large intra- and inter-fraction variations in lung tumor motion including variation in amplitude and periodicity [10].

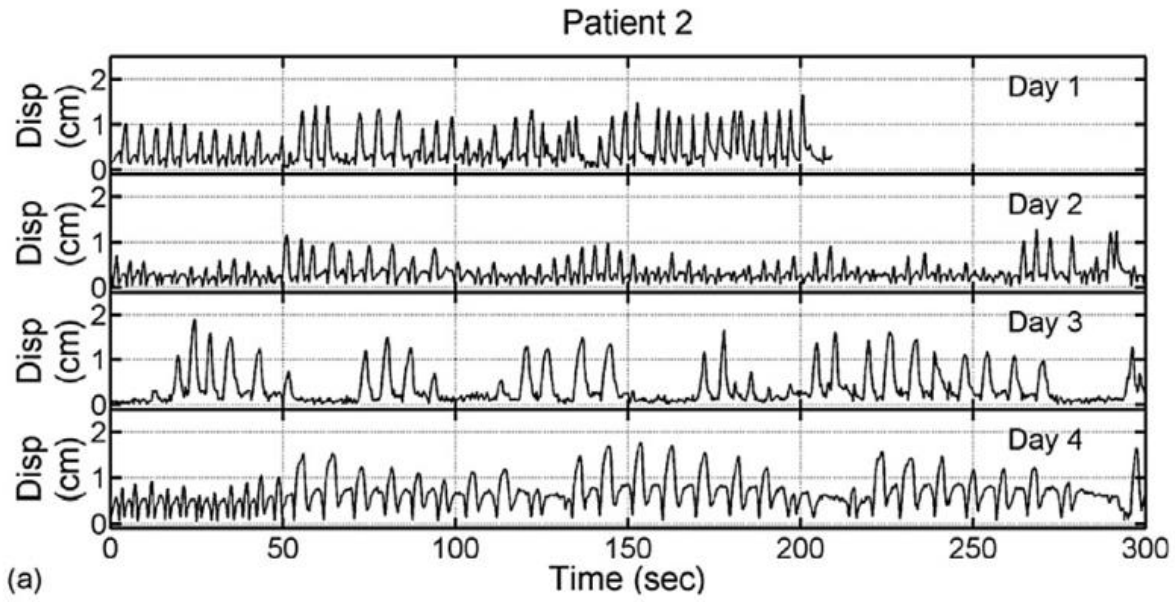

Figure 5. Lung tumor displacement recorded over 4 consecutive days illustrating intra- and inter-fractional variations. [10]

3.2.2 Bladder and gastro-intestinal filling

Both the bladder and rectum are sources of inter- and intra-fractional motion of particular importance for stereotactic radiation therapy of the prostate. Careful adherence to bladder and bowel preparation protocols is typically required of patients. Bladder preparation protocols may include directions to drink certain volumes of liquid at defined times prior to treatment. Depending on the clinical circumstance, the protocol may involve voiding bladder and or bowel before treatment. The aim is to have the bladder, rectum and prostate in a position as close to the planning scan as possible.

4 Concepts for Motion Management

In the context of SBRT, there exists the highest need for respiratory motion management and the maintenance of high spatial targeting accuracy throughout the entire treatment[1]. The clinician must decide on which motion management strategy is the most appropriate to

achieve the clinical goals, taking into consideration all of the patient's capabilities and tolerances for undergoing motion management. In this section we discuss some of the strategies that are available. Figure 6 illustrates that motion management strategies generally become increasingly complex as the treatment margin requirements become "tighter".

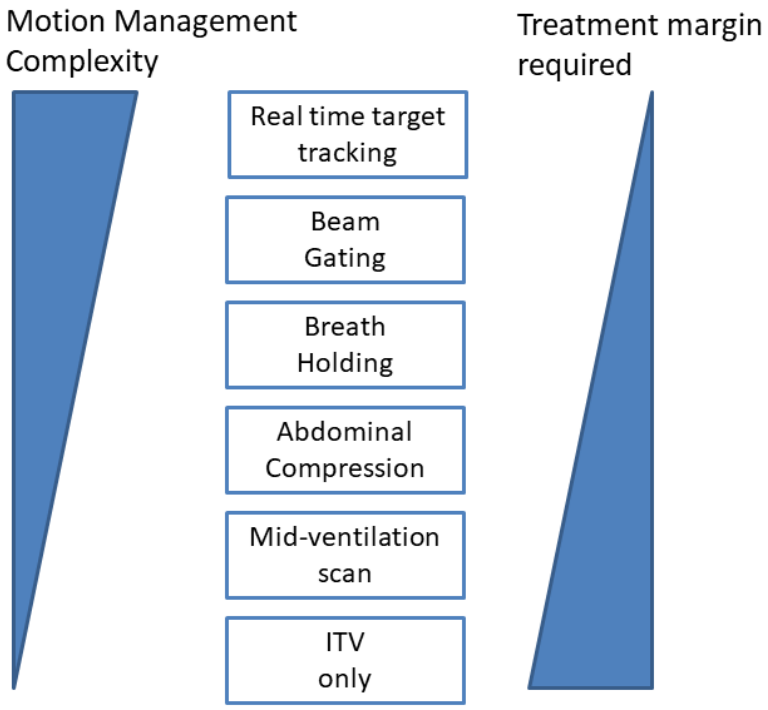

Figure 6. A more precise and accurate treatment requires smaller treatment margins but at the cost of greater motion management complexity.

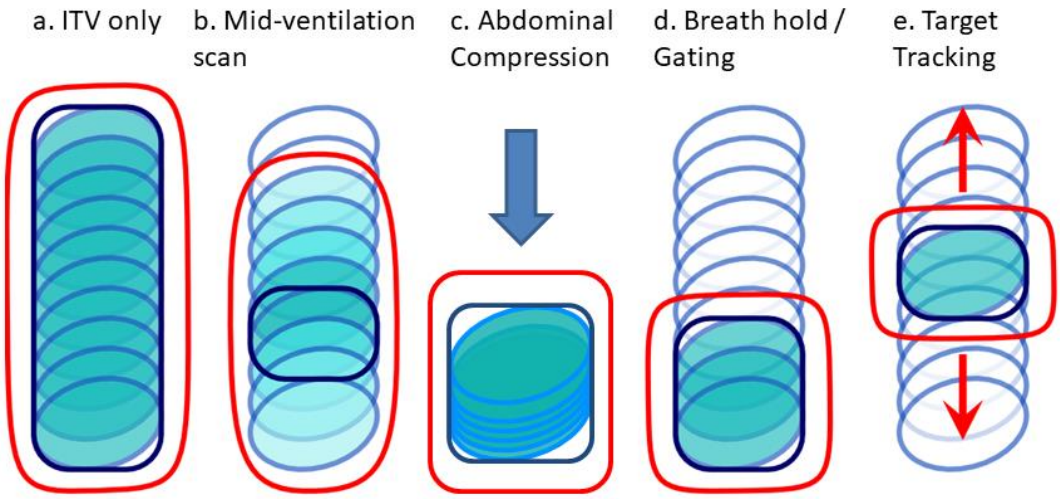

Figure 7. Schematic illustrating five techniques for motion management. The ellipse shape depicts tumor target motion over breathing phases; the smaller rectangles depict the ITV, the larger rectangles depict the beam aperture. a. ITV only; b. Mid-ventilation scan; c. Abdominal Compression; d. Breath hold / Gating; e. Target Tracking (figure based on ref [11]).

4.1 PLANNING FOR TUMOR MOTION

There is a need to accurately identify the anatomy and trajectory of targets and surrounding tissue to enable the evaluation of the cumulative dose over the respiratory cycle in lung SBRT[12]. Four Dimensional Computed Tomography (4D-CT) is a central imaging tool to fulfil these requirements and its use in treatment planning is described below.

4.1.1 INTERNAL MOTION MARGIN

Perhaps the simplest approach to manage respiratory induced tumor motion is simply to use the patient's respiratory motion information for creating an Internal Motion Margin (IM) in the context of creating an Internal Target Volume (ITV)[13]. In this scenario, the IM can be derived from a 4D-CT scan. This allows the clinician to visualize the extrema of tumor

motion from which the IM is defined. However, it has been reported that this simple approach can lead to an over-estimation of Planning Target Volumes [14]. A common approach is to use a Maximum Intensity Projection across all phases of a 4D-CT scan in lung to generate the ITV (Figure 7a) permitting rapid assessment of mobility of targets in lung cancer radiotherapy [15, 16]. Unfortunately tumor motion, particularly tumors located in the vicinity of the diaphragm, can be tens of millimeters in magnitude leading to potentially large IMs and PTVs, unnecessarily irradiating healthy lung tissue. In general, margins do not account for respiratory variations (for example if the patient takes a deeper breath). On the other hand, if the clinician judges the tumor motion to be acceptably small in magnitude, these methods for determining ITVs might suffice.

A mid-ventilation CT scan technique proposes to use a single, "well chosen" CT scan from a 4D-CT set (Figure 7b). The chosen scan acts as a representative reference average position of a mobile tumor target over the breathing cycle in lung, allowing for the possibility of margin reduction in planning [17, 18]. Mid-ventilation reference images can facilitate treatment of free breathing patients (without compression or breath hold) and a potentially reduced treatment margin, however, there is an increased risk of breathing artifacts for mid-ventilation imaging because the tumor velocity is high at this phase of the breathing cycle [18].

4.2 TUMOR MOTION DETECTION: TREATMENT COMPARED TO PLANNING

The work performed on characterizing and accounting for the motion of a tumor during the planning stage of SBRT must be followed up with careful assessment of the tumor motion detected immediately prior to, and during treatment. It is critical to the success of the treatment that the tumor motion is assessed to be within the planning margins. Fortunately, gantry mounted kV imaging systems (usually orthogonal to the treatment beam axis) are universally available on current release linear accelerators, making a revolutionary contribution to image guidance workflow for patient positioning accuracy and motion

management in SBRT. Reference radiological images from planning (3D / 4D-CT and or Digitally Reconstructed Radiographs [DRRs]) may be registered with radiological images (orthogonal planar kV pairs, 3D- and 4D-CBCT) from the gantry mounted kV imaging system. Matching the "images of the day" at the time of treatment with the reference images is designed to yield a re-positioning vector: either a 3D translation (most commonly) or a 6D vector which incorporates 3 translational movements as well as 3 rotational (pitch, roll, yaw) movements (Figure 8).

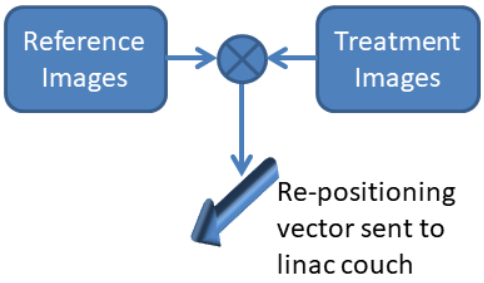

Figure 8. Reference images from planning are compared to treatment images from imaging systems "on-board" the linac treatment machine. The difference between the images is used to calculate a re-positioning vector with the goal of minimizing mismatch.

Commercial systems such as BrianLab's ExacTrac™, Varian's PerfectPitch™ 6 degrees of freedom, Elekta's HexaPOD™ evo RT all follow a similar generalized workflow summarized as: (1) acquire "fresh" patient images immediately prior to treatment; (2) process those images to calculate a possible patient re-positioning vector; (3) execute the patient re-positioning action by automatically sending motion instructions to the linac couch, either a 3D translational movement or possibly a couch capable of 6D movement, including pitch, roll and yaw. Figure 9 schematically illustrates how a pre-treatment 4D-CBCT can resolve a lung tumor trajectory into respiratory phases (numbered) and in this example there is hysteresis in the target trajectory. The initial setup shows that the PTV would miss the target

but after the repositioning vector is applied, following Figure 8, the PTV covers the entire respiratory cycle with no miss. This example encompasses the entire tumor trajectory (Figure 7a) but 4D-CBCT could also be used in conjunction with gated beam delivery reducing the required PTV.

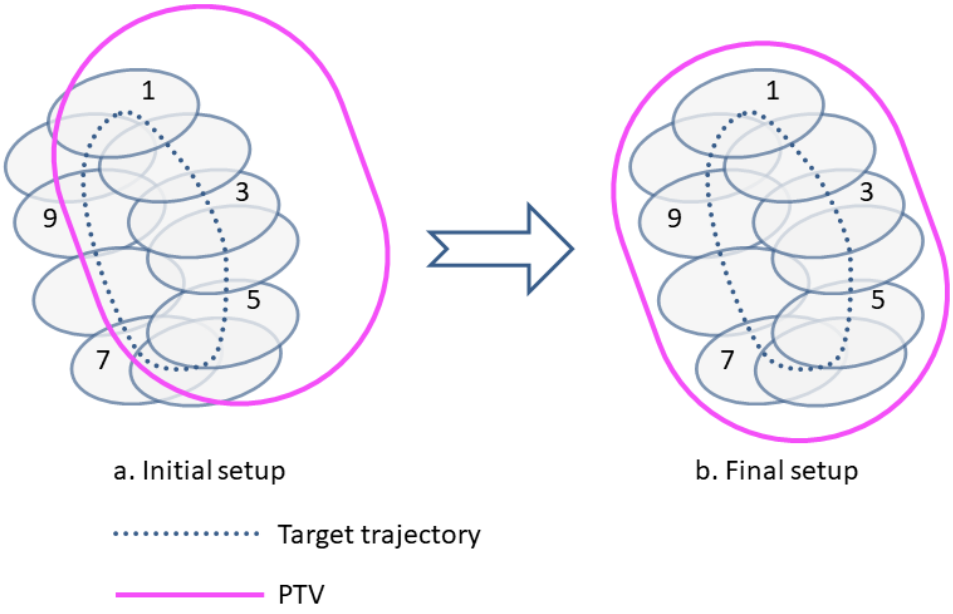

Figure 9. a. A pre-treatment 4D-CBCT scan resolves a tumor target trajectory (small ellipses, odd phases numbered for clarity). The initial setup shows the planned PTV would miss; b. after re-positioning (see Figure 8) a second 4D-CBCT scan confirms a good match between the planned PTV covering the tumor target trajectory.

4.3 Restricting Tumor Motion

4.3.1 Breath holding approaches

The clinician, treatment and planning teams need to decide if motion compensation is going to be used at treatment delivery or not[1] because this will have an impact on the magnitude of the ITV used in planning: if any kind of breath hold technique is used, then this potentially opens the possibility for a smaller internal margin and less normal tissue irradiation. This is difficult because it requires a high degree of confidence in getting the tumor into position via

patient breath hold at the planned respiratory phase. Typically, breath hold techniques require respiratory motion signals to be monitored and used in conjunction with image guidance systems, possibly using radio-opaque marker implants, to verify an acceptable correlation between phase of breath hold and actual tumor position.

4.3.1.1 Deep inspiration Breath Hold

Hanley *et al.* investigated the potential value of Deep Inspiration Breath Hold (DIBH) in lung radiation therapy. The idea of DIBH is that patients modify their normal breathing pattern by forcibly expelling air in a slow vital capacity maneuver, then taking a deep breath and holding at inspiration during treatment delivery (Figure 7d, Figure 10).

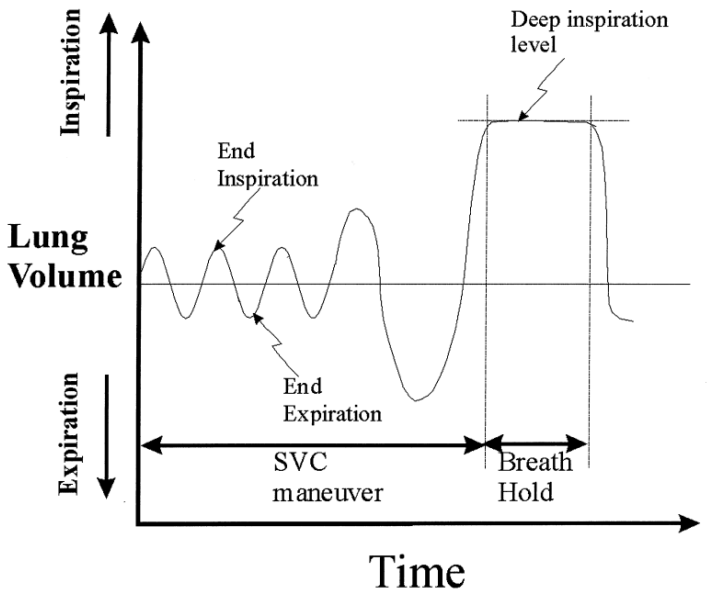

Figure 10. Lung volume changing over time showing the slow vital capacity maneuver (SVC) and breath hold. [19]

The benefits are: (1) lung volume is increased which lowers lung density overall, helping to reduce normal lung tissue irradiation, and (2) tumor target motion due to respiration is effectively arrested [19]. In a planning study, the authors report that the DIBH technique can reduce the relative volume of lung receiving 25 Gy by 30% [19]. Another DIBH

study by Mah *et al.* demonstrated the use of spirometry to infer the displacement of the tumor centroid at treatment time as compared to tumor position at planning. Using a DIBH maneuver and spirometry, the authors reported a mean displacement and standard deviation of 0.02 ± 0.14 cm between the treatment time tumor position and the planned position, and this was consistent with independent tumor position measurements with port films [20] (radiographic films exposed with the treatment beam exiting the patient). Unfortunately only around 50% of lung cancer patients were able to perform the DIBH breathing maneuver [20].

4.3.1.2 Active Breathing Control (ABC)

Active breathing control, or "ABC", is a treatment technique whose goal it is to minimize tumor target motion due to respiration. This is achieved by controlling the flow of air into the patient's lungs via a computer controlled valve inside a breathing tube system. Air flow is continuously monitored by the ABC computer giving a respiratory signal. At a pre-determined phase of the respiratory cycle (usually full inspiration), the ABC system stops the airflow and forces a controlled patient breath hold during which the treatment beam is delivered (Figure 11).

Figure 11. Active Breathing Coordinator system™. Image courtesy of Elekta.

It is often the case that a treatment beam's duration is longer than the time a patient is able to hold their breath comfortably necessitating two or more consecutive breath holds to complete the treatment beam. A study of the reproducibility of repeat ABC breath holds of 8 patients receiving treatment for intrahepatic tumors reported a mean diaphragmatic reproducibility of 2.5 mm (cranio-caudal direction). The same study reported an average absolute inter-fraction offset of 5.2 mm in the CC direction. The relatively large inter-fraction offsets can be addressed by daily imaging and is required if any substantial reduction in PTV margin is desired [21].

4.3.2 Abdominal compression to force shallow breathing

Normal breathing occurs when the action of the diaphragm "pulls" down into the abdominal cavity causing air to fill the lungs. Abdominal compression is a simple technique to reduce lung and liver tumor motion by restricting the normal action of the diaphragm and enforcing shallow breathing (Figure 7c). Lax *et al.* have described tumor motion in liver ranging from 1.5 - 2.5 cm during quiet breathing. Applying a light, constant pressure to the abdomen by

tightening a belt around the patient, diaphragm motion could be reduced to 0.5 - 1.0 cm [22], thereby reducing the likelihood of the target moving out of the high dose region. Utilizing 4D-CT for analysis, tumor and organ motion can be significantly reduced under medium and high abdominal compression. In a small 10 patient study, mean tumor motion was reduced from 13.6 mm (no compression), to 8.3 mm (medium compression at an average pressure of 48 N), and to 7.2 mm (high compression pressure, 91 N) [23]. Abdominal compression must be assessed on a patient by patient basis for suitability in SBRT given that the authors reported that 3 out of 10 patients still exhibited tumor trajectories exceeding 1 cm, deemed to be unacceptable for SBRT [23].

4.4 GATING THE BEAM DURING TREATMENT

Beam gating is where the treatment beam is switched on only when the target is in a pre-determined position during the respiratory cycle. The aim is to reduce normal tissue irradiation by trimming the radiation beam down to a smaller beam aperture where instantaneous target motion is at or near a minimum (Figure 7d, Figure 12).

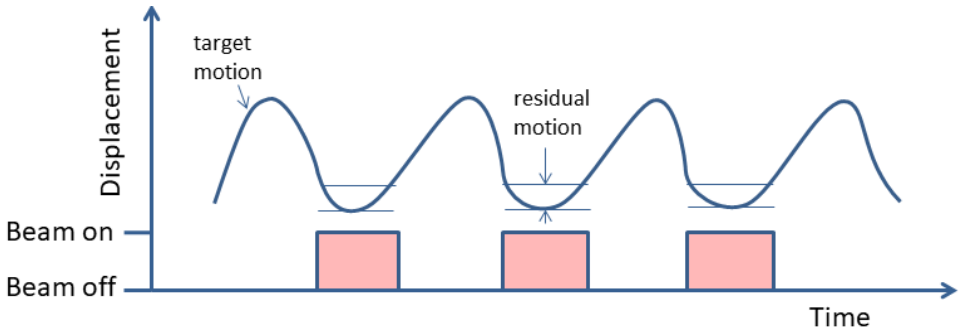

Figure 12. Gating the treatment beam is switching the beam on at a pre-determined part of the breathing cycle. The on duty cycle of the beam (shaded rectangles) is only allowed to occur within the residual motion window that is pre-set.

There is a balance between having a small beam on duty cycle, which gives less residual motion but higher treatment times, and a larger beam on time which is faster but has higher residual motion. The gating concept is straightforward; however, the practical execution is technically difficult for numerous reasons: (1) internal / external correlation (phase shift); (2) longer treatment time (beam can be off for 50% - 70% of duty cycle); (3) irregular breathing (4) residual motion during the "beam on" phase. For these reasons, some authors have reported that the difficulty with gating may not outweigh the benefits for patients with tumor motions less than 2cm [24-26].

4.5 Tumor Tracking and Real Time Beam Adaptation

Tumor tracking is an advanced technique whereby measured tumor motion signals during treatment can be used in a feedback loop to change the beam aperture dynamically and "adapt" the treatment to compensate for the tumor motion. The ability to detect motion and use this information to update the beam collimation and "track" the target in real time allows greater conformality to treatment targets and can reduce the need for manually repositioning the patient during treatment. The CyberKnife™ system, a specialized robotic radiation therapy device, was one of the first systems capable of tracking respiratory motion[27, 28]. The Vero™ system (no longer commercially available) took a different approach whereby the radiation beamline, assembled on orthogonal gimbals, could track moving tumors [29]. A feasibility study of MLC linac based *in vivo* tumor tracking was first demonstrated in pigs [30]. The first human clinical implementation of linac based dynamic MLC beam shaping to track tumor motion relied on the motion signals coming from electromagnetic transponder implants. These motion signals are processed by a computer program whose output instructs

the MLC leaves to optimally align the treatment beam to the target, all during "beam on" (Figure 13).

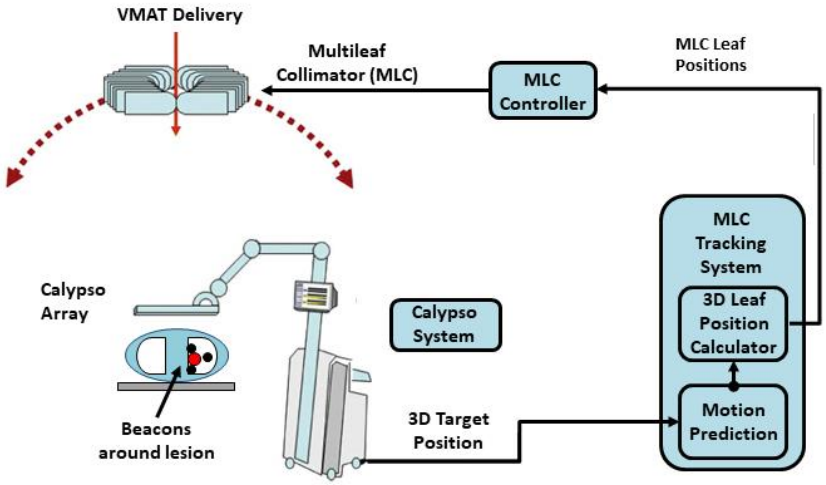

Figure 13. Real time tumor tracking feedback loop. Tumor motions are detected by the 3D target position system (Calypso) and processed by the MLC tracking software to automatically adjust the MLC leaf positions in real-time. [31]

The motion detection-to-adaptation feedback loop has been clinically demonstrated. The first human treatment using this technique was for a prostate cancer patient being treated with a dual-arc VMAT technique [32]. Keall *et al.* reported that without tracking, there was a 30% increase in the fractional rectal volume receiving 60 Gy compared to the original plan [32]. More recently, the same electromagnetic-guided real time adaptive radiotherapy technique was applied to a lung cancer patient receiving 48 Gy over 4 fractions using Stereotactic Ablative Body Radiotherapy (SABR) [31]. In lung cancer radiotherapy, the target motion is generally more complex due to respiratory motion, especially for tumor sites located close to the diaphragm. At the planning stage, 4DCT was used to attain respiratory motion information. The end-of-exhale phase was used to define a 'tracking' GTV ($GTV_{Tracking}$) then expanded by 5mm to define a PTV. A fundamental difference in adaptive radiotherapy

planning is that the actual tumor trajectory on the day of treatment cannot be known exactly *a priori*. A novel planning technique was developed to deal with this issue whereby an "isocenter shift method" considers each planned treatment arc as many sub arcs each with isocenter shifted in 2 mm bins to mimic target volume motion. Treatment log files, recording actual MLC leaf positions during treatment, and the EM transponder trajectories (assumed surrogates for target motion) inform the isocenter shift method to reconstruct the dose delivered utilizing the treatment planning system [31]. Booth *et al.* report that in comparison to standard ITV-based planning, the real time adaptive radiotherapy with MLC tracking reduced the PTV from 18.7 to 11 cm^3; mean lung dose reduced from 202 to 140 cGy with lung V20 and V5 reduced by 35% and 9% respectively [31]. Another broadly available technology yet to be clinically implemented for real-time adaptation is the treatment couch, for which there has been considerable research and development, e.g. refs [33, 34] and subsequent articles. The community awaits the clinical translation of this technology which could be used as the sole adaptation method or in conjunction with MLC tracking and other degrees of freedom that could be modified on a modern linear accelerator, such as the gantry and collimator angles to improve beam-tumor targeting.

5 SYSTEMS FOR MONITORING AND MEASURING MOTION

The motion monitoring and measuring can be realized using the in-room image guidance solutions, which can be categorized as (1) radiation based systems and (2) non-radiation based systems. This section elaborates on the technical details of some of the available monitoring and measuring systems.

5.1 RADIATION-BASED SYSTEMS

For those radiation-based systems, motion monitoring relies on continuous imaging of the moving objects. The images are formed on imagers while detecting the attenuated x-ray photons. Important parameters that are relevant to motion monitoring are image resolution, acquisition rate, imaging dose, and accuracy. The fundamentals of image source, detectors, and imaging parameters are elaborated below.

5.1.1 X-RAY SOURCES

Radiation-based systems for in-room image guidance use x-ray sources with energy ranging from kilo-voltage to mega-voltage. Systems with MV x-ray sources either directly uses the 6 MV treatment beam (C-arm linac or Accuray CyberKnife) or a ramp-down 3.6 MV beam (Accuray Tomotherapy). Systems with kV x-ray source require an independent kV x-ray generator that can be mounted directly on the linac gantry or within a ceiling/floor space. Typical kV x-ray energy is similar to conventional CT scanners, with a range of 100 to 140 kV.

5.1.2 IMAGING DETECTORS

The most common imaging detector for both kV and MV x-ray sources is the solid state flat panel imager (FPI). The FPI acquire images from a layer of phosphor screen made of Gadolinium oxysulphide base doped with terbium (Gd_2O_2S:Tb)[35]. The imagers are mounted on a mechanical arm, with 180 degree from the imaging source. The detailed specifications of the MV and kV imaging system are listed in Table 2. Another imaging detector is Xenon gas detector. Adopted from the old generation of CT scanners, Accuray Tomotherapy uses xenon-filled 640 channel CT detectors housed in an aluminium box [36]. These detector channels are separated by tungsten septa that are not in the line of divergence of beam axis. Signals are proportional to the scattering photons from Compton interactions of MV x-ray

beams and the tungsten septa. This out-of-focus design allows higher scatter along the beam edge as compared to the beam center, resulting a signal dip at the center of the detector-measured profiles [37].

Table 2. Flat Panel Detectors for kV and MV imaging

Flat Panel Detector Type	MV			kV	
Linac	Varian-TrueBeam	Varian-TrueBeam/EDGE	Elekta-VersaHD	Varian-TrueBeam	Elekta-VersaHD
Detector model	aS1000	aS1200	XRD 1642	4030CB	XRD 1642
Scintillator	GOS	GOS	Various GOS	CsI	CsI
(Active) Imaging Area (cm^2)	40 x 30	43.0 x 43.0 (40.0 x 40.0)	41 x 41	39.7 x 29.8	41 x 41
Pixel matrix (1x1) (2x2)	1024x768 512x384	1280x1280 (1190x1190) 640x640	1024x1024	2048x1536 1024x768	1024x1024
Pixel pitch (mm)	0.392 or 0.784	0.336 or 0.672	0.4	0.194 or 0.388	0.4
Lag 1st frame	4%	1.5% @7.5fps	<5%@10fps	<5%@7.5fps	<8%
Energy range	40kV – 15MV	40kV – 15MV	20 kV – 15 MV	40 - 150 kV	40 - 150 kV
Max image acquisition rate	Up to 23fps	20fps	Up to 100 fps	Up to 30fps	Up to 100 fps
Contrast resolution	0.2% for 6MV, 0.8MU/frame, 10 frames	0.15% for 6MV, 1.5MU/frame, 2frames			2.58 lp/mm @ 7.5 fps (1x1) 1.29 lp/mm @ 30 fps (2x2)
MTF		0.35 cycles/mm for 6MV		>45% @1lp/mm for 80kVp	63% (0.5 cy/mm), 31% (1 cy/mm) for RQA5 with CsI

5.1.3 *Clinical systems and their use in motion monitoring and management*

With the combination of different x-ray sources and detectors, the available imaging modes include 2D, 3D, and 4D for both kV and MV systems, as listed in Figure 14.

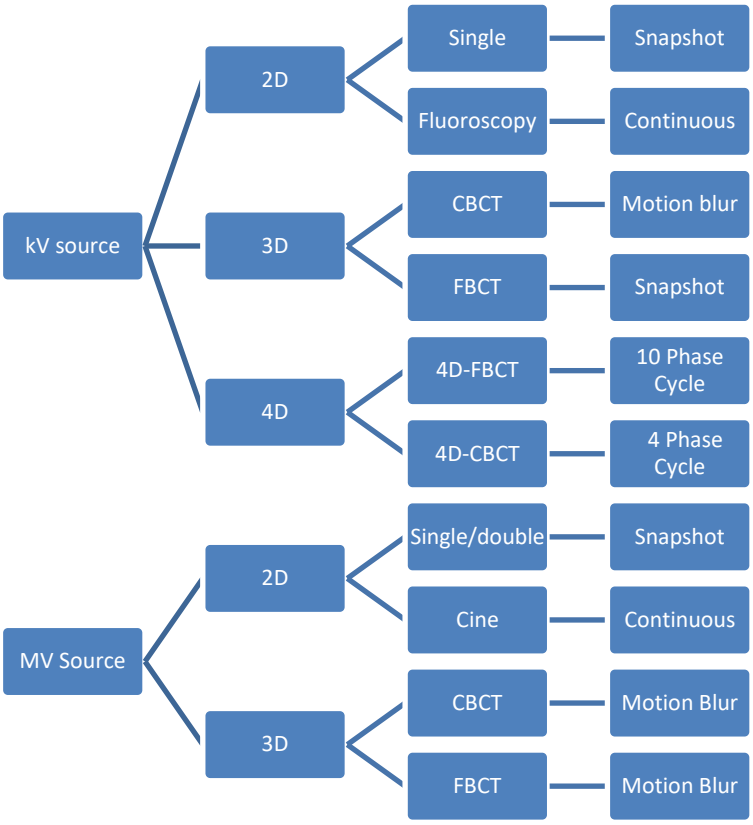

Figure 14. Clinically available imaging modes and their applications in motion management

5.1.3.1 A. kV imaging

With the combination of kV x-ray source and solid state detectors, images can be generated in various dimensions, including 2D, 3D, and 4D. All of them can serve the purpose of patient positioning and motion management. In the initial phase of patient simulation, a 4D CT sorted through 10 respiratory phases is usually acquired on the planning CT unit when

treating area is involved with significant motion. In the treatment room, various imaging modes can be utilized to manage or track motion. As shown in Figure 15, the two commonly used systems used in conjunction with a linear accelerator include gantry-mounted imaging system[38] (Figure 15 A and B) and floor-ceiling mounted imaging system[39] (Figure 15 C and D).

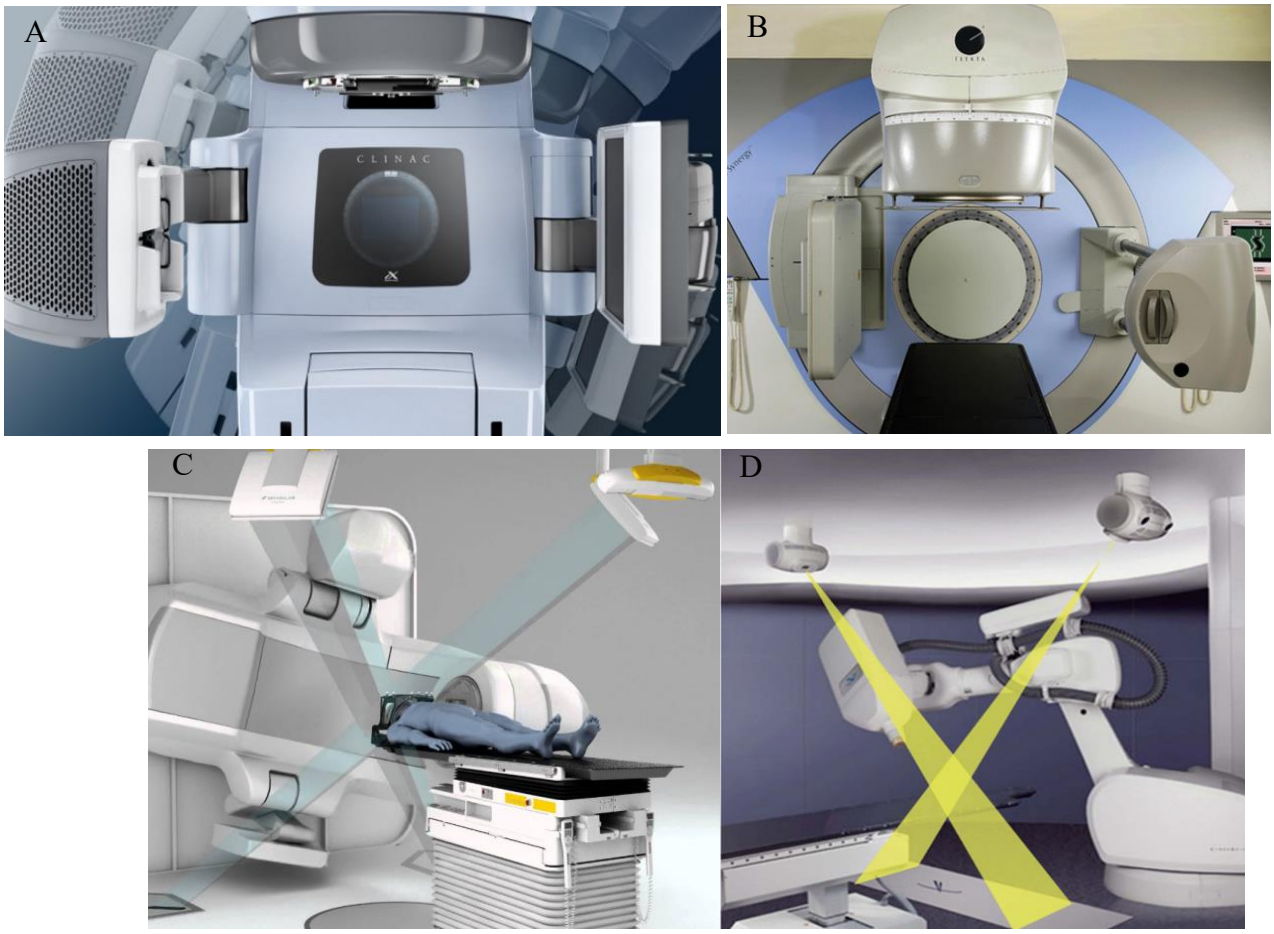

Figure 15. Typical gantry-mounted imaging systems (A Varian Trilogy and B Elekta Synergy) and floor-ceiling mounted imaging systems (C BrainLab ExacTrac and D CyberKnife)

For gantry-mounted systems (C-arm linacs from Varian or Elekta), kV x-ray tube and the FPI are mounted directly on the linac gantry, orthogonal to the beam axis. In this setting,

the available image modes include 2D single/fluoroscopy, 3D CBCT, and 4D CBCT imaging. Motion monitoring and assessment can be achieved using 2D fluoroscopy and 4D CBCT modes. Continuous kV images can be acquired by the imager at an acquisition rate of 15 fps prior or during treatment. If used prior to treatment, the kV x-ray tube can be placed at the same gantry angle as the treatment beam, in order to assess the target motion in a beam's eye view. If used during treatment, kV x-ray tube can be turned on at the same time as the treatment beam-on, but rotated 90 degrees from the treatment angle. This mode is mostly used for motion monitoring. In both cases, visualization of the moving target is challenging with the 2D imaging mode. There are two ways to mediate the issue: one is to use a surrogate that can be visualized on the 2D image, i.e. the diaphragm for lung cancer[40, 41]; the other is to plant fiducial markers that can be seen on kV images in or around the target[42, 43]. Typical imaging dose ranges from 1-3 mGy per kV radiograph image, thus can ramp up to 0.1-0.3 cGy per fluoroscopy [44]. The time synchronized 4D CBCT image is created through sorting and binning a group (4 phases and 10 phases) of 3D CBCT image slices based on their corresponding breathing cycles, available on the new models of Elekta[45, 46] and Varian linacs[47]. In comparison with the 4D CT acquired at the time of simulation/planning, 4D CBCT provides the most accurate way in managing and verifying the respiration-induced target motion prior to treatment delivery. The limitations include prolonged imaging time and elevated imaging dose to patients[47, 48].

Ceiling/floor mounted systems include BrainLab ExacTrac and CyberKnife. BrainLab ExactTrac is a stereotactic hybrid system, equipped with kV stereoscopic imaging, infra-red tracking, and 6-D couch[39]. The stereoscopic imaging system is composed of two kV x-ray tubes mounted on the floor and two a-Si FPDs mounted on the ceiling. The infra-red tracking system is composed of two infra-red cameras, one video camera, and an infra-red marker array. The motion tracking capability relies on the infra-red system and/or x-ray with bony

anatomy. This system is mostly designed for intra-cranial treatments, therefore, not ideal for extra-cranial sites where large motion may occur. CyberKnife also has a stereoscopic imaging system, but with the x-ray tube mounted on the ceiling and the a-Si FPDs mounted on the floor. Unlike BrainLab, the x-ray images can be acquired continuously at an interval of 5-90 s depending on the imaging mode[49]. This provides the capability of real-time tracking with the options of using bony structure, fiducial marker, or soft tissue[49]. The drawback is that each image adds an additional 0.01-0.07 cGy imaging dose to patients.

5.1.3.2 B. MV imaging

The imaging systems with the MV x-ray sources are all gantry mounted, with the options of generating 2D portal images or 3D reconstructed MV CT images. The MV imager is mounted on the linac gantry, 180 degrees from the treatment head, as shown in Figure 16 A and B.

The 2D single/double exposure mode is mostly used for patient setup or field shape verification prior to treatment. Typical dose per image ranges from 2 to 3 cGy, depending on the imaging mode chosen and the MU used for imaging (1-5 MU for most users) [44]. The MV Cine mode collects exit radiation using the MV panel during treatment at a certain frame rate (Table 2). The benefit of this continuous imaging mode is that there is no additional dose to patients[50]. The limitation is low soft tissue contrast due to the inherent tissue interaction property with MV beams. The most use of this capability in motion monitoring is on the tangent beams when treating breast cancer, as shown in Figure 16 C [51]. It distinctively shows the boundary of chest wall as opposed to the edge of the MLC collimation, which can be compared with DRRs from the treatment plan in order to monitor the positioning of patient's breast or chest wall during treatment. This is especially useful for deep inspiration breath hold (DIBH) treatment for left breast cancer [51].

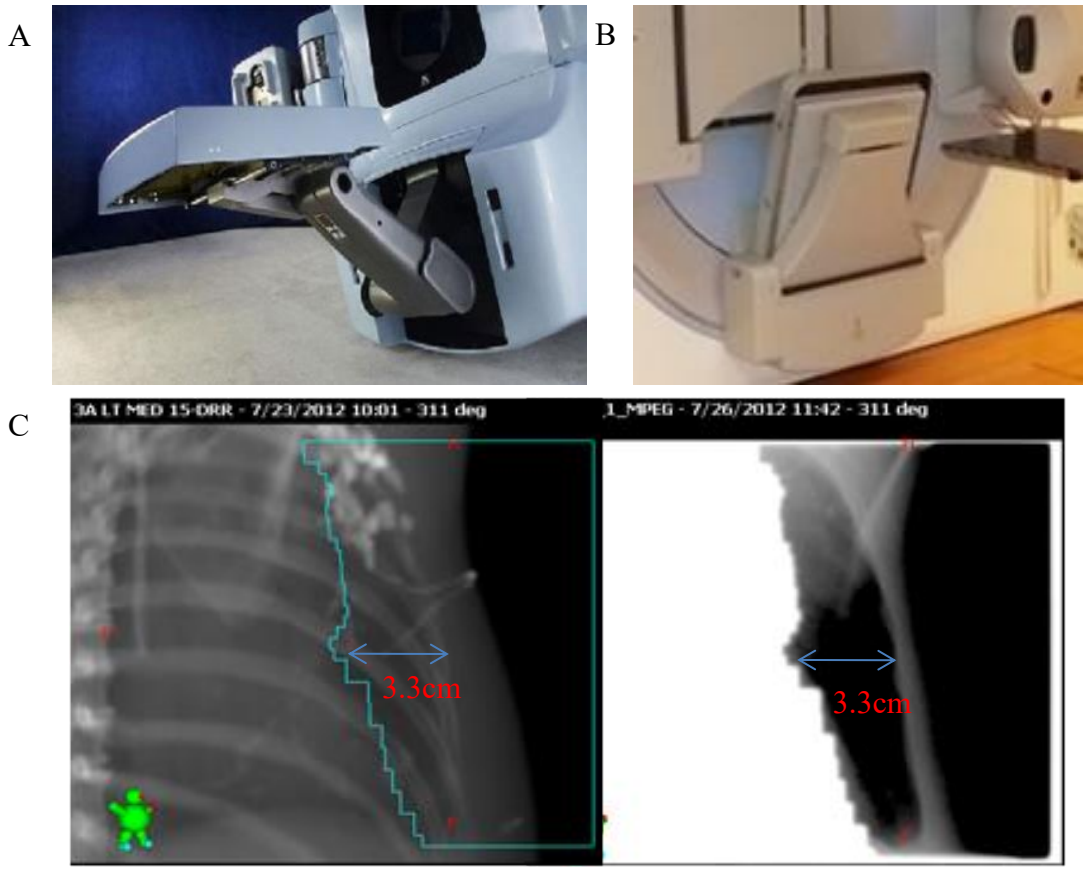

Figure 16. A. Varian robotic 3-axis arm; B. Elekta retractable EPID arm; C. EPID MV Cine imaging during treatment for motion tracking.

The 3D MV CBCT acquisition mode is available on Siemens linacs[52] (discontinued) and the recently released Varian Halcyon. The MV FBCT acquisition mode is available on Accuray Tomotherapy linacs[52, 53], with the use of Xenon-filled CT detectors as mentioned in section 5.1.2. The use of these modes is limited for the application in motion management, since the image is acquired prior to treatment in a static CT mode with a blur trajectory of the target motion. However, due to the limited soft tissue contrast of the MV imaging, this blur trajectory can hardly be seen. Therefore, this mode is mostly used for patient positioning only.

5.2 NON-RADIATION BASED SYSTEMS

Non-radiation based systems for monitoring and measuring target motion include camera-based, radiofrequency-based (RF), and ultrasound-based systems. Both camera-based systems and RF systems operate in very low frequency region of the EM spectrum, using light waves or RF waves, respectively. Ultrasound-based systems rely on sound-waves for imaging, but also incorporate infrared tracking technology for localization. Quality assurance for these systems has been mostly described in [54, 55].

5.2.1 CAMERA-BASED SYSTEMS

Camera-based systems can be categorized into stereoscopic imaging and monoscopic imaging based on the method of 3D reconstruction[54]. The former relies on two sensors to identify the relative geometry information of a feature and derives its 3D information through triangulation. The latter derives 3D geometry information of an object through a single sensor with added geometric data. Both of these systems can only be used for surrogate or surface monitoring.

The infrared tracking system, based on stereoscopic imaging, can efficiently extract feature (infrared marker) information and detect motions. The infrared markers are usually placed on patients' surface as motion surrogates. One typical example of this system is Real-time Position Management (RPM) (Varian Medical Systems, Palo Alto, CA), which is composed of an infrared tracking camera (mounted on the ceiling or the rear end of the couch) and a reflective infrared six-dot marker box (placed on patient's chest or abdomen where largest respiratory motion occurs). The system provides 3-dimensional respiratory motion waveforms by measuring the displacement of the box with respect to the origin. The use of this RPM device has been well described by Keall, *et al.* [5]. Other more complicated systems also incorporate this infrared technology to track motion, i.e. BrainLab ExacTrac

(section 5.1.3), or determine spatial coordinates of a motion tracking device, i.e. Calypso system (5.2.2) or SonArray US system (5.2.3).

Instead of using emissive or reflective fiducials as extracting features, video-based camera systems rely on the projected light pattern as known features and derive 3D information of the projecting object [56-58]. They are primarily used in surface guided radiotherapy, which compares real-time surface imaging of regions of interests with the skin rendering from patient's planning CT scan, and provides patient positioning accuracy, as well as real-time monitoring [51, 59]. The commercially available systems can be categorized based on their imaging triangulation method: stereoscopic imaging (VisionRT AlignRT and humediQ) and monoscopic imaging (Catalyst C-RAD). Stereoscopic imaging generates 3D surface through passive triangulation, which requires two video binocular cameras to acquire depth information of each structure point. Take the AlignRT system for example. The system needs 2 or 3 pods (depending on the version) to create a complete patient's surface image, as shown in Figure 17 A. Each pod consists of two data cameras for stereovision, one projector for continuous speckle projection, and one texture camera to capture a gray-scale image for visual information, as shown in Figure 17 B [57, 58]. The monoscopic imaging system, Catalyst C-RAD, only has one unit to generate a 3D surface image. This unit includes a high speed CMOS camera and a structured light projector, Figure 17 C. The latter projects coded stripe light patterns to patients' body, which can be captured by the high speed camera from a different angle. The depth information of the 3D surface can be calculated based on the angle-coded stripe patterns, thus the name active triangulation, Figure 17 D [60-62]. The clinical usages of these camera-based systems include initial patient setup and intra-fractional patient motion monitoring specifically on patient's surface [51, 56, 59, 63-65]. The surface images are shown in Figure 17 E from AlignRT system and Figure 17 F from the Catalyst C-RAD system.

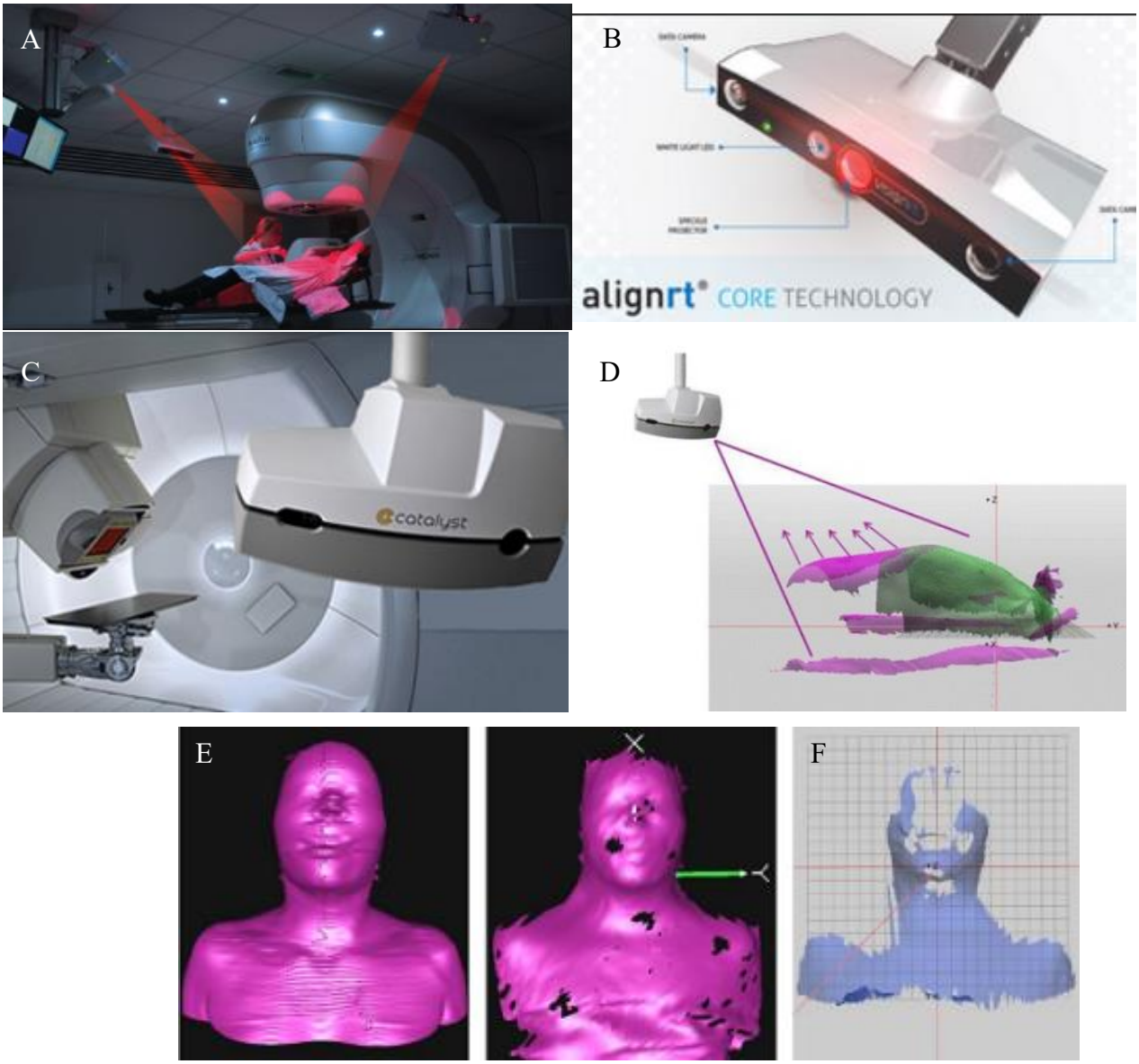

Figure 17. Room installation and device image for VisionRT (A and B) and Catalyst C-Rad (C and D). The surface images reconstructed by VisionRT (E) and Catalyst C-Rad (F).

5.2.2 RADIOFREQUENCY-BASED SYSTEM

The use of radio-frequency (RF) signals covers a variety of applications in radiology (i.e. MR imaging) and surgery (i.e. RF guided bronchoscopy, SuperDimension, Inc., Minneapolis,

MN). The latter can be of assistance in placing fiducials within the lung lesion for gated thoracic SBRT treatments, as shown in Figure 18 A and B[66]. The RF system operates based on the ability to detect one or more RF emitted coils that can be implanted in or on patients, or attached to a device. A current commercial radiofrequency system used for motion management is the Calypso system (Varian Medical Systems, Palo Alto, CA), Figure 18 C. The system consists of EM source coils, EM transponders (Beacon™), sensor array with infrared markers, and infrared cameras, Figure 18 D [67]. Prior to the treatment, the transponders (8 mm in length and 2 mm in diameter) are implanted inside or near the target (mostly used for prostate) by surgeons. Two or three transponders are usually used considering possible migrations in the patients' body. During the treatment, transponders are excited by the EM field from the EM source coils, and send out signals that can be detected by the sensor array. The coordinates of the transponders can be determined with respect to the sensor array position. The sensor array position with respect to the linac isocenter can be determined by the infra-red markers on the panel and the infra-red cameras. The overall coordinates of the transponders with respect to the linac isocenter can then be determined. These coordinates are updated at a rate of 10 Hz prior and during patients' treatment, in order to monitor and manage possible target motion, with proved submillimeter accuracy [68] and clinical benefits especially for prostate target tracking [69]. Despite the advantages, the Calypso system still has fundamental limitations due to RF signal interference with other magnetic fields or metal objects, as well as signal strength[54, 70]. Therefore, it may not be an option for patients with metal implants, pacemakers/defibrillators, and/or a separation between the transponder and array larger than 27 cm for localization and 23 cm for target tracking [67, 71]. Furthermore, even with patients who met the Calypso criteria, only 91% of those were actually appropriate for the Calypso system [71]. Calypso system also requires a special kVue™ couch to replace the conventional carbon fiber couch due to possible carbon fiber interference

with the signals. Other limitations include invasive surgery operation (thus surgeons' time) for placing the markers, marker migrations, etc.

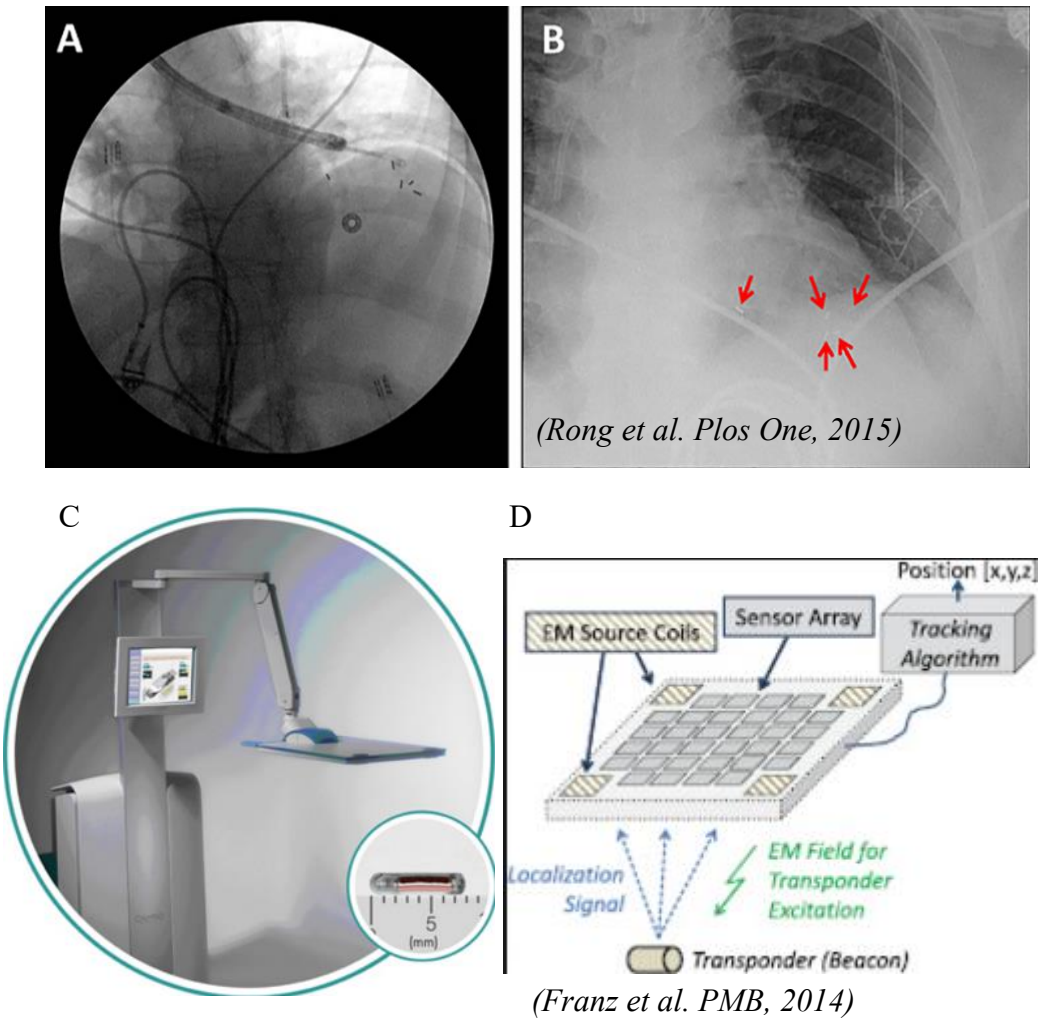

Figure 18. A and B show fiducial placements using RF guided bronchoscopy by SuperDimension (ref [66]); C and D show the Calypso system and its configurations (ref [70])

5.2.3 *ULTRASOUND BASED SYSTEMS*

The use of ultrasound (US) systems in patient setup and verification for radiotherapy began in the late 90s, when conventional films were the only resources for daily setup and patient positioning. US offers real-time volumetric image with soft-tissue contrast and no radiation to

patients. Its imaging technique limits the application to the pelvic, abdominal and breast sites. The Brightness-mode acquisition and targeting (BAT) system (Best Nomos, Pittsburgh, PA) provides 2D orthogonal US images of the treatment area to determine the target positional accuracy through matching the structure outlines from treatment plans, as shown in Figure 19 A and B. Its use has been intensively studied for prostate external beam treatment and results have demonstrated its superiority in reducing target misalignment due to internal organ motions [72-77]. Adapted from the 2D US system, 3D US imaging was proposed [78, 79] and can be formed through mechanical scanning, free-hand scanning with position-sensor, or electronic scanning with 2D matrix arrays. The most common approach in RT is optical tracking, which tracks the probe position via infrared markers or reflectors and ceiling-mount optical cameras. The commercial systems include SonArray (Varian Medical Systems, Palo Alto, CA), BATCAM (Best Nomos), Figure 19 C-E, and Clarity (Elekta Stockholm, Sweden, Figure 20 A), which were found to be superior to 2DUS in detecting internal target/organ displacements [59, 80-83]. However, their limitations are also non-trivial, which include inter-modality errors between CT and US, anatomical deformation caused by abdominal pressure, inter-user inconsistency from freehand probe sweeping, incompatibility for intra-fractional motion monitoring, etc. The Clarity system provides a solution to overcome the inter-modality inconsistency, by letting users to acquire a 3D US image at the time of CT sim and register to the planning CT. This allows users to determine patient setup and positioning errors based on the daily US image in the reference frame of the CT during treatment, Figure 20 B. In addition, the concept of 4D US has been proposed with the intra-fractional real-time monitoring as the fourth dimension. Clarity Autoscan system provides hands-free intra-fractional US monitoring through a static trans-perineal transducer housed within an Autoscan Kit, Figure 20 C and D, which motorizes the sweeping motion and enables a complete scan of 0.5s, 75 degree sweep [84, 85]. Furthermore, other robotic abdominal sweeping

systems for hands-free US scanning are being developed, which is also to overcome the limitation of performing inter- and intra-fractional target monitoring [86, 87]. A complete radiotherapy workflow with the use of US imaging in various steps are well summarized by Fontanarosa, *et al.* [88] and O'Shea, *et al.* [87]. A comparison of the available imaging modalities that can be used with SBRT is presented (Table 3).

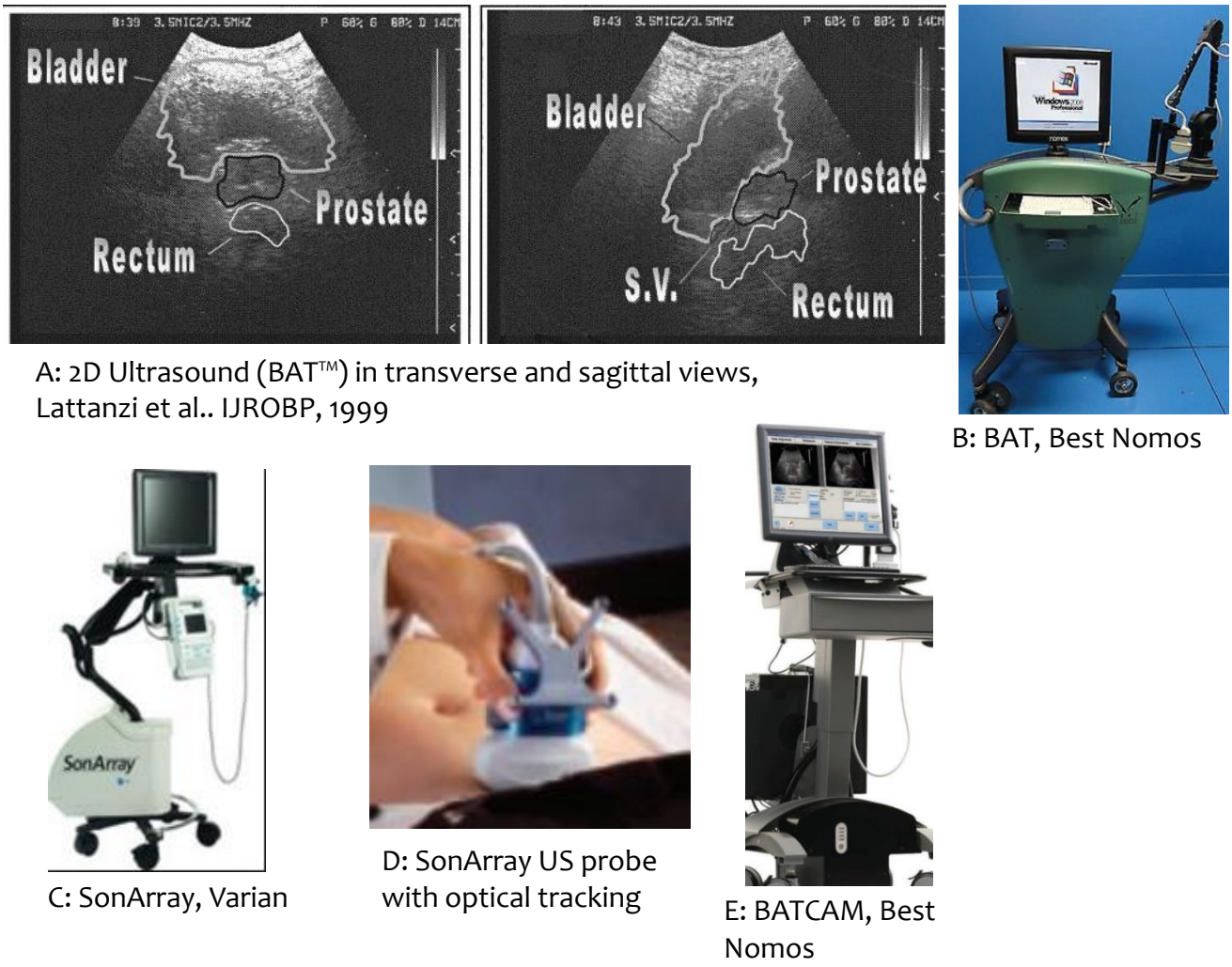

A: 2D Ultrasound (BAT™) in transverse and sagittal views, Lattanzi et al.. IJROBP, 1999

B: BAT, Best Nomos

C: SonArray, Varian

D: SonArray US probe with optical tracking

E: BATCAM, Best Nomos

Figure 19. A shows 2D orthogonal US images of the treatment area overlaid with the contoured structures from treatment plans; B-E show the BAT system, the SonArray system, the US probe with optical tracking markers, and BATCAM system.

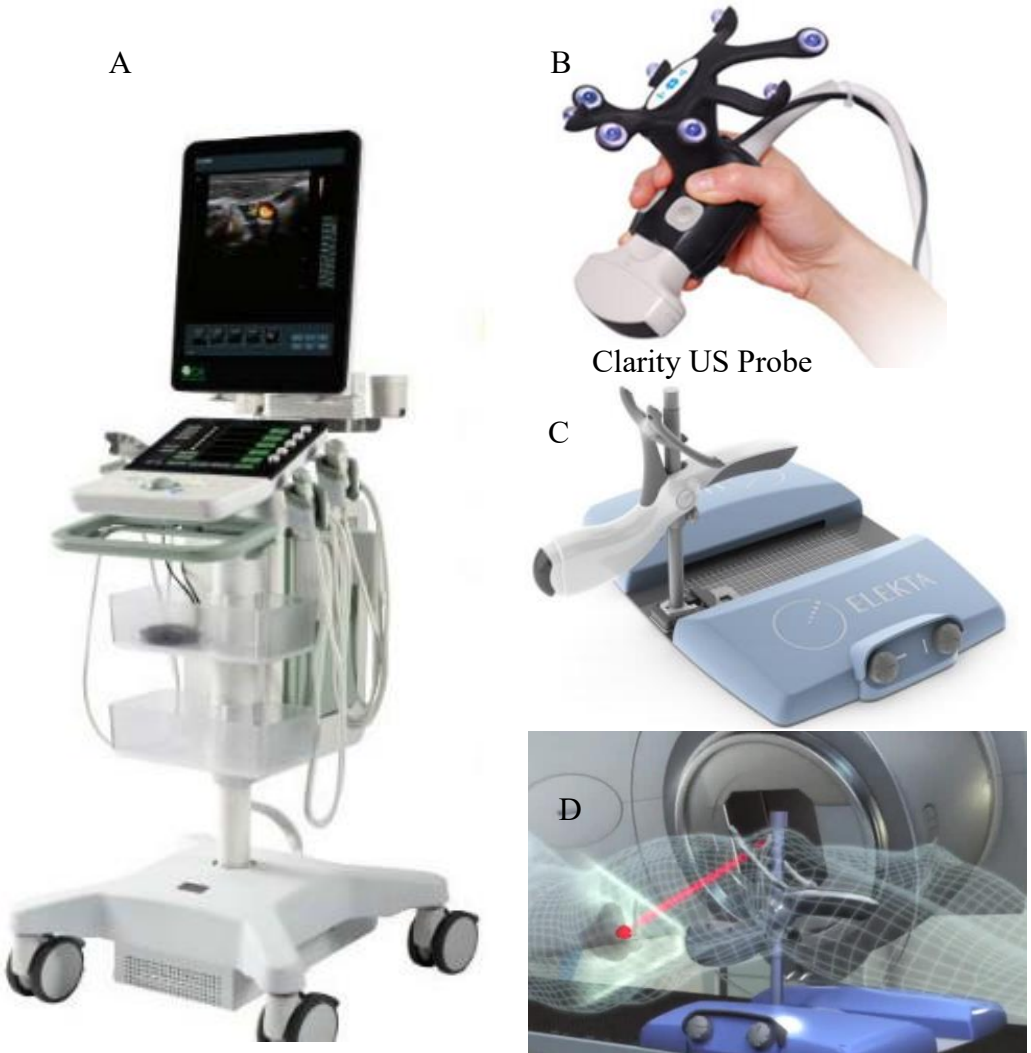

Figure 20. A-C show the Clarity system, the Clarity US probe, and the autoscan kit. D shows the system setup with patient on the table during treatment for intra-fractional motion monitoring.

Table 3. Comparison within various imaging modalities for their physical characteristics (CT refers to devices specific for RT (such as CBCT or CT-on-rails). Two cases are distinguished: when the beam is in the kV range (standard CT and kV cone beam CT (kV-CBCT)) and when it is in the MV range (MV-CBCT and Tomotherapy). MRI refers to the MR for guiding RT treatment. Adapted from Table 1, ref[87] with modifications.

Imaging modality	CT	US	MRI	2D kV/MV	Surface Imaging	Calypso/EM
Acquisition time (with setup/ preparation)	~2 min	~2 min	5 min	<1 min	<1min	8min
Spatial resolution	1–3 mm	Sub-mm	0.5–5 mm	~1 mm	Sub-mm	NO
Visualization capabilities	kVCT: soft tissue in the whole body. Whole body imaging MVCT: bone contrast only	Soft tissues: high contrast Difficult to image through air or bones (no lungs/brain)	Soft tissues: high contrast	2D, Poor contrast (only bones and fiducial markers)	Surface 3D (no internal organs)	Markers
Invasiveness	YES with fiducial markers or contrast	YES for some applications (intracavity) or using contrast	YES for special application with contrast	YES with fiducial markers or contrast	NO	YES with beacon transponders
Dose delivered	1–3 cGy (kV); 1–15 cGy (MV)	None	None	<1 cGy (kV); 6cGy (MV)	NO	NO
Operator dependence	NO	YES	NO	NO	YES (ROI selection)	NO
Inter-fraction motion monitoring	YES, 4D CT or 4D CBCT, kV	YES	YES, 2D	YES (fluoroscopy)	YES (surface only)	YES (Marker tracking)
Intra-fraction motion monitoring	NO	YES (with Clarity autoscan)	YES (Semi real-time)	YES (kV fluoroscopy or MV-Cine)	YES (surface only)	YES (real-time marker tracking)
Image distortion and artifacts	Streaking, beam hardening, scatter	Probe pressure, aberrations	Motion, metal parts, geometrical uncertainties depending on acquisition type	Streaking, low signal-to-noise ratio, motion	Partial image based on camera view, reflection, gantry blocking	No images, but signals can be affected by metal or carbon fiber
Functional/ biological information	YES	YES	YES	NO	NO	NO
Extra time for system setup and preparation	NO, unless contrast CT	YES	NO, unless contrast MRI	NO	NO	YES

5.2.4 MAGNETIC RESONANCE IMAGING LINEAR ACCELERATOR SYSTEMS

An emerging area of clinical radiotherapy is the introduction of integrated Magnetic Resonance Imaging Linear Accelerator (MRI-Linac) systems. MRI-Linacs combine the exquisite soft tissue imaging offered by MRI with the linac's radiotherapy targeting capabilities. This field was clinically pioneered by the ViewRay MRIdian device[89], a 0.35T MRI which initially was integrated with cobalt-60 radiation sources. In 2017, new MRIdian models replaced the cobalt-60 source with a linac and started treating patients. The MRIdian workflow involves pre-treatment volumetric MRI images with intra-treatment 2D planar images which can be used for gating the treatment beam based on the MRI-measured tumor position. The superior image quality offered by MRI has also enabled the introduction of online adaptive radiotherapy into routine clinical use[90]. In 2017 a prototype 1.5T Elekta Unity was first used to treat patients at Utrecht University[91], and it is anticipated that the use of the Unity will expand rapidly. The Alberta [92]and Sydney[93] groups have also built MRI-Linacs. It is anticipated that the role of MRI-Linacs in cancer radiotherapy will grow substantially over the next 10 years.

6 SUMMARY

Motion management in radiotherapy remains one of the most challenging technical aspects of radiation oncology, particularly for SBRT. Motion affects the imaging, treatment planning, set-up and delivery phases of the radiotherapy process. Motion adds time and complexity to the radiotherapy process. Motion varies between patients, between tumor sites, from day to day and from breath to breath. A variety of technology has been developed to measure motion and account for motion. In this chapter we have outlined the challenges, technology available and clinical processes for motion management in radiotherapy. The selection and

safe application of this technology requires a multidisciplinary team effort supported by experience, published guidelines, ongoing education and a strong quality assurance program. The complexity of current motion management offers opportunities for future innovations to make motion management safer, simpler and more time efficient.

BIBLIOGRAPHY

1. Benedict SH, Yenice KM, Followill D, Galvin JM, Hinson W, Kavanagh B, *et al*. Stereotactic body radiation therapy: the report of AAPM Task Group 101. Medical physics. 2010;37(8):4078-101.
2. Balter JM, Ten Haken RK, Lawrence TS, Lam KL, Robertson JM. Uncertainties in CT-based radiation therapy treatment planning associated with patient breathing. International Journal of Radiation Oncology* Biology* Physics. 1996;36(1):167-74.
3. Yamamoto T, Langner U, Loo BW, Shen J, Keall PJ. Retrospective analysis of artifacts in four-dimensional CT images of 50 abdominal and thoracic radiotherapy patients. International Journal of Radiation Oncology* Biology* Physics. 2008;72(4):1250-8.
4. Berger AJ, Mitchell RA, Severinghaus JW. Regulation of respiration. New England Journal of Medicine. 1977;297(2):92-7.
5. Keall PJ, Mageras GS, Balter JM, Emery RS, Forster KM, Jiang SB, *et al.* The management of respiratory motion in radiation oncology report of AAPM Task Group 76. Medical Physics. 2006;33(10):3874-900.
6. Lujan AE, Larsen EW, Balter JM, Ten Haken RK. A method for incorporating organ motion due to breathing into 3D dose calculations. Medical Physics. 1999;26(5):715-20.
7. George R, Vedam S, Chung T, Ramakrishnan V, Keall P. The application of the sinusoidal model to lung cancer patient respiratory motion. Medical physics. 2005;32(9):2850-61.
8. Seppenwoolde Y, Shirato H, Kitamura K, Shimizu S, Van Herk M, Lebesque JV, et al.. Precise and real-time measurement of 3D tumor motion in lung due to breathing and heartbeat, measured during radiotherapy. International Journal of Radiation Oncology* Biology* Physics. 2002;53(4):822-34.
9. Ruan D, Fessler JA, Balter J, Keall P. Real-time profiling of respiratory motion: baseline drift, frequency variation and fundamental pattern change. Physics in medicine and biology. 2009;54(15):4777.
10. Shah AP, Kupelian PA, Waghorn BJ, Willoughby TR, Rineer JM, Mañon RR, et al.. Real-time tumor tracking in the lung using an electromagnetic tracking system. International Journal of Radiation Oncology* Biology* Physics. 2013;86(3):477-83.
11. Ehrbar S, Jöhl A, Stieb S, Riesterer O, Stark L, Guckenberger M, et al.. PO-0926: Dosimetric comparison of different motion management techniques. Radiotherapy and Oncology. 2015;115:S482-S3.
12. Hugo GD, Rosu M. Advances in 4D radiation therapy for managing respiration: Part I–4D imaging. Zeitschrift für Medizinische Physik. 2012;22(4):258-71.
13. Landberg T, Chavaudra J, Dobbs J, Gerard J-P, Hanks G, Horiot J-C, et al.. Prescribing, Recording and Reporting Photon Beam Therapy (Supplement to ICRU report 50). 1999.
14. Stevens CW, Munden RF, Forster KM, Kelly JF, Liao Z, Starkschall G, et al.. Respiratory-driven lung tumor motion is independent of tumor size, tumor location, and pulmonary function. International Journal of Radiation Oncology* Biology* Physics. 2001;51(1):62-8.
15. Bradley JD, Nofal AN, El Naqa IM, Lu W, Liu J, Hubenschmidt J, et al.. Comparison of helical, maximum intensity projection (MIP), and averaged intensity (AI) 4D CT imaging for stereotactic body radiation therapy (SBRT) planning in lung cancer. Radiotherapy and oncology. 2006;81(3):264-8.
16. Underberg RW, Lagerwaard FJ, Slotman BJ, Cuijpers JP, Senan S. Use of maximum intensity projections (MIP) for target volume generation in 4DCT scans for lung cancer. International Journal of Radiation Oncology* Biology* Physics. 2005;63(1):253-60.
17. Wolthaus JW, Schneider C, Sonke J-J, van Herk M, Belderbos JS, Rossi MM, et al.. Mid-ventilation CT scan construction from four-dimensional respiration-correlated CT scans for radiotherapy planning of lung cancer patients. International Journal of Radiation Oncology* Biology* Physics. 2006;65(5):1560-71.
18. Guckenberger M, Wilbert J, Krieger T, Richter A, Baier K, Flentje M. Mid-ventilation concept for mobile pulmonary tumors: internal tumor trajectory versus selective reconstruction

of four-dimensional computed tomography frames based on external breathing motion. International Journal of Radiation Oncology* Biology* Physics. 2009;74(2):602-9.
19. Hanley J, Debois MM, Mah D, Mageras GS, Raben A, Rosenzweig K, et al.. Deep inspiration breath-hold technique for lung tumors: the potential value of target immobilization and reduced lung density in dose escalation. International Journal of Radiation Oncology* Biology* Physics. 1999;45(3):603-11.
20. Mah D, Hanley J, Rosenzweig KE, Yorke E, Braban L, Ling CC, et al.. Technical aspects of the deep inspiration breath-hold technique in the treatment of thoracic cancer. International Journal of Radiation Oncology* Biology* Physics. 2000;48(4):1175-85.
21. Dawson LA, Brock KK, Kazanjian S, Fitch D, McGinn CJ, Lawrence TS, et al.. The reproducibility of organ position using active breathing control (ABC) during liver radiotherapy. International Journal of Radiation Oncology* Biology* Physics. 2001;51(5):1410-21.
22. Lax I, Blomgren H, Näslund I, Svanström R. Stereotactic radiotherapy of malignancies in the abdomen: methodological aspects. Acta Oncologica. 1994;33(6):677-83.
23. Heinzerling JH, Anderson JF, Papiez L, Boike T, Chien S, Zhang G, et al.. Four-dimensional computed tomography scan analysis of tumor and organ motion at varying levels of abdominal compression during stereotactic treatment of lung and liver. International Journal of Radiation Oncology* Biology* Physics. 2008;70(5):1571-8.
24. Guckenberger M, Krieger T, Richter A, Baier K, Wilbert J, Sweeney RA, et al.. Potential of image-guidance, gating and real-time tracking to improve accuracy in pulmonary stereotactic body radiotherapy. Radiotherapy and Oncology. 2009;91(3):288-95.
25. Korreman SS, Juhler-Nøttrup T, Boyer AL. Respiratory gated beam delivery cannot facilitate margin reduction, unless combined with respiratory correlated image guidance. Radiotherapy and Oncology. 2008;86(1):61-8.
26. Sonke J-J, Rossi M, Wolthaus J, van Herk M, Damen E, Belderbos J. Frameless stereotactic body radiotherapy for lung cancer using four-dimensional cone beam CT guidance. International Journal of Radiation Oncology* Biology* Physics. 2009;74(2):567-74.
27. Dieterich S, Tang J, Rodgers J, Cleary K, editors. Skin respiratory motion tracking for stereotactic radiosurgery using the CyberKnife. International Congress Series; 2003: Elsevier.
28. Murphy MJ, editor Tracking moving organs in real time. Semin Radiat Oncol; 2004: Elsevier.
29. Depuydt T, Verellen D, Haas O, Gevaert T, Linthout N, Duchateau M, et al.. Geometric accuracy of a novel gimbals based radiation therapy tumor tracking system. Radiotherapy and Oncology. 2011;98(3):365-72.
30. Poulsen PR, Carl J, Nielsen J, Nielsen MS, Thomsen JB, Jensen HK, et al.. Megavoltage image-based dynamic multileaf collimator tracking of a NiTi stent in porcine lungs on a linear accelerator. International Journal of Radiation Oncology* Biology* Physics. 2012;82(2):e321-e7.
31. Booth JT, Caillet V, Hardcastle N, O'Brien R, Szymura K, Crasta C, et al.. The first patient treatment of electromagnetic-guided real time adaptive radiotherapy using MLC tracking for lung SABR. Radiotherapy and Oncology. 2016;121(1):19-25.
32. Keall PJ, Colvill E, O'Brien R, Ng JA, Poulsen PR, Eade T, et al.. The first clinical implementation of electromagnetic transponder-guided MLC tracking. Medical physics. 2014;41(2).
33. D'Souza WD, Naqvi SA, Yu C, X. . Real-time intra-fraction-motion tracking using the treatment couch: a feasibility study. Physics in Medicine and Biology. 2005;50(17):4021.
34. Wilbert J, Meyer J, Baier K, Guckenberger M, Herrmann C, Heß R, et al.. Tumor tracking and motion compensation with an adaptive tumor tracking system (ATTS): System description and prototype testing. Medical Physics. 2008;35(9):3911-21.
35. Tao S, Gu ZH, Nathan A. Fabrication of Gd2O2S:Tb based phosphor films coupled with photodetectors for x-ray imaging applications. Journal of Vacuum Science & Technology A: Vacuum, Surfaces, and Films. 2002;20(3):1091-4.
36. Fenwick JD, Tome WA, Soisson ET, Mehta MP, Rock Mackie T. Tomotherapy and other innovative IMRT delivery systems. Semin Radiat Oncol. 2006;16(4):199-208.

37. Keller H, Glass M, Hinderer R, Ruchala K, Jeraj R, Olivera G, et al.. Monte Carlo study of a highly efficient gas ionization detector for megavoltage imaging and image-guided radiotherapy. Med Phys. 2002;29(2):165-75.
38. Ross I Berbeco SBJ, Gregory C Sharp, George T Y Chen, Hassan Mostafavi and Hiroki Shirato. Integrated radiotherapy imaging system (IRIS): design considerations of tumour tracking with linac gantry-mounted diagnostic x-ray systems with flat-panel detectors. Phys Med Biol 2004;49:12.
39. Jin JY, Yin FF, Tenn SE, Medin PM, Solberg TD. Use of the BrainLAB ExacTrac X-Ray 6D system in image-guided radiotherapy. Med Dosim. 2008;33(2):124-34.
40. Christelle Gendrin HF, Christoph Weber. Monitoring tumor motion by real time 2D/3D registration during radiotherapy. Radiotherapy and Oncology. 2012;102:6.
41. Lin T, Cervino LI, Tang X, Vasconcelos N, Jiang SB. Fluoroscopic tumor tracking for image-guided lung cancer radiotherapy. Phys Med Biol. 2009;54(4):981-92.
42. Shirato H, Harada T, Harabayashi T, Hida K, Endo H, Kitamura K, et al.. Feasibility of insertion/implantation of 2.0-mm-diameter gold internal fiducial markers for precise setup and real-time tumor tracking in radiotherapy. International Journal of Radiation Oncology*Biology*Physics. 2003;56(1):240-7.
43. Tang X, Sharp GC, Jiang SB. Fluoroscopic tracking of multiple implanted fiducial markers using multiple object tracking. Phys Med Biol. 2007;52(14):4081-98.
44. Murphy MJ, Balter J, Balter S, BenComo JA, Jr., Das IJ, Jiang SB, et al.. The management of imaging dose during image-guided radiotherapy: report of the AAPM Task Group 75. Med Phys. 2007;34(10):4041-63.
45. Sheeba Thengumpallil KS, Pascal Monnin, Jean Bourhis, François Bochud, and Raphaël Moeckli1a. Difference in performance between 3D and 4D CBCT for lung imaging: a dose and image quality analysis. JOURNAL OF APPLIED CLINICAL MEDICAL PHYSICS,. 2016;17(6):9.
46. Yoganathan SA, Maria Das KJ, Mohamed Ali S, Agarwal A, Mishra SP, Kumar S. Evaluating the four-dimensional cone beam computed tomography with varying gantry rotation speed. Br J Radiol. 2016;89(1060):20150870.
47. Santoso AP, Song KH, Qin Y, Gardner SJ, Liu C, Chetty IJ, et al.. Evaluation of gantry speed on image quality and imaging dose for 4D cone-beam CT acquisition. Radiat Oncol. 2016;11:98.
48. Thengumpallil S, Smith K, Monnin P, Bourhis J, Bochud F, Moeckli R. Difference in performance between 3D and 4D CBCT for lung imaging: a dose and image quality analysis. J Appl Clin Med Phys. 2016;17(6):97-106.
49. Goyal S, Kataria T. Image guidance in radiation therapy: techniques and applications. Radiol Res Pract. 2014;2014:705604.
50. Warren K, Clare S. The effect of the Varian amorphous silicon electronic portal imaging device on exit skin dose. Physics in Medicine & Biology. 2003;48(19):3117.
51. Rong Y, Walston S, Welliver MX, Chakravarti A, Quick AM. Improving Intra-Fractional Target Position Accuracy Using a 3D Surface Surrogate for Left Breast Irradiation Using the Respiratory-Gated Deep-Inspiration Breath-Hold Technique. Plos One. 2014;9(5).
52. Chan M, Yang J, Song Y, Burman C, Chan P, Li S. Evaluation of imaging performance of major image guidance systems. Biomed Imaging Interv J. 2011;7(2):e11.
53. Yunfei Hu MB, Ben Archibald-Heeren, Matthew Squires, Amy Teh, Kylie Seiffert, Sonja Cheers, Yang Wang. A feasibility study on the use of tomotherapy megavoltage computed tomography images for palliative patient treatment planning. J Med Phys. 2017;42:7.
54. Willoughby T, Lehmann J, Bencomo JA, Jani SK, Santanam L, Sethi A, et al.. Quality assurance for nonradiographic radiotherapy localization and positioning systems: report of Task Group 147. Med Phys. 2012;39(4):1728-47.
55. Molloy JA, Chan G, Markovic A, McNeeley S, Pfeiffer D, Salter B, et al.. Quality assurance of U.S.-guided external beam radiotherapy for prostate cancer: report of AAPM Task Group 154. Med Phys. 2011;38(2):857-71.
56. Djajaputra D, Li SD. Real-time 3D surface-image-guided beam setup in radiotherapy of breast cancer. Medical Physics. 2005;32(1):65-75.

57. Bert C, Metheany KG, Doppke K, Chen GTY. A phantom evaluation of a stereo-vision surface imaging system for radiotherapy patient setup. Medical Physics. 2005;32(9):2753-62.
58. Siebert JP, Marshall SJ. Human body 3D imaging by speckle texture projection photogrammetry. Sensor Review. 2000;20(3):218-26.
59. Robinson D, Liu DR, Steciw S, Field C, Daly H, Saibishkumar EP, et al.. An evaluation of the Clarity 3D ultrasound system for prostate localization. J Appl Clin Med Phys. 2012;13(4):100-12.
60. Moore C, Lilley F, Sauret V, Lalor M, Burton D. Opto-electronic sensing of body surface topology changes during radiotherapy for rectal cancer. Int J Radiat Oncol. 2003;56(1):248-58.
61. Brahme A, Nyman P, Skatt B. 4D laser camera for accurate patient positioning, collision avoidance, image fusion and adaptive approaches during diagnostic and therapeutic procedures. Medical Physics. 2008;35(5):1670-81.
62. Stieler F, Wenz F, Shi M, Lohr F. A novel surface imaging system for patient positioning and surveillance during radiotherapy A phantom study and clinical evaluation. Strahlenther Onkol. 2013;189(11):938-44.
63. Pham NL, Reddy PV, Murphy JD, Sanghvi P, Hattangadi JA, Kim GY, et al.. Frameless, Real Time, Surface Imaging Guided Radiosurgery: Clinical Outcomes for Brain Metastases. Int J Radiat Oncol. 2015;93(3):E105-E.
64. Cervino LI, Pawlicki T, Lawson JD, Jiang SB. Frame-less and mask-less cranial stereotactic radiosurgery: a feasibility study. Physics in Medicine and Biology. 2010;55(7):1863-73.
65. Walter F, Freislederer P, Belka C, Heinz C, Sohn M, Roeder F. Evaluation of daily patient positioning for radiotherapy with a commercial 3D surface-imaging system (Catalyst (TM)). Radiat Oncol. 2016;11.
66. Rong Y, Bazan JG, Sekhon A, Haglund K, Xu-Welliver M, Williams T. Minimal Inter-Fractional Fiducial Migration during Image-Guided Lung Stereotactic Body Radiotherapy Using SuperLock Nitinol Coil Fiducial Markers. Plos One. 2015;10(7).
67. Balter JM, Wright JN, Newell LJ, Friemel B, Dimmer S, Cheng Y, et al.. Accuracy of a wireless localization system for radiotherapy. Int J Radiat Oncol. 2005;61(3):933-7.
68. Santanam L, Malinowski K, Hubenshmidt J, Dimmer S, Mayse ML, Bradley J, et al.. Fiducial-based translational localization accuracy of electromagnetic tracking system and on-board kilovoltage imaging system. Int J Radiat Oncol. 2008;70(3):892-9.
69. Litzenberg DW, Willoughby TR, Balter JM, Sandler HM, Wei J, Kupflian PA, et al.. Positional stability of electromagnetic transponders used for prostate localization and continuous, real-time tracking. Int J Radiat Oncol. 2007;68(4):1199-206.
70. Franz AM, Schmitt D, Seitel A, Chatrasingh M, Echner G, Oelfke U, et al.. Standardized accuracy assessment of the calypso wireless transponder tracking system. Phys Med Biol. 2014;59(22):6797-810.
71. Kimple RJ, Wallen EM, Pruthi R, Marks LB. A simple algorithm to assess patient suitability for Calypso-seed implantation for four-dimensional prostate localization. J Appl Clin Med Phys. 2010;11(1):252-62.
72. Lattanzi J, McNeeley S, Donnelly S, Palacio E, Hanlon A, Schultheiss TE, et al.. Ultrasound-based stereotactic guidance in prostate cancer--quantification of organ motion and set-up errors in external beam radiation therapy. Comput Aided Surg. 2000;5(4):289-95.
73. Trichter F, Ennis RD. Prostate localization using transabdominal ultrasound imaging. Int J Radiat Oncol. 2003;56(5):1225-33.
74. Kuban DA, Dong L, Cheung R, Strom E, De Crevoisier R. Ultrasound-based localization. Semin Radiat Oncol. 2005;15(3):180-91.
75. Fung AYC, Enke CA, Ayyangar KM, Raman NV, Zhen WN, Thompson RB, et al.. Prostate motion and isocenter adjustment from ultrasound-based localization during delivery of radiation therapy. Int J Radiat Oncol. 2005;61(4):984-92.
76. Lattanzi J, McNeeley S, Pinover W, Horwitz E, Das I, Schultheiss TE, et al.. A comparison of daily CT localization to a daily ultrasound-based system in prostate cancer. Int J Radiat Oncol. 1999;43(4):719-25.

77. Little DJ, Dong L, Levy LB, Chandra A, Kuban DA. Use of portal images and bat ultrasonography to measure setup error and organ motion for prostate IMRT: Implications for treatment margins. Int J Radiat Oncol. 2003;56(5):1218-24.
78. Fenster A, Downey DB. Three-dimensional ultrasound imaging. Annu Rev Biomed Eng. 2000;2:457-75.
79. Fenster A, Downey DB. Three-dimensional ultrasound imaging and its use in quantifying organ and pathology volumes. Anal Bioanal Chem. 2003;377(6):982-9.
80. Chinnaiyan P, Tome W, Patel R, Chappell R, Ritter M. 3D-ultrasound guided radiation therapy in the post-prostatectomy setting. Technol Cancer Res T. 2003;2(5):455-8.
81. Tome WA, Meeks SL, Orton NP, Bouchet LG, Bova FJ. Commissioning and quality assurance of an optically guided three-dimensional ultrasound target localization system for radiotherapy. Medical Physics. 2002;29(8):1781-8.
82. Peignaux K, Truc G, Barillot I, Ammor A, Naudy S, Crehange G, et al.. Clinical assessment of the use of the Sonarray system for daily prostate localization. Radiotherapy and Oncology. 2006;81(2):176-8.
83. Chandra A, Dong L, Huang E, Kuban DA, O'Neill L, Rosen I, et al.. Experience of ultrasound-based daily prostate localization. Int J Radiat Oncol. 2003;56(2):436-47.
84. Baker M, Behrens CF. Determining intrafractional prostate motion using four dimensional ultrasound system. Bmc Cancer. 2016;16.
85. Abramowitz MC, Bossart E, Flook R, Wu X, Brooks R, Lachaine M, et al.. Noninvasive Real-time Prostate Tracking Using a Transperineal Ultrasound Approach. Int J Radiat Oncol. 2012;84(3):S133-S.
86. Western C, Hristov D, Schlosser J. Ultrasound Imaging in Radiation Therapy: From Interfractional to Intrafractional Guidance. Cureus. 2015;7(6):e280.
87. O'Shea T, Bamber J, Fontanarosa D, van der Meer S, Verhaegen F, Harris E. Review of ultrasound image guidance in external beam radiotherapy part II: intra-fraction motion management and novel applications. Phys Med Biol. 2016;61(8):R90-137.
88. Fontanarosa D, van der Meer S, Bamber J, Harris E, O'Shea T, Verhaegen F. Review of ultrasound image guidance in external beam radiotherapy: I. Treatment planning and inter-fraction motion management. Phys Med Biol. 2015;60(3):R77-114.
89. Mutic S, Dempsey JF, editors. The ViewRay system: Magnetic resonance–guided and controlled radiotherapy. Semin Radiat Oncol; 2014: Elsevier.
90. Acharya S, Fischer-Valuck BW, Kashani R, Parikh P, Yang D, Zhao T, et al.. Online magnetic resonance image guided adaptive radiation therapy: first clinical applications. International Journal of Radiation Oncology• Biology• Physics. 2016;94(2):394-403.
91. Raaymakers B, Jürgenliemk-Schulz I, Bol G, Glitzner M, Kotte A, van Asselen B, et al.. First patients treated with a 1.5 T MRI-Linac: clinical proof of concept of a high-precision, high-field MRI guided radiotherapy treatment. Physics in Medicine & Biology. 2017;62(23):L41.
92. Fallone BG, editor The rotating biplanar linac–magnetic resonance imaging system. Semin Radiat Oncol; 2014: Elsevier.
93. Keall PJ, Barton M, Crozier S, editors. The Australian magnetic resonance imaging–linac program. Semin Radiat Oncol; 2014: Elsevier.

4

RESPIRATORY TRIGGERED 4D CONE-BEAM COMPUTED TOMOGRAPHY: A NOVEL METHOD TO REDUCE IMAGING DOSE

This chapter introduces the concept of respiratory triggered 4D cone-beam computed tomography (RT 4D CBCT), particularly the utilisation of a respiratory signal to "trigger" the projection acquisition. The study involves oversampling a thorax phantom with approximately 3600 projections from which subsets of projections are selected using the novel RT 4D CBCT technique and the conventional 4D CBCT technique. A study is made on the effects of image quality and imaging dose through varying acquisition parameters: acquisitions time, breathing period, and projection/imager frequency for both RT 4D CBCT and conventional 4D CBCT. The work presented in this chapter was published in *Medical Physics* in 2013.

Respiratory triggered 4D cone-beam computed tomography: A novel method to reduce imaging dose

Benjamin J. Cooper
Radiation Physics Laboratory, Sydney Medical School, University of Sydney, NSW 2006, Australia and Department of Medical Physics and Radiation Engineering, The Canberra Hospital, Canberra, ACT 2605, Australia

Ricky T. O'Brien
Radiation Physics Laboratory, Sydney Medical School, University of Sydney, NSW 2006, Australia

Salim Balik and Geoffrey D. Hugo
Radiation Oncology, Virginia Commonwealth University, 401 College Street, P.O.Box 980058, Richmond, Virginia 23298-0058

Paul J. Keall[a)]
Radiation Physics Laboratory, Sydney Medical School, University of Sydney, NSW 2006, Australia

(Received 7 October 2012; revised 11 February 2013; accepted for publication 14 February 2013; published 11 March 2013)

Purpose: A novel method called respiratory triggered 4D cone-beam computed tomography (RT 4D CBCT) is described whereby imaging dose can be reduced without degrading image quality. RT 4D CBCT utilizes a respiratory signal to trigger projections such that only a single projection is assigned to a given respiratory bin for each breathing cycle. In contrast, commercial 4D CBCT does not actively use the respiratory signal to minimize image dose.
Methods: To compare RT 4D CBCT with conventional 4D CBCT, 3600 CBCT projections of a thorax phantom were gathered and reconstructed to generate a ground truth CBCT dataset. Simulation pairs of conventional 4D CBCT acquisitions and RT 4D CBCT acquisitions were developed assuming a sinusoidal respiratory signal which governs the selection of projections from the pool of 3600 original projections. The RT 4D CBCT acquisition triggers a single projection when the respiratory signal enters a desired acquisition bin; the conventional acquisition does not use a respiratory trigger and projections are acquired at a constant frequency. Acquisition parameters studied were breathing period, acquisition time, and imager frequency. The performance of RT 4D CBCT using phase based and displacement based sorting was also studied. Image quality was quantified by calculating difference images of the test dataset from the ground truth dataset. Imaging dose was calculated by counting projections.
Results: Using phase based sorting RT 4D CBCT results in 47% less imaging dose on average compared to conventional 4D CBCT. Image quality differences were less than 4% at worst. Using displacement based sorting RT 4D CBCT results in 57% less imaging dose on average, than conventional 4D CBCT methods; however, image quality was 26% worse with RT 4D CBCT.
Conclusions: Simulation studies have shown that RT 4D CBCT reduces imaging dose while maintaining comparable image quality for phase based 4D CBCT; image quality is degraded for displacement based RT 4D CBCT in its current implementation. © *2013 American Association of Physicists in Medicine*. [http://dx.doi.org/10.1118/1.4793724]

Key words: 4D cone-beam computed tomography, imaging dose, respiratory motion, respiratory triggered

I. INTRODUCTION

Image guidance is a useful tool to reduce patient setup errors[1] in external beam radiation therapy and a steady rise in the use of image guidance has been reported.[2] An orthogonal pair of megavoltage or kilovoltage images just prior to a patient receiving radiotherapy can be utilized to correct for spatial discrepancy between the bony anatomy in the current state and a reference state, usually a set of digitally reconstructed radiographs from the planning CT dataset. Both megavoltage and kilovoltage imaging play important roles within the array of image guidance techniques[3] and accordingly, there is a sliding scale of imaging dose to the patient depending on the level of complexity of the image guidance technique.[4,5]

The advent of kilovoltage cone-beam computed tomography (3D CBCT) (Refs. 6 and 7) has provided the ability to discern soft tissue anatomy and thus a more detailed picture of interfraction and intrafraction organ motion and thereby an ability to detect and correct for more complex target positioning problems.

Due to the rotational speed limitations of kV imaging systems on linear accelerator gantries, conventional 3D CBCT acquisition gives rise to motion blurring[8,9] of moving organs, particularly those organs in the proximity of the

diaphragm (lungs, liver, kidney, etc.). This has been the motivation for the development of 4D CBCT which attempts to address the problem of respiration induced organ motion blurring by correlating the acquired projections with the respiratory signal.[10–12] 4D CBCT raises a problem of undersampling causing artifacts and some approaches employ slow gantry or multiple gantry rotations to increase projections[13] to address undersampling which potentially increases imaging dose. The use of daily image guidance using CBCT at treatment time in external beam radiation therapy has been shown to improve geometric accuracy in locally advanced lung cancer;[14] however, there is a trade-off between increasing imaging dose, both from the frequency and type of daily imaging, and the improvement in accuracy. Increased imaging from IGRT raises clinical concern and has motivated the development of novel iterative CBCT reconstruction algorithms which can use fewer projections leading to a 36-72 times reduction in imaging dose compared to a widely used head and neck scanning protocol.[15] The purpose of this work is to introduce and investigate a novel method called "respiratory triggered 4D CBCT" with the goal to reduce imaging dose. ICRP 73 poses the question, "Are there any reasonable steps I can take to improve protection?"[16] More recently, the "Image Wisely" and "Image Gently" campaigns have been established to address public concern of radiation in medical procedures for both the adult and pediatric populations. The stated objectives are "lowering the amount of radiation used in medically necessary imaging studies and eliminating unnecessary procedures" (http://www.imagewisely.org/About-Us - retrieved 2012-08-28) and "to change practice by increasing awareness of the opportunities to promote radiation protection in the imaging of children" (http://www.pedrad.org/associations/5364/ig/ - retrieved 2012-08-28), respectively. We will show that the proposed method can reduce imaging dose to the patient thus making a positive impact for these campaigns.

II. METHODS AND MATERIALS

In order to generate a phase-based 4D CBCT dataset from a linear accelerator imaging system, it is necessary to subdivide the acquired projection images into bins according to when the projection occurs during the patient's respiratory cycle. In phase based 4D CBCT, the respiratory cycle is typically subdivided into 6–10 time windows or bins. A side effect of the subdivision into bins is that the angular distribution of the projections in any given bin exhibits clustering. During reconstruction using FDK based algorithms, streaking artifacts have been reported due to this clustering effect.[17] To illustrate, in Fig. 1 we consider the angular distribution of the projections sorted into respiratory bin 1 over three respiratory cycles. During the first respiratory cycle, a number of consecutive projections separated by a small angle $\delta\theta$ will be sorted into bin 1. Time passes and acquired projections get sorted into the other bins (not shown). When the second respiratory cycle starts, the projections are again sorted into bin 1 but there is now a large angular gap $\Delta\theta$ between the first and second cluster of projections.

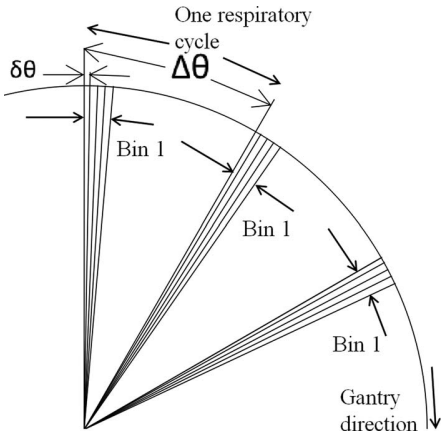

FIG. 1. Angular distribution of projections for bin 1 showing projection clustering. $\delta\theta$ is the angle between consecutive projections in bin 1; $\Delta\theta$ is the angular span travelled by the gantry in one respiratory cycle.

In this work, there were two arms of simulation studies undertaken:

1. a conventional 4D CBCT acquisition method with no respiratory signal feedback, referred to as "conventional 4D CBCT" throughout this paper where the imaging frequency is constant during acquisition representing current clinical systems;
2. the novel respiratory triggered 4D CBCT acquisition method, referred to as "RT 4D CBCT" where imaging frequency is variable and triggered based on the respiratory signal.

It should be noted that the RT 4D CBCT method requires an independent respiratory signal that is not derived from the imaging system acquiring the 4D CBCT. For simplicity, the respiratory signal is assumed to be a sine wave as studied in Ref. 18. Figure 2 illustrates the difference between a conventional 4D CBCT method [Figs. 2(a) and 2(b)] and the proposed respiratory triggered 4D CBCT method [Figs. 2(c) and 2(d)].

II.A. Conventional 4D CBCT

Figure 2(a) shows the sine wave respiratory signal over two cycles. The larger spacing vertical lines represent the subdivision of a cycle into 10 phase bins. The shaded vertical rectangles depict "Bin 1." Above the respiratory signal is a graphical depiction of the imaging system triggering at a constant rate of 5.5 Hz (densely spaced vertical bars). Note that the triggering frequency is fixed and has no feedback from the respiratory signal. Considering just the first bin in the cycle, the corresponding projection angles over three respiratory cycles are shown on the polar graph in Fig. 2(b). For clarity, the polar graph is scaled: one degree on the figure represents 0.1 degrees of gantry rotation.

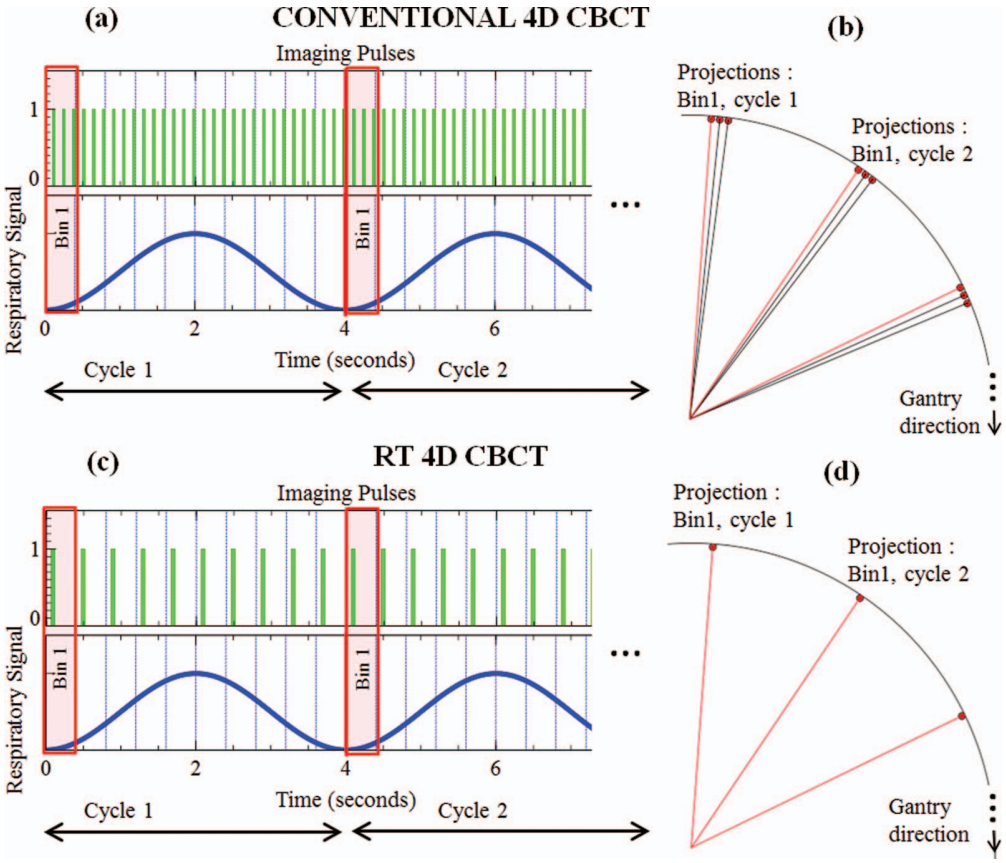

FIG. 2. Conventional 4D CBCT acquisition method [(a) and (b)] compared to RT 4D CBCT acquisition method [(c) and (d)]. Part (a) shows two 4 s respiratory cycles with a sinusoidal respiratory signal (lower) and a pulse train for the imaging system acquiring projections (upper). "Bin 1" is highlighted as the vertical shaded box. Part (b) shows the corresponding gantry angles for the clustered projections in "Bin 1" over three respiratory cycles. Part (c) is analogous to (a) except that the pulse train is only triggered once per respiratory phase bin in RT 4D CBCT and (d) shows the corresponding gantry angles for a single projection per respiratory phase bin.

II.B. Respiratory triggered 4D CBCT

Figure 2(c) shows how the imaging system triggering frequency is now controlled such that only one projection is triggered and acquired per phase bin per cycle illustrated by only one imaging system pulse per bin per cycle [vertical bars in Fig. 2(c)]. A reduction in the total number of projections is evident. The corresponding projection angles for the RT 4D CBCT method are shown on the polar graph in Fig. 2(d). Although Fig. 2 illustrates the RT 4D CBCT method for respiratory phase type bin sorting, the method can also be applied to respiratory displacement type bin sorting. Both respiratory phase and displacement type bin sorting will be discussed but the focus is on phase type bin sorting as this approach has been implemented commercially (Elekta, Kungstensgatan 18, SE-103 93 Stockholm).

II.C. Materials

A stationary thorax phantom was imaged using a linac based kV imaging system with the following parameters:

- 3600 projections;
- 200° span of gantry rotation;
- Full fan bowtie filter.

The set of projection images serves two purposes: (1) to generate a "ground truth" reconstruction CBCT dataset using a commercial FDK reconstruction package (COBRA, Exxim Computing Corporation, 3825 Hopyard Road, Suite 220, Pleasanton, CA 94588) for image comparison analyses and (2) to provide a large pool of projections from which the simulation program can select for the various simulation studies. Using 3600 projections essentially eliminates the introduction of angular sampling error during the simulation experiments. The largest possible sampling error is less than 0.028° using 3600 projections over a 200° span. This mode of projection acquisition is only available in a nonclinical mode of the linac's imaging system.

II.D. Phase based projection sorting experiment

A set of 4D CBCT simulation studies were performed to investigate the imaging dose and image quality using a conventional respiratory phase based 4D CBCT method and the RT 4D CBCT method. Acquisition time, breathing period, and imager frequency (frame rate) were varied. Acquisition time is varied by varying gantry speed over a fixed 200° span for acquisition. The parameter values for each simulation are summarized in Table I. Simulation 1 represents the

TABLE I. Parameter values for phase based sorting simulation studies. Bold type indicates the parameter varying.

Simulation number	Acquisition time (s)	Breathing period (s)	Imager frequency (Hz)
1	**240**	4.0	5.5
2	**120**	4.0	5.5
3	240	**2.1**	5.5
4	240	**6.7**	5.5
5	240	4.0	**10.0**

image acquisition parameters from a commercially available 4D CBCT system along with a rounded patient population mean breathing period of 4.0 s, based on the report by George *et al.*[18] To account for variations in breathing period, simulations were performed with 2.1 and 6.7 s representing the measured patient population for the 5th and 95th percentiles for free breathing.[18] For the acquisition time and imager frequency parameters, the variations are multiples of the representative commercial 4D CBCT acquisition parameters (simulations 2 and 5, Table I).

II.E. Displacement based projection sorting experiment

A further set of simulations was performed to investigate the imaging dose and image quality of the conventional 4D CBCT and the RT 4D CBCT using displacement based projection sorting rather than phase based sorting. We investigate changes in dose and image quality between displacement bins for all 10 bins. In this set, the acquisition parameters are fixed: acquisition time = 240 s; breathing period = 4 s; imager frequency = 5.5 Hz. Work by Abdelnour *et al.* gives a good general description of phase and amplitude (displacement) based projection sorting.[19]

II.F. Simulations

Using all 3600 projections as input to the cone-beam reconstructor program Cobra, a "ground truth" CT dataset was generated giving 160 CT slices (256 × 256 pixels/slice) spaced 1 mm apart. The same reconstruction parameters were used to generate the conventional 4D CBCT datasets and the RT 4D CBCT datasets. Figure 3 shows the work flow for the conventional 4D CBCT, the RT 4D CBCT, and the "ground truth" simulations.

II.G. Analysis

ImageJ (ImageJ version 1.46q, http://rsbweb.nih.gov/ij/) was used to calculate difference images. A difference image is defined to be the scalar difference between corresponding pairs of pixels in a pair of images of the same dimensions. An ImageJ macro was developed to calculate slice by slice difference images for all slices thus quantifying the overall average pixel difference values for:

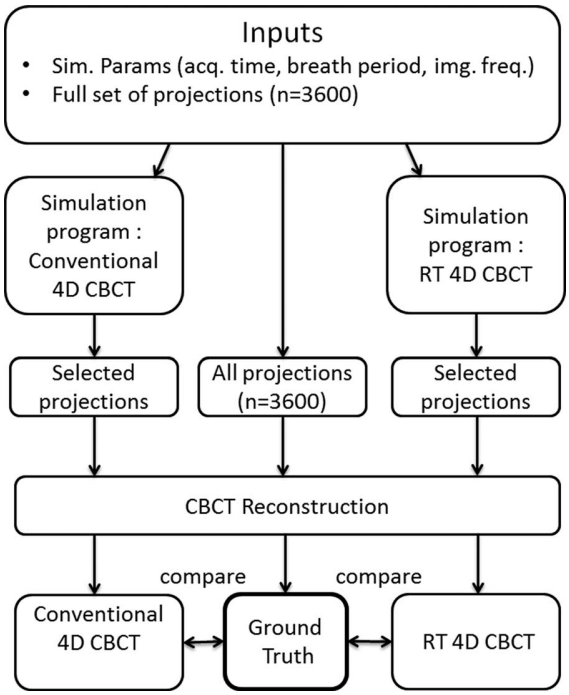

FIG. 3. Flow diagram showing schema for simulation experiments showing conventional 4D CBCT (left), ground truth (middle), and RT 4D CBCT (right). The ground truth (middle) is a CBCT reconstruction of all 3600 projections and is compared to the reconstructions from the conventional 4D CBCT (left) and the RT 4D CBCT (right).

1. ground truth and the conventional 4D CBCT;
2. ground truth and the respiratory triggered 4D CBCT methods.

The overall average pixel difference is defined as follows. The average pixel difference (diff_s) is the average value for the difference image and is given for a single slice as

$$\text{diff}_s = \frac{\sum_{a,b=1}^{N} |\text{pix}_a - \text{pix}_b|}{N},$$

where pix_a and pix_b are pixel values from image (a) and image (b); and N is the total number of pixels in the difference image. The overall average pixel difference is defined as

$$\text{Overall average pixel difference} = \frac{\sum_{i=1}^{S} \text{diff}_{s,i}}{S},$$

where S is the number of image slices in the dataset. The overall average pixel difference for each dataset is used as the metric for image quality. A higher value means that the test dataset is worse quality in the sense that it is farther from the ground truth.

Imaging dose was assessed assuming one projection equals one dose unit. Kim *et al.*[5] reported a measured dose of 7.68 mGy per 677 projections for a low dose thorax imaging CBCT protocol. Using this for an indicative imaging dose for the simulation studies gives approximately 11.3 μGy per projection. The number of projections resulting from the conventional 4D CBCT and the RT 4D CBCT simulations was counted to compare imaging dose.

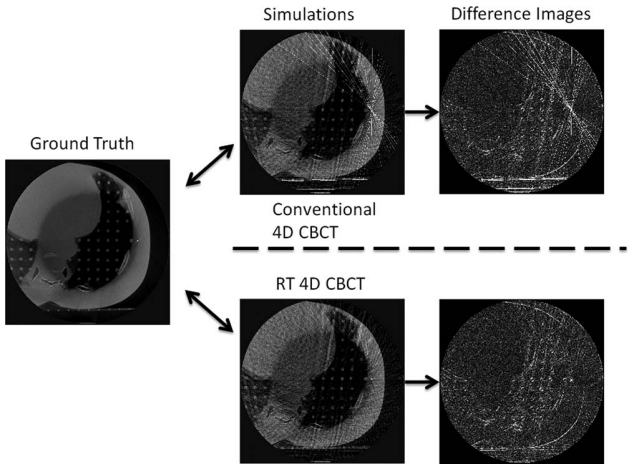

FIG. 4. The ground truth image (left) is compared to both the conventional 4D CBCT (top middle) and RT 4D CBCT images (bottom middle) using phase type projection sorting. The corresponding difference images are shown (right). Window and level settings are consistent for both conventional 4D CBCT and RT 4D CBCT.

III. RESULTS

III.A. Phase based projection sorting

The reconstruction images for simulation 1 (Table I) are shown in Fig. 4. Ground truth and simulation reconstructions and the resulting scalar difference images are shown left to right; top row is conventional 4D CBCT and bottom row is RT 4D CBCT.

The average pixel value differences for all simulations are shown in column pairs for both the conventional 4D CBCT and the RT 4D CBCT methods (left and right columns, respectively) in Fig. 5(a). One interpretation of the average pixel differences is a measure of how much the image (or set of images) under examination has been degraded from the ground truth image set. The corresponding comparisons in imaging dose are shown in Fig. 5(b). The simulations are grouped into three parameter groups corresponding to the three groups in Table I.

III.B. Displacement based projection sorting

The average pixel value differences and imaging dose differences for the effects of displacement type bin sorting using conventional and RT 4D CBCT methods are shown in Figs. 6(a) and 6(b), respectively.

IV. DISCUSSION

A new method, RT 4D CBCT, has been developed that substantially reduces imaging dose without degrading image quality for 4D CBCT that employs projection sorting by phase. Conceptually, the method is simple: take the patient respiratory signal and use this to trigger image acquisition. Qualitatively, Fig. 4 shows that there is not much difference between the conventional 4D CBCT images and the RT 4D CBCT images, apart from a notable star artifact that is more prominent around a fiducial marker in the conventional 4D CBCT images. For all three of the parameter groups, acquisition time, breathing period, and imager frequency, there are only small differences in image quality between conventional 4D CBCT and RT 4D CBCT. Conventional 4D CBCT shows a strong correlation between increased imaging dose as imaging frequency is increased with no clear improvement in imaging quality. Yet despite the comparable image quality, there is a marked saving in imaging dose with the RT 4D CBCT method showing roughly half or less the relative dose (and number of projections needed) compared to the 4D CBCT method with the exception of simulation 3 (2.1 s breathing period). A possible explanation for this result goes as follows. In Fig. 1 the projection sampling scheme for bin 1 is shown. There are essentially two sampling frequencies that are present--a higher sampling frequency for all the projections within a single cluster ($1/\delta\theta$) and a lower sampling frequency between clusters ($1/\Delta\theta$). Having two different sampling frequencies violates the assumption of equally spaced samples (projections) in the formulation of the FDK cone-beam reconstruction algorithm.[20] This, in turn, leads to streaking and star artifacts in the reconstructed images, especially as observed around highly attenuating material such as bone and fiducial markers. Another interpretation is that if $\delta\theta$ is very small, this implies only a very subtle change in the contents of those clustered projections. As there is very little "new" spatial information within a group of clustered projections, the high signal pixels in the projection (bone, fiducial markers, and highly attenuating material) tend to be reinforced along the ray line giving rise to streaks and star artifacts. The reason for this is that there are missing projections in the span ($\Delta\theta$, Fig. 1) and so the high signal pixels are not "balanced out" in the back projection process. In contrast, a conventional (nonbinned) 3D CBCT case has a complete set of projections in the span ($\Delta\theta$) and so streaking artifact is absent. The RT 4D CBCT method effectively removes the clustering effect thus removing the ($1/\delta\theta$) sampling frequency component and leaving only the ($1/\Delta\theta$) sampling frequency. As the angular sampling frequency becomes sparser, as might be the case for long period breathers (6.7 s), then the reconstructed images are further degraded because projection data sufficiency is not met. As RT 4D CBCT is a subset of the conventional method, both methods would suffer from a sparser angular sampling frequency.

For those patients where it might be indicated to use frequent CBCT image guidance for improved geometrical accuracy, as suggested by Higgins *et al.*,[14] any saving in imaging dose with minimal impact on image quality is desirable. RT 4D CBCT employing a phase based binning scheme offers a benefit in this situation. Other authors have shown that reducing tube current and longer CBCT acquisitions can improve 4D CBCT image quality.[13] Another approach to reducing imaging dose is through the use of iterative algorithms. The RT 4D CBCT method described in this paper could be coupled with non-FDK based reconstruction algorithms, like the GPU-based approach described,[15] to further optimize the use of imaging dose.

Figure 6 shows the average pixel difference and imaging dose, respectively, for each bin using a displacement based

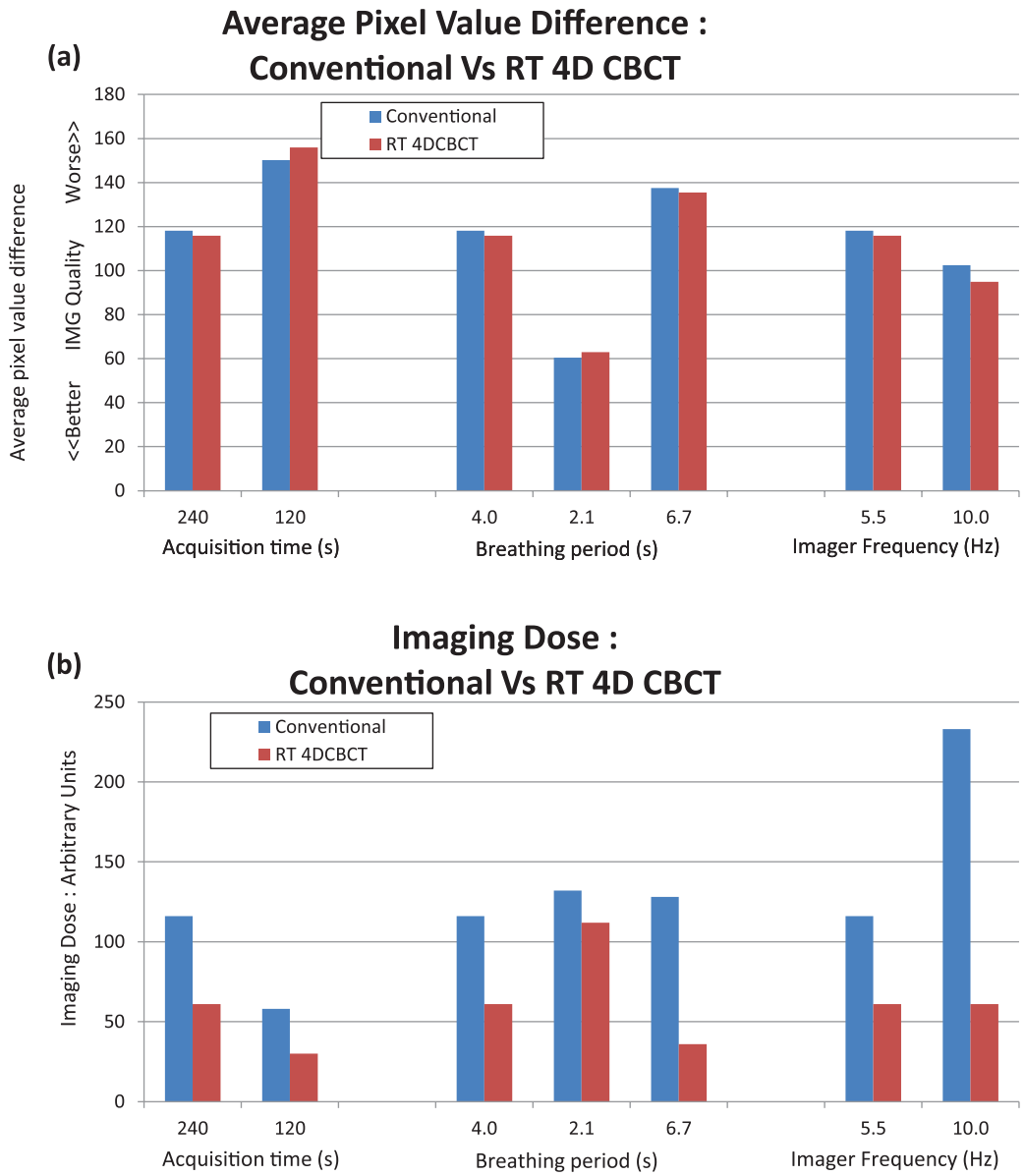

FIG. 5. Comparison of average pixel value difference [Fig. 5(a)] and imaging dose [Fig. 5(b)] for conventional 4D CBCT (left columns) and RT 4D CBCT (right columns) from the Ground Truth 4D CBCT dataset. In each group of three, the first left/right column pair is a repeat of the result from simulation 1 (Table I) which represents reference acquisition parameters from a commercial 4D CBCT system and an average breathing period. The latter column pairs in each parameter group show variations of that particular parameter group (acquisition time, breathing period, and imager frequency).

sorting method for both the conventional 4D CBCT and RT 4D CBCT. The conventional 4D CBCT exhibits marked variability in image quality across the ten bins with poorer image quality at the extremes (bins 1 and 10). Additionally, the imaging dose at these bins is highest. The reason for this is illustrated in Fig. 7. Both bins 1 and 10 show multiple projection acquisitions which cause the worst clustering effect. For the remaining bins, the clustering effect is greatly reduced and in some cases (bins 2 and 7, Fig. 6; bins 5 and 6, Fig. 7) it just so happens that only one projection per respiratory cycle is acquired. Here, the image quality and imaging dose for conventional 4D CBCT and RT 4D CBCT converge. The RT 4D CBCT image quality is fairly consistent across all ten bins. For bins 1, 2, 7, and 10, the average pixel difference is roughly in agreement (within 6 %) between conventional 4D CBCT and RT 4D CBCT. The imaging dose for bins 2 and 7 is correspondingly identical between conventional 4D CBCT and RT 4D CBCT; however, bins 1 and 10 suffer from clustering in conventional 4D CBCT and have a much higher dose than the RT 4D CBCT counterparts. The remaining bins show better image quality for conventional 4D CBCT but with correspondingly higher dose. By virtue of only one projection being allowed in the RT 4D CBCT, the imaging dose is consistent across all bins. This is illustrated in Fig. 8.

Why do bins 2 and 7 have the same imaging dose for both conventional 4D CBCT and RT 4D CBCT? This is explained by a chance happening that only one projection per respiratory cycle was sorted into bins 2 and 7 for this simulation. In fact,

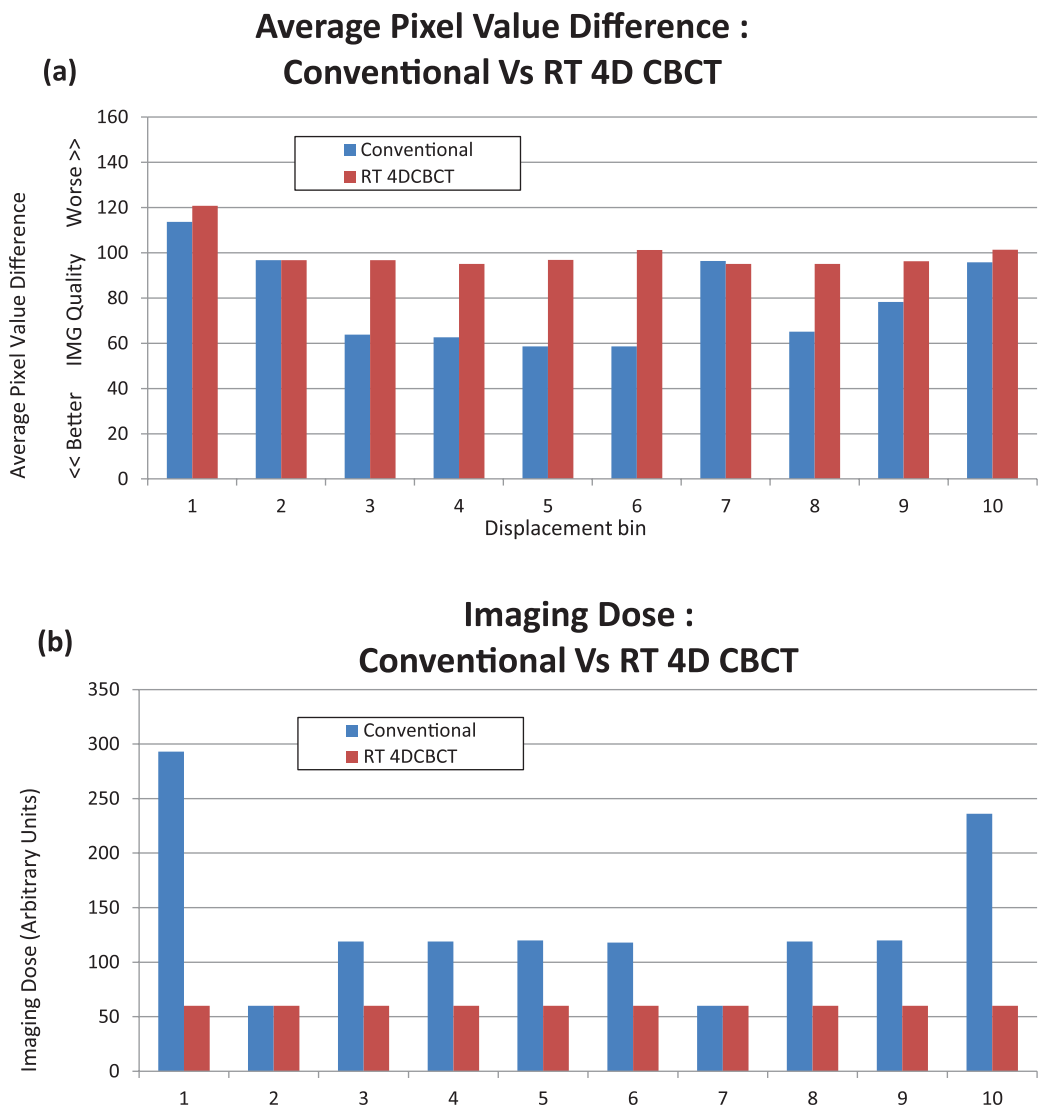

FIG. 6. (a) Comparison of average pixel value differences for conventional 4D CBCT and RT 4D CBCT from the Ground Truth 4D CBCT dataset for all 10 displacement bins. (b) The corresponding imaging dose for all 10 displacement bins.

this is actually what the RT 4D CBCT algorithm does for all bins. Depending on the interplay between imager frequency, breathing period, and acquisition time, it is also possible that no projections will be sorted into some displacement bins for one or more respiratory cycles. These "misses" will in turn lead to potentially unusable images for the affected displacement bins. The likelihood of projection "misses" would be exacerbated by irregular breathing. These problems are not solved by RT 4D CBCT at present because it is a subset of the conventional 4D CBCT acquisition. Further work is currently being pursued to overcome these problems. Controlling the imaging frequency according to an input respiratory signal creates another degree of freedom in how 4D CBCT can be acquired. Extending this idea, it is possible to trigger projections on the rising and falling part of the respiratory motion, instead of just once per bin per cycle which has been the focus of this work. This could offer better image quality for displacement type projection sorting, particularly for the most rapidly moving part of the respiratory motion. For example, projections could be triggered on the rise and fall of the respiratory signal for displacement bins 4, 5, 6, and 7, in Fig. 8. The imaging dose will of course increase, however. A more general approach to solve this optimization problem is currently being developed.

There are several limitations in this study. The choice of using a stationary phantom was to study the effects of projection clustering and the interplay of the acquisition time, breathing period, and imager frequency in isolation from the possible introduction of interference from a phantom undergoing respiratory motion. Additionally, a stationary phantom allows for a "ground truth" dataset for comparative analysis using difference images. It is expected that phantom motion will contribute to temporal blurring and reduce the image quality.[21] It is well known that breathing is anything but regular, in general. In this study we assume a sine wave for the respiratory signal with a reproducible period of 4 s. The

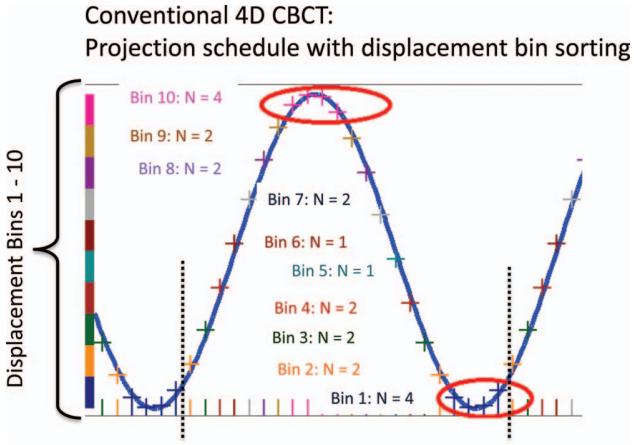

FIG. 7. Projection schedule for conventional 4D CBCT with displacement bin sorting over one respiratory cycle indicated with dashed vertical lines. Cross marks on the respiratory signal (sine wave) show how many projections will be sorted into displacement bins 1 through 10. Bins 1 and 10 exhibit the worst clustering effect.

sinusoidal model was chosen for simplicity and has been shown to be a reasonable model for respiratory motion which can exhibit moderate correlation to measured breathing signals.[18] A known challenge for both conventional and RT 4D CBCT is the ability to maintain regular/constant angle spacing between projections in the presence of an irregular respiratory signal. Irregular breathing is not dealt with in the current study in order to answer the question, "is there any benefit from the RT 4D CBCT method?" without the potentially confounding effects of irregular breathing. However, a practical implementation of RT 4D CBCT would have to address irregular breathing. A possible solution would be to detect irregularity through monitoring the breathing signal in near real time. If the gradient of the signal falls outside a reasonable threshold, the acquisition is paused. After breathing stabilizes, perhaps over the next few breathing cycles, the acquisition resumes. Other investigators have successfully implemented a beam "hold off" for projections during kV CBCT.[22] Pausing and restarting the linac gantry motion is achievable although considerations of inertia would probably require the gantry to rewind and resume acquisition at the right angular position and the right phase bin of the breathing trace. On a Varian linac, it is possible to stop and restart a conventional CBCT manually. Pausing and resuming gantry motion would need to be automated in the proposed RT 4D CBCT scheme. These simulation studies rely on the regularity of the respiratory period as it gives the ability to trigger a projection at a correspondingly regular angle between projections.

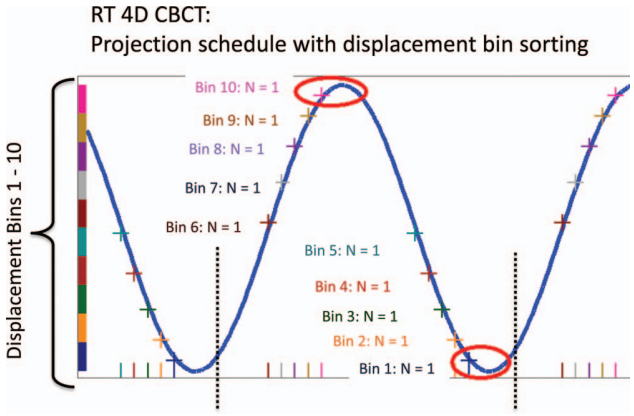

FIG. 8. Projection schedule for RT 4D CBCT with displacement bin sorting over one respiratory cycle indicated with dashed vertical lines. Cross marks on the respiratory signal (sine wave) show how only one projection will be sorted into displacement bins 1 through 10. One projection per bin per cycle guarantees no clustering.

V. CONCLUSION

A novel 4D CBCT acquisition method has been described and compared to a conventional 4D CBCT system. Imaging dose and image quality have been quantified for respiratory phase and displacement based projection sorting. The proposed RT 4D CBCT system simulations under phase based projection sorting showed that the imaging dose is roughly halved, regardless of acquisition time; imaging dose and image quality decrease with longer breathing periods; imaging dose remains constant despite increasing imager frequency. The proposed respiratory signal triggered 4D CBCT system can give comparable image quality to the conventional 4D CBCT system using fewer projections and thus less dose, simply by triggering the projection acquisitions according to an input respiratory signal. In principle, the RT 4D CBCT system could be implemented on existing linac systems through utilizing a respiratory signal to trigger projection acquisitions during 4D CBCT and eliminating projection clustering and thereby reducing imaging dose.

ACKNOWLEGDMENTS

The authors acknowledge Douglas J. Vile who helped with collecting experimental data. The authors acknowledge funding support from the Australian National Health and Medical Research Council (NHMRC) Project Grant, an NHMRC Australia Fellowship, and a US NIH/NCI Grant No. P01CA116602. Thanks to Julie Baz for reviewing and improving the clarity of the paper. A patent application (PCT/US2012/048693) has been lodged which is related to this work.

[a]Author to whom correspondence should be addressed. Electronic mail: paul.keall@sydney.edu.au; Telephone: +61 2 9351 3590.

[1]L. Pisani, D. Lockman, D. Jaffray, D. Yan, A. Martinez, and J. Wong, "Setup error in radiotherapy: On-line correction using electronic kilovoltage and megavoltage radiographs," Int. J. Radiat. Oncol., Biol., Phys. **47**, 825–839 (2000).
[2]D. R. Simpson, J. D. Lawson, S. K. Nath, B. S. Rose, A. J. Mundt, and L. K. Mell, "A survey of image-guided radiation therapy use in the United States," Cancer **116**, 3953–3960 (2010).
[3]L. A. Dawson and D. A. Jaffray, "Advances in image-guided radiation therapy," J. Clin. Oncol. **25**, 938–946 (2007).
[4]M. K. Islam, T. G. Purdie, B. D. Norrlinger, H. Alasti, D. J. Moseley, M. B. Sharpe, J. H. Siewerdsen, and D. A. Jaffray, "Patient dose from

kilovoltage cone beam computed tomography imaging in radiation therapy," Med. Phys. **33**, 1573–1583 (2006).
[5]S. Kim, S. Yoo, F.-F. Yin, E. Samei, and T. Yoshizumi, "Kilovoltage cone-beam CT: Comparative dose and image quality evaluations in partial and full-angle scan protocols," Med. Phys. **37**, 3648–3660 (2010).
[6]D. A. Jaffray, D. G. Drake, M. Moreau, A. A. Martinez, and J. W. Wong, "A radiographic and tomographic imaging system integrated into a medical linear accelerator for localization of bone and soft-tissue targets," Int. J. Radiat. Oncol., Biol., Phys. **45**, 773–789 (1999).
[7]D. Jaffray, J. H. Siewerdsen, J. Wong, and A. Martinez, "Flat-panel cone-beam computed tomography for image-guided radiation therapy," Int. J. Radiat. Oncol., Biol., Phys. **53**, 1337–1349 (2002).
[8]T. Li, L. Xing, P. Munro, C. McGuinness, M. Chao, Y. Yang, B. Loo, and A. Koong, "Four-dimensional cone-beam computed tomography using an on-board imager," Med. Phys. **33**, 3825–3834 (2006).
[9]M. Brehm, T. Berkus, M. Oehlhafen, P. Kunz, and M. Kachelriess, "Motion-compensated 4D cone-beam computed tomography," *IEEE Nuclear Science Symposium and Medical Imaging Conference (NSS/MIC)*, 3986–3993 (2011).
[10]L. Dietrich, S. Jetter, T. Tucking, S. Nill, and U. Oelfke, "Linac-integrated 4D cone beam CT: First experimental results," Phys. Med. Biol. **51**, 2939–2952 (2006).
[11]J.-J. Sonke, L. Zijp, P. Remeijer, and M. van Herk, "Respiratory correlated cone beam CT," Med. Phys. **32**, 1176–1187 (2005).
[12]T. Li, E. Schreibmann, Y. Yang, and L. Xing, "Motion correction for improved target localization with on-board cone-beam computed tomography," Phys. Med. Biol. **51**, 253–267 (2006).
[13]T. Li and L. Xing, "Optimizing 4D cone-beam CT acquisition protocol for external beam radiotherapy," Int. J. Radiat. Oncol., Biol., Phys. **67**, 1211–1219 (2007).
[14]J. Higgins, A. Bezjak, A. Hope, T. Panzarella, W. Li, J. B. Cho, T. Craig, A. Brade, A. Sun, and J. P. Bissonnette, "Effect of image-guidance frequency on geometric accuracy and setup margins in radiotherapy for locally advanced lung cancer," Int. J. Radiat. Oncol., Biol., Phys. **80**, 1330–1337 (2011).
[15]X. Jia, Y. Lou, R. Li, W. Y. Song, and S. B. Jiang, "GPU-based fast cone beam CT reconstruction from undersampled and noisy projection data via total variation," Med. Phys. **37**, 1757–1760 (2010).
[16]H. Smith, "Radiological protection and safety in medicine," Ann. ICRP **26**, 1–47 (1996).
[17]S. Leng, J. Zambelli, R. Tolakanahalli, B. Nett, P. Munro, J. StarLack, B. Paliwal, and G.-H. Chen, "Streaking artifacts reduction in four-dimensional cone-beam computed tomography," Med. Phys. **35**, 4649–4659 (2008).
[18]R. George, S. S. Vedam, T. D. Chung, V. Ramakrishnan, and P. J. Keall, "The application of the sinusoidal model to lung cancer patient respiratory motion," Med. Phys. **32**, 2850–2862 (2005).
[19]A. F. Abdelnour, S. A. Nehmeh, T. Pan, J. L. Humm, P. Vernon, H. Schöder, K. E. Rosenzweig, G. S. Mageras, E. Yorke, S. M. Larson, and Y. E. Erdi, "Phase and amplitude binning for 4D-CT imaging," Phys. Med. Biol. **52**, 3515–3529 (2007).
[20]L. A. Feldkamp, L. C. Davis, and J. W. Kress, "Practical cone-beam algorithm," J. Opt. Soc. Am. A **1**, 612–619 (1984).
[21]J. Lu, T. M. Guerrero, P. Munro, A. Jeung, P.-C. M. Chi, P. Balter, X. R. Zhu, R. Mohan, and T. Pan, "Four-dimensional cone beam CT with adaptive gantry rotation and adaptive data sampling," Med. Phys. **34**, 3520 (2007).
[22]M. van Herk, L. Ploeger, and J. J. Sonke, "A novel method for megavoltage scatter correction in cone-beam CT acquired concurrent with rotational irradiation," Radiother. Oncol. **100**, 365–369 (2011).

5

QUANTIFYING THE IMAGE QUALITY AND DOSE REDUCTION OF RESPIRATORY TRIGGERED 4D CONE-BEAM COMPUTED TOMOGRAPHY WITH PATIENT-MEASURED BREATHING

Following on from the introduction of the RT 4D CBCT algorithm where simple sinusoidal respiration signals were assumed, further study into how RT 4D CBCT performs utilising patient recorded respiratory signals is a necessary step on the pathway to implementation of RT 4D CBCT with an imaging system on a linear accelerator. In this chapter, a cohort of 111 breathing traces is utilised to create a simulated breathing motion using a digital phantom called XCAT. RT 4D CBCT and conventional 4D CBCT image reconstructions are produced and analyses including angular distribution of projections, imaging dose, and image quality are compared. The work was published in *Physics in Medicine and Biology* in 2015.

IOP Publishing | Institute of Physics and Engineering in Medicine Physics in Medicine & Biology

Phys. Med. Biol. **60** (2015) 9493–9513 doi:10.1088/0031-9155/60/24/9493

Quantifying the image quality and dose reduction of respiratory triggered 4D cone-beam computed tomography with patient-measured breathing

Benjamin J Cooper[1,2], Ricky T O'Brien[1], John Kipritidis[1], Chun-Chien Shieh[1] and Paul J Keall[1]

[1] Radiation Physics Laboratory, Sydney Medical School, University of Sydney, NSW 2006, Australia
[2] Department of Medical Physics and Radiation Engineering, The Canberra Hospital, Canberra, ACT 2605, Australia

E-mail: ben.cooper@act.gov.au

Received 10 September 2015
Accepted for publication 22 September 2015
Published 24 November 2015

Abstract

Respiratory triggered four dimensional cone-beam computed tomography (RT 4D CBCT) is a novel technique that uses a patient's respiratory signal to drive the image acquisition with the goal of imaging dose reduction without degrading image quality. This work investigates image quality and dose using patient-measured respiratory signals for RT 4D CBCT simulations. Studies were performed that simulate a 4D CBCT image acquisition using both the novel RT 4D CBCT technique and a conventional 4D CBCT technique. A set containing 111 free breathing lung cancer patient respiratory signal files was used to create 111 pairs of RT 4D CBCT and conventional 4D CBCT image sets from realistic simulations of a 4D CBCT system using a Rando phantom and the digital phantom, XCAT. Each of these image sets were compared to a ground truth dataset from which a mean absolute pixel difference (*MAPD*) metric was calculated to quantify the degradation of image quality. The number of projections used in each simulation was counted and was assumed as a surrogate for imaging dose. Based on 111 breathing traces, when comparing RT 4D CBCT with conventional 4D CBCT, the average image quality was reduced by 7.6% (Rando study) and 11.1% (XCAT study). However, the average imaging dose reduction was 53% based on needing fewer projections (617 on average) than conventional 4D CBCT (1320 projections). The simulation studies have demonstrated that the RT 4D CBCT method can potentially offer a 53% saving in imaging dose on average compared to conventional 4D CBCT in simulation studies using

0031-9155/15/249493+21$33.00 © 2015 Institute of Physics and Engineering in Medicine Printed in the UK

a wide range of patient-measured breathing traces with a minimal impact on image quality.

Keywords: radiation therapy imaging, 4D cone-beam computed tomography, respiratory signal

(Some figures may appear in colour only in the online journal)

1. Introduction

Four dimensional cone beam computed tomography (4D CBCT) is growing as a tool for assessing organ and target motion due to respiration on the day of treatment. Numerous reports have been published on the use of 4D CBCT to evaluate and reduce setup error and to monitor the tumour trajectory (Sonke *et al* 2008, Qi and Chen 2011, Sweeney *et al* 2012, Takahashi *et al* 2013). Unfortunately, in general there are problems that hinder the practical implementation of 4D CBCT imaging into routine clinical treatment which several authors summarize as: (i) increased acquisition time; (ii) increased imaging dose; and (iii) uneven projection distributions leading to view-aliasing and streaking in the reconstruction images (Leng *et al* 2008b, Rosu and Hugo 2012, Fast *et al* 2013). Furthermore, Fast *et al* point out that making an improvement in one of these problems tends to come at the cost of degrading one of the others (Fast *et al* 2013).

There has been a good deal of research to try and improve on these problems and a variety of strategies have been pursued. Earlier work has shown that a slow-gantry technique can improve image quality (Li and Xing 2007, Lu *et al* 2007) and accordingly acquisition time lengthens. Leveraging improvements in computational power, especially exploiting the capability of GPUs, has led to the exploration and development of iterative based algorithms with the goal of obtaining high quality CBCT images from under-sampled and noisy projection data as a consequence of reducing applied imaging dose (Jia *et al* 2010, 2011). Streak free, high temporal resolution image volumes from vastly undersampled cone-beam projections in conjunction with a fully sampled prior image have been reported using a custom PICCS algorithm (Leng *et al* 2008a). Ahmad *et al* showed that the most influential object parameter for 4D-CBCT performance is the period of motion of the object and published recommendations for minimum scan times according to object size and period of motion (Ahmad and Pan 2012). Brehm *et al* propose a motion-compensated reconstruction technique that does not use a prior planning CT image but instead applies a deformation based on estimated motion vector fields from all respiratory phases from the same imaging session thus removing any influence of anatomical changes between planning and treatment (Brehm *et al* 2011). Frustratingly, the problem of building a motion model from CBCT projection data is ill-posed (Rit *et al* 2009) as the motion models are generally sensitive to streak artifacts from undersampling. To help address this, Brehm *et al* model a patient specific undersampling artifact and then use this information to compensate for its effects on the motion vector field leading to imaging volumes of high quality (Brehm *et al* 2013). Zhang *et al* simulated a lung patient with anatomical changes between planning 4D-CT to onboard imaging. The prior 4D-CT scans were used in conjunction with limited angle onboard cone-beam projections to develop a motion modelled free-form deformation technique leading to improved accuracy in estimating target volume and centre of mass changes (Zhang *et al* 2013). Wang and Gu used the projections collected from on-treatment CBCT in a 'warm start', two step optimization process that deforms the planning CT without the need for a prior motion model of the patient, aiming to produce high quality 4D-CBCT (Wang and Gu 2013).

Another approach to improving 4D CBCT involves incorporating a breathing signal as a feedback into the control systems responsible for acquiring projections. Fast *et al* demonstrated an experimental 4D CBCT acquisition technique that takes a breathing signal, either external motion sensor or electromagnetic transponder based, and actively triggers desirable projections to efficiently utilize dose and eliminate motion blurring from sinusoidal trajectories in anthropomorphic lung phantom studies (Fast *et al* 2013). Kincaid *et al* have developed a gated CBCT technique that focusses on acquiring narrowly spaced projections for up to a 30% 'on' gated window using a programmed gantry motion that 'rewinds' the gantry position to continue acquisition where it left off at the end of the last 'on' gated window (Kincaid Jr *et al* 2013). O'Brien *et al* presented an optimization algorithm that responds to a respiratory signal with the aim of obtaining evenly spaced projections for all respiratory bins by allowing a constrained variation on gantry velocity and variation on projection frequency (O'Brien *et al* 2013, 2014).

In this space, we introduced a method, 'Respiratory Triggered' 4D CBCT (RT 4D CBCT). In RT 4D CBCT, a single projection is triggered once per respiratory bin per breathing period. Using this method, imaging dose can be reduced and image quality maintained using synthetic, regular sinusoidal breathing signals (Cooper *et al* 2013). The effects of breathing irregularities can impact on the performance of 4D CBCT (Lu *et al* 2007). This is why we make the crucial step towards clinical implementation of RT 4D CBCT in this work by investigating RT 4D CBCT's performance using real patient-measured breathing traces with the accompanying irregularities and unpredictable behaviour of the breathing signals. We compare image quality and estimated imaging dose using the RT 4D CBCT acquisition method and a conventional 4D CBCT acquisition method using the same patient-measured breathing trace in each case.

2. Methods

2.1. Theory of RT 4D CBCT and conventional 4D CBCT simulations

A brief explanation for RT 4D CBCT and its main difference from conventional 4D CBCT is presented for completeness but a detailed description of the RT 4D CBCT method can be found in a previously reported study with sinusoidal motion (Cooper *et al* 2013).

Trajectories for a kV source during an RT 4D CBCT (A) and a conventional (B) acquisition session are represented (figure 1). Just the projections collected for phase-bin 1 are shown.

We see the central idea of RT 4D CBCT (figure 1(A)) is that only one projection is allowed to be triggered per phase bin per breath. In contrast, during a conventional 4D CBCT acquisition (figure 1(B)) the projections are triggered at a constant rate with no feedback from the patient's respiratory signal resulting in tightly grouped clusters of projections.

There are two arms to this study: the RT 4D CBCT arm and the conventional 4D CBCT arm. The work flow for the simulation experiments in this study is illustrated (figure 2). The overview here is expanded upon in the following sections. In the current study, each of 111 lung cancer patient breathing traces are used to drive 111 pairs of separate simulations of an image acquisition session using the RT 4D CBCT method (figure 2, left) and another image acquisition session using the conventional 4D CBCT method (figure 2, right). Each simulation set of projection images is sent to a commercial FDK (Feldkamp *et al* 1984) reconstructor program, Cobra[3]. The resulting images from each method are compared against a ground truth dataset from which the mean absolute pixel difference error (*MAPD*) and the imaging doses are reported.

[3] Exxim Computing Corporation, Pleasanton, CA.

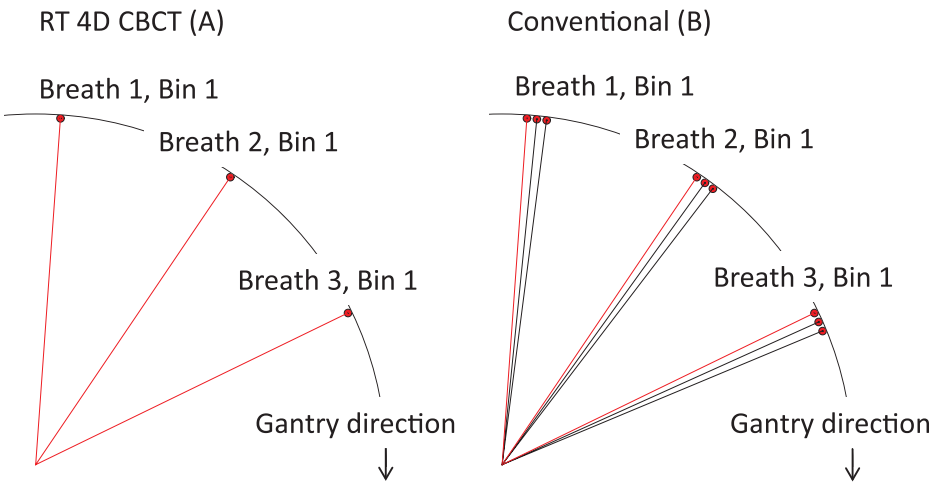

Figure 1. Projection schedule, phase-bin 1 for RT 4D CBCT (A) and conventional 4D CBCT (B).

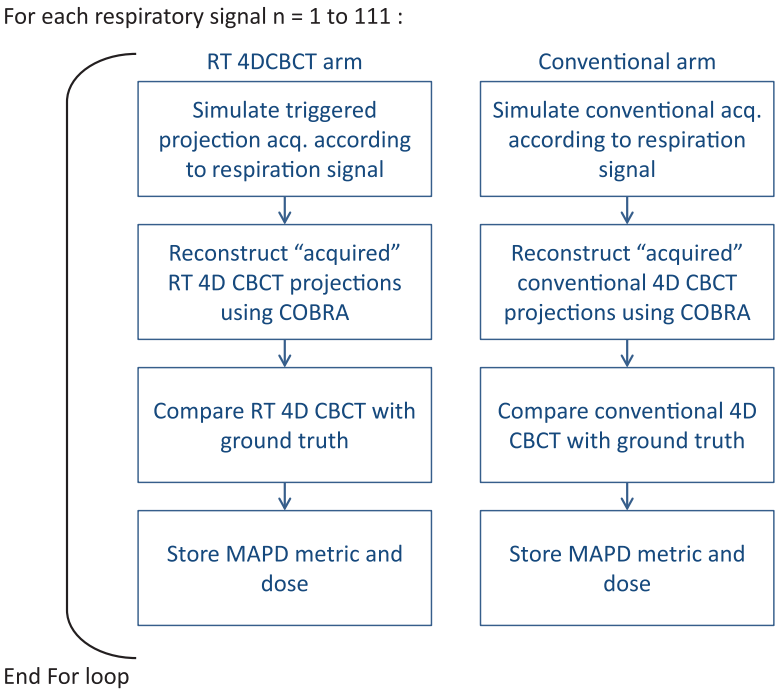

Figure 2. Flow chart of the RT 4D CBCT and conventional 4D CBCT simulation arms.

2.2. Patient-measured breathing data

Breathing data in the form of external marker position data from 111 RPM files from 24 lung cancer patients measured under free breathing conditions in a previous study were utilized (George *et al* 2006). The data were used as an input driver for the RT 4D CBCT algorithm and used to break down the conventional 4D CBCT acquisition into 10 bins in the simulation experiments (figure 2).

2.3. RT 4D CBCT and conventional simulation software

The first box (figure 2, top, left), is expanded upon here to describe how the RT 4D CBCT module works. Simulation software has been built in-house which allows the study and simulation of 4D CBCT imaging techniques. This software platform was built for flexibility to allow different software implementations of image acquisition optimization modules. This allows the experimenter to enable or disable various combinations of algorithms for a given set of simulations. The RT 4D CBCT software module was built to accept a respiratory signal, specifically RPM data[4] (version 1.4) as an input data stream. The studies use the recorded *.dat RPM files which contain the real-time phase estimates, not the *.vxp files which have phase re-calculated. The *.dat files represent phase estimations that are commercially achievable in a real-time system. The data is formatted as a comma separated list with the first three positions in a single line being: (i) detected displacement of marker block; (ii) respiratory phase (range 0–2π); (iii) time stamp. The marker block is an external surrogate for tumour motion which can lead to small time shifts and amplitude mismatches; however, Ionascu *et al* have shown that the superior-inferior internal-external motion is well correlated in a small 10 patient study (Ionascu *et al* 2007). Numerous other works have investigated the correlation between tumour/organ motion and various surrogates (table 3, Keall *et al* (2006). Never the less, it is expected that there will be some patients amongst the cohort of 111 where marker correlation is poor potentially degrading image quality. The RT 4D CBCT algorithm takes an incoming respiratory signal and triggers based on the conditions outlined (figure 3). The RPM data is 'read in' in close to real-time to model as closely as possible the data stream that would be present in a real world clinical situation. As the respiratory signal data frames arrive (approximately every 33 ms), the software determines to which phase-bin the current signal frame belongs (b_{now}, figure 3) by reading the respiratory phase from the data frame. If b_{now} has changed from the previous signal frame, and we do not already have a projection in this bin for this breath, we trigger a projection, otherwise wait for the next signal frame. This continues until the end of the simulation run for this breathing trace. This is now repeated for each of 111 breathing traces (the outer loop, figure 2). One purpose for using the phase data directly 'as-is' from the RPM data stream without any post processing is for simplicity of implementation with the RPM system in widespread clinical use. Abdelnour *et al* describe some of the behaviours and limitations of the RPM system in detail (Abdelnour *et al* 2007).

The conventional 4D CBCT simulation runs (figure 2, right) are simulated using the same software platform but with the RT 4D CBCT module switched off. Referring to figure 3, switching off the RT 4D CBCT module is equivalent to skipping the numbered sections 2–4. The respiratory signal is now simply used to divide the projections into respiratory phase-bins for each of the 111 breathing traces.

2.4. Experiments: ground truth, RT 4D CBCT and conventional acquisition simulations with RANDO phantom

Rando phantom studies were carried out to investigate the behaviour of the RT 4D CBCT acquisition technique driven by an irregular breathing signal. The benefit in using the static Rando phantom is that the effect of the irregular breathing signal on the projection triggering can be determined in isolation from the confounding effects of a moving tumour on image quality. See Shrimpton *et al* (1981) for details regrding the tissue equivalence of the Rando phantom for kilovoltage x-rays.

[4] Varian Medical Systems, Palo Alto, CA.

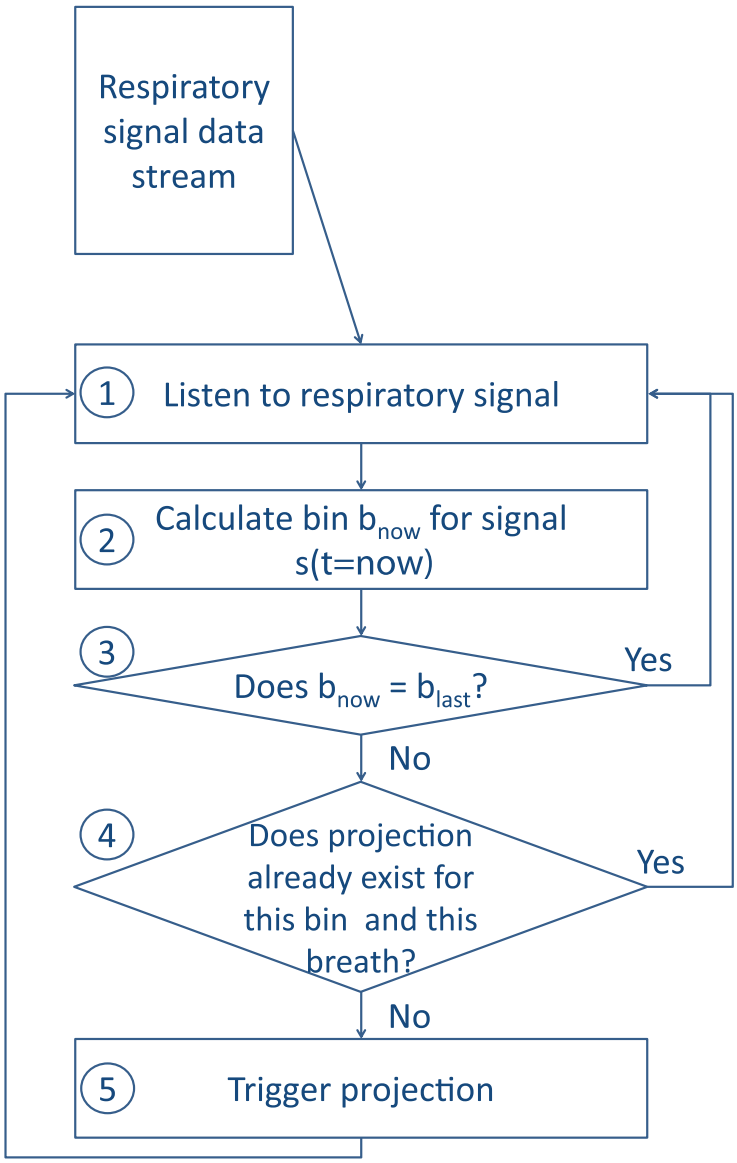

Figure 3. Algorithm controlling projection acquisition for RT 4D CBCT.

2.4.1. Ground truth data. A CBCT projection dataset from the thorax region of a static Rando phantom was collected using a very fine angular spacing (0.056°). This is the ground truth image dataset. It contains roughly 3600 projections over a 200 degree gantry sweep.

2.4.2. RT 4D CBCT and conventional 4D CBCT simulations. The RT 4D CBCT and conventional 4D CBCT simulations are 'synthetic' as they select projections according to the input respiratory signal from the static projections collected in section 2.4.1. All conventional 4D

CBCT simulations are based on the acquisition parameters used from a commercially available 4D CBCT system[5] as listed by Giaddui *et al* (2013):

- 200° span of gantry sweep;
- 240 s acquisition time;
- Imaging frequency of 5.5 Hz.

For the RT 4D CBCT simulations, only the imaging frequency is varied in accordance with the input respiratory signals; the acquisition time and gantry speed are the same as for the conventional simulations. For each simulation we collect data for the following properties: (i) how many projections were used; (ii) the angle of each projection (range: 0–200°); (iii) the respiratory bin of each projection (range: 1–10). For each of the simulated projections we find the closest matching 'real' projection from the Rando CBCT projection set (section 2.4.1) based on the simulation projection angles, and send those projections via a batch file to the Cobra CBCT reconstruction platform to reconstruct the simulation CBCT images.

2.5. Experiments: RT 4D CBCT and conventional acquisition simulations with XCAT phantom

The behaviour of the RT 4D CBCT acquisition technique and effect on image quality in the presence of irregular breathing and tumour motion was investigated using the XCAT digital phantom.

2.5.1. XCAT phantom set up. The XCAT digital phantom (Segars *et al* 2010) was configured to model a breathing patient. Existing RPM breathing signal data files were used as a data source for a representative spherical tumour motion and diaphragm motion within the capabilities of the XCAT tool kit. The XCAT studies are included to determine the performance of the RT 4D CBCT method under conditions that attempt to represent a breathing patient *in silico*. The XCAT phantom has been used in these experiements to investigate these effects on image quality for both RT 4D CBCT and conventional 4D CBCT. It is necessary to use the XCAT phantom to understand the variations in tumour motion that comes from breathing patients.

During the course of a clinical 4D CBCT acquisition, projections are acquired as the patient breathes and the RPM system records displacement of the marker block. As a model for breathing, the displacement parameter from the RPM signal has been translated and normalized into a thoracic 'breathing' motion with a 2 cm superior-inferior range and 0.5 cm anterior-posterior range using the XCAT software. The minimum and maximum RPM displacement signal has been re-scaled to 0 cm and 2 cm tumour displacement respectively giving a 2 cm superior-inferior tumour excursion which is synchronised with the diphragm motion.

To illustrate this, the marker block displacement is plotted (figure 4). The dots represent where projections are acquired for a selected mid-inhale phase. The spread of dots is reflective of the difficulties in calculating real-time phase which leads to intermittent assignment of the gating phase interval to an incorrect portion of the respiratory trace (Santoro *et al* 2009). The simulations incorporate these difficulties associated with real-time phase calculation and the accompanying inconsistencies of tumour motion by directly using the real-time RPM data. We have used the real-time phase signal from the RPM system because it is in current use for clinical gating systems. The real-time phase from the RPM system is known to contain significant errors (Santoro *et al* 2009); however, the work of Ruan *et al* (2009) on real-time phase calculation methods demonstrate improvements that would help address these issues.

[5] Elekta Symmetry.

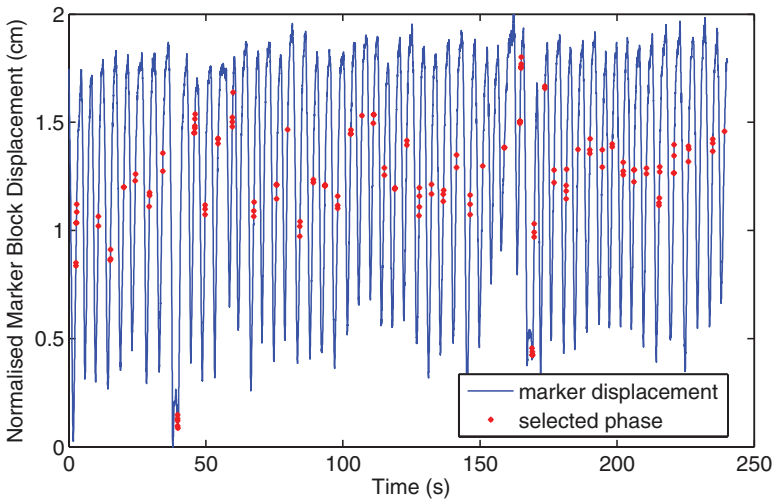

Figure 4. RPM marker displacement with dots representing where projections are taken for a selected mid-inhale phase.

A set of 50 'snapshot' 3D XCAT digital phantoms with the moving tumour embedded was created. If end-exhale is snapshot 1 with tumour displacement = 0.0 cm and end-inhale is snapshot 50 with tumour displacment = 2.0 cm, then each of the 50 snapshots steps up the tumour in 0.4 mm gradations from end-exhale to end-inhale giving a finely spaced set of tumour positions in the XCAT phantoms to sample the tumour motion. The normalized displacement values from each of the 111 breathing traces were used to select the appropriate XCAT 'snapshot' from the set of 50 XCAT phantoms thus giving the modelled instantaneous diaphragm and tumour position. The resulting series of XCAT snapshots effectively provide a model of diaphragm and tumour motion for a given RPM file. The 'ground truth' image for the XCAT simulations is taken to be the tumour in the middle of its trajectory between inhale and exhale and is taken from the middle of the range of the set of 50 XCAT phantoms. It is a deliberate choice not to include intra-phase blur in the XCAT ground truth to try and highlight the expected intra-phase blur resulting from both the conventional and RT 4D CBCT simulations.

2.5.2. RT 4D CBCT and conventional 4D CBCT XCAT simulations. A forward projection of each snapshot XCAT phantom for a given phase bin was generated to simulate the collection of an on-board imaging system projection frame using the RTK software suite (Rit *et al* 2014). Consider a single x-ray beamlet from the kV source: an upper limit intensity value is set to 65 535 ($2^{16} - 1$) representing no attenuation at all. As the beamlet passes through the XCAT phantom, the linear attenuation is determined and the resulting intensity value is registered as a pixel on the projection image. Image noise is modelled as Poisson noise via the Matlab function *imnoise*[6]. In this manner, a complete set of x-ray projections is collected simulating the acquisition that occurs during a 4D CBCT imaging session of a breathing patient. Photon scatter from the kV source traversing through the phantom has not been considered. In an effort to capture the time snap, or phase-bin where the image reconstructions are likely to be the blurriest due to maximal instantaneous tumour motion, the phase-bin that sits half way

[6] MATLAB and Image Processing Toolbox, Release 2012b, The Mathworks, Inc.m Natick, Massachusetts, United States.

between inhale and exhale was chosen for projection collection. These projections were then fed in to the Cobra reconstruction engine to produce the CBCT image reconstructions.

2.5.3. RT 4D CBCT and equivalent dose conventional 4D CBCT XCAT simulations. The conventional 4D CBCT simulations were repeated but using the same number of projections as the corresponding RT 4D CBCT simulations. This is referred to as *equivalent dose conventional 4D CBCT* (EqD Conventional). These simulations could only be run retrospectively once the number of projections (imaging dose) was known for each of the 111 RT 4D CBCT simulations. Then for a given simulation, the EqD Conventional fixed triggering frequency is calculated by:

$$Triggering\ Frequency = \frac{N_{\text{proj}}}{240} \tag{1}$$

Triggering Frequency is given in Hz where N_{proj} is the number of projections from the RT 4D CBCT simulation and 240 is the number of seconds for the acquisition.

2.6. Image metrics: mean absolute pixel difference from ground truth (MAPD), image gradient and dose

All images were reconstructed using Cobra which outputs CT images with default, un-calibrated Hounsfield Unit (HU) gray scale, referred to as raw pixel gray level in this study. The mean absolute pixel difference (*MAPD*) is defined as the mean scalar pixel value difference between the ground truth CT image dataset and the RT 4D CBCT or conventional reconstructed CT image dataset. It is defined as follows:

$$MAPD = \frac{\sum_{i=1}^{N} |GT_i - X_i|}{N} \tag{2}$$

where N is the total number of pixels in a CT dataset, GT_i is the intensity of pixel i in a ground truth image dataset and X_i is the intensity of pixel i from either an RT 4D CBCT or conventional 4D CBCT reconstructed image dataset. Henceforth, *MAPD* always means the mean absolute pixel difference as defined here and it is always with respect to the ground truth CBCT image dataset. It has units of raw pixel gray level.

For the XCAT simulations, the change in pixel value in the superior-inferior (y) direction in a vertical line through the centre of the spherical tumour on a coronal image (f) was calculated. We define this as the superior-inferior image gradient and represent it simply as *SupInf*:

$$SupInf = \frac{\partial f}{\partial y} \tag{3}$$

The *SupInf* image gradient metric is chosen to focus on the tumour motion induced blurring of the image reconstructions. It is interpreted to describe the image sharpness of the tumour in the direction of the tumour motion. A sharper image of the tumour corresponds to a well defined peak-and-trough in the image gradient plot as is expected in a ground truth image with no tumour motion; a less sharp image will have a less well defined peak-and-trough gradient plot.

The total number of projections was counted for each simulation and it is assumed that one projection equals one arbitrary unit of imaging dose. As an indication of dose, Kim *et al* (2010) report that a low dose thorax imaging CBCT protocol with 677 projections gave a measured dose of 7.68 mGy.

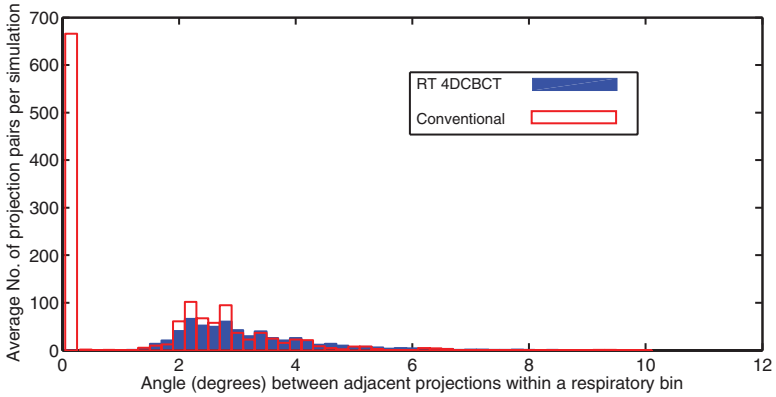

Figure 5. Angular distribution of adjacent projections for all bins over all paired 111 RT 4D CBCT and conventional simulations.

3. Results

3.1. Angular separation of adjacent projections: distributions for RT 4D CBCT and conventional 4D CBCT

The distributions of angular separation between adjacent projections for all bins and all 111 breathing traces are shown for RT 4D CBCT and conventional 4D CBCT simulations (figure 5). The static Rando thorax phantom data is used here to study the effects on projection angular distribution and image quality from irregular breathing traces without the confounding effect of tumour motion. The striking feature of the conventional distribution is that it shows a large peak of adjacent projections in the first histogram bin with a small angular spacing. It represents projection 'doubling up' whereby two projections are acquired in the same bin with only a very small angular spacing ($\leqslant 0.2°$). In this scenario, the second projection within that bin is redundant and gives rise to extra imaging dose without much benefit. In contrast, the RT 4D CBCT method ensures that this doubling up of projections is avoided.

3.2. Mean absolute pixel difference from reference ground truth (MAPD)

The distributions of the *MAPD* for the RT 4D CBCT and conventional simulations from the 111 breathing traces are represented with boxplots for the Rando phantom data (figure 6) and the XCAT phantom data (figure 7).

The median values of the *MAPD* in units of raw pixel gray level value for RT 4D CBCT and conventional are 113.9 and 101.5 (Rando studies), 59.2 and 53.5 (XCAT studies) respectively; the corresponding mean values of *MAPD* are 119.2 and 110.8 (Rando studies), 65.1 and 58.6 (XCAT studies). Wilcoxon signed rank tests on the RT 4D CBCT and conventional *MAPD* distributions from the Rando and XCAT studies give a p-value $p < 0.001$ for both meaning that there are significant differences in the median values from the RT 4D CBCT and conventional datasets. Although statistically significant, the mean *MAPD* for RT 4D CBCT is only 7.6% worse than conventional for the Rando studies and 11.1% worse than conventional for the XCAT studies, taking conventional as the reference in both cases.

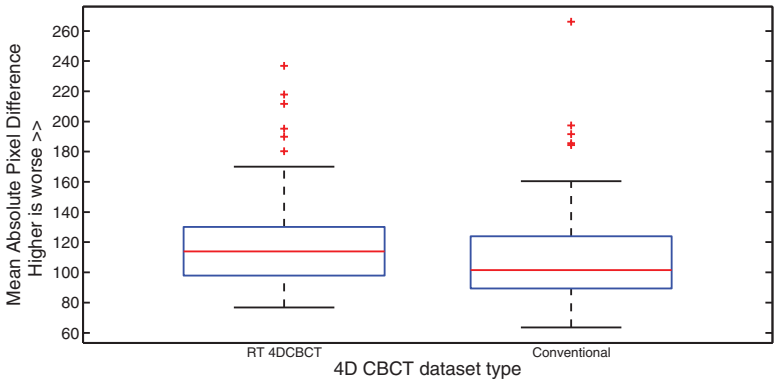

Figure 6. Comparison of RT 4D CBCT and conventional image quality (*MAPD* from ground truth) for Rando studies.

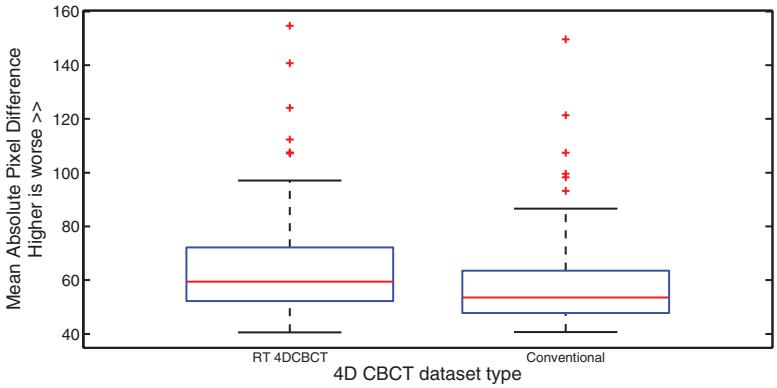

Figure 7. Comparison of RT 4DCBCT and conventional image quality (*MAPD* from ground truth) for XCAT studies.

3.3. Image quality (MAPD from ground truth) versus dose

The image quality (*MAPD* from ground truth) versus imaging dose (or number of projections) for the 111 breathing traces used in the Rando and XCAT simulation studies are plotted respectively (figures 8–10). The open circles and squares represent the RT 4D CBCT and conventional acquisition methods respectively. For the RT 4D CBCT dataset, the number of projections (imaging dose) corresponding to the 25th, 50th and 75th percentile of *MAPD* are 486, 616, and 761 for the Rando studies (figure 8) and 492, 620, 770 for the XCAT studies (figure 9) respectively. The conventional simulations give an imaging dose that is fixed at 1320 projections for both the Rando and XCAT studies (figures 8 and 9). The equivalent dose conventional simulations have the same dose as the RT 4D CBCT simulations, by design (figure 10).

There are clear savings in imaging dose using the RT 4D CBCT method with only a 7.6% and 11.1% reduction in image quality on average for the Rando and XCAT studies respectively (figures 8 and 9). Interestingly, when conventional XCAT simulations are repeated and 'clamped' to the same dose as the RT 4D CBCT simulations, the relationship between imaging quality and imaging dose takes on the same $1/x$ like shape as that for RT 4D CBCT

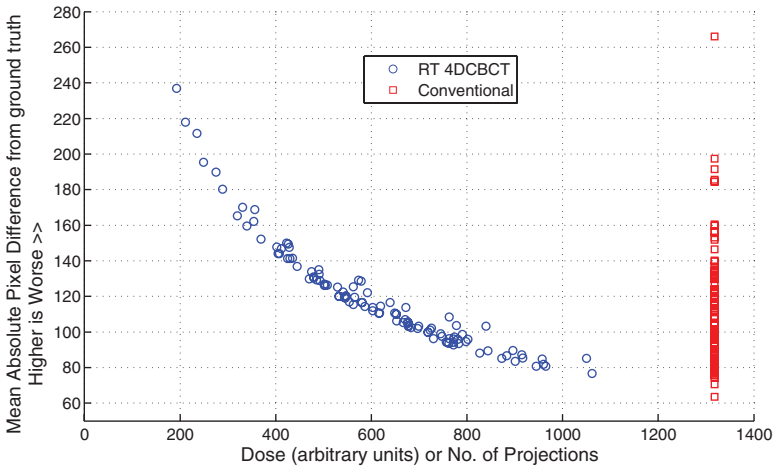

Figure 8. Image quality (*MAPD*) versus dose for RT 4D CBCT and conventional for Rando studies.

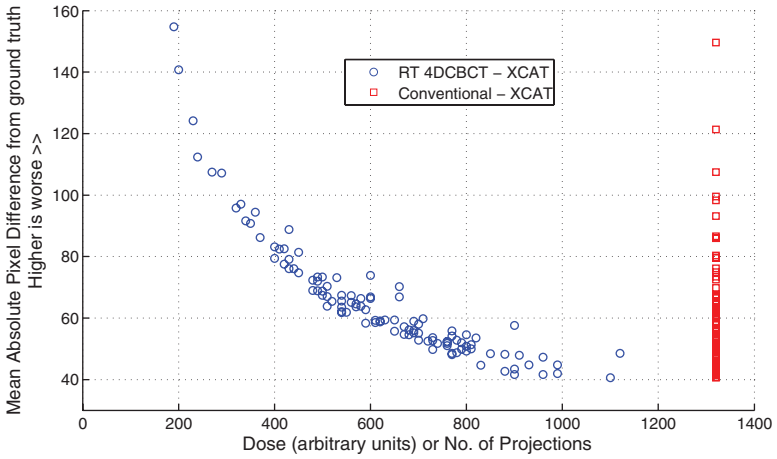

Figure 9. Image quality (*MAPD*) versus dose for RT 4D CBCT and conventional for XCAT studies.

(figure 10). Curve fitting was performed using a Matlab *power2* curve fitting model[7]. R-square values for RT 4D CBCT and EqD Conventional are 0.964 and 0.627 respectively, indicating a greater spread for the EqD Conventional data.

To try and visualize what a 7.6% reduction in image quality means qualitatively, CBCT reconstructions for RT 4D CBCT and conventional are shown (figure 11, top and bottom row respectively). Left to right shows representative images from the 25th, 50th, and 75th percentile of *MAPD*. It is apparent that there is very little difference comparing the top row (RT 4D CBCT) to the bottom row (conventional).

[7] MATLAB Curve Fitting Toolbox 3.3, The Mathworks, Inc.m Natick, Massachusetts, United States.

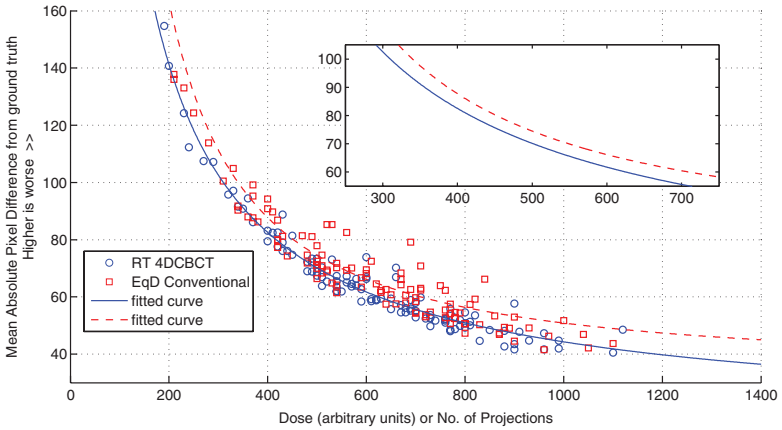

Figure 10. Image quality (*MAPD*) versus dose for RT 4D CBCT and EqD conventional for XCAT studies. The EqD conventional simulations use equivalent dose to RT 4D CBCT. Inset: fitted curves for RT 4D CBCT (solid) and EqD conventional (dashed) simulations shown without data tick marks for clarity.

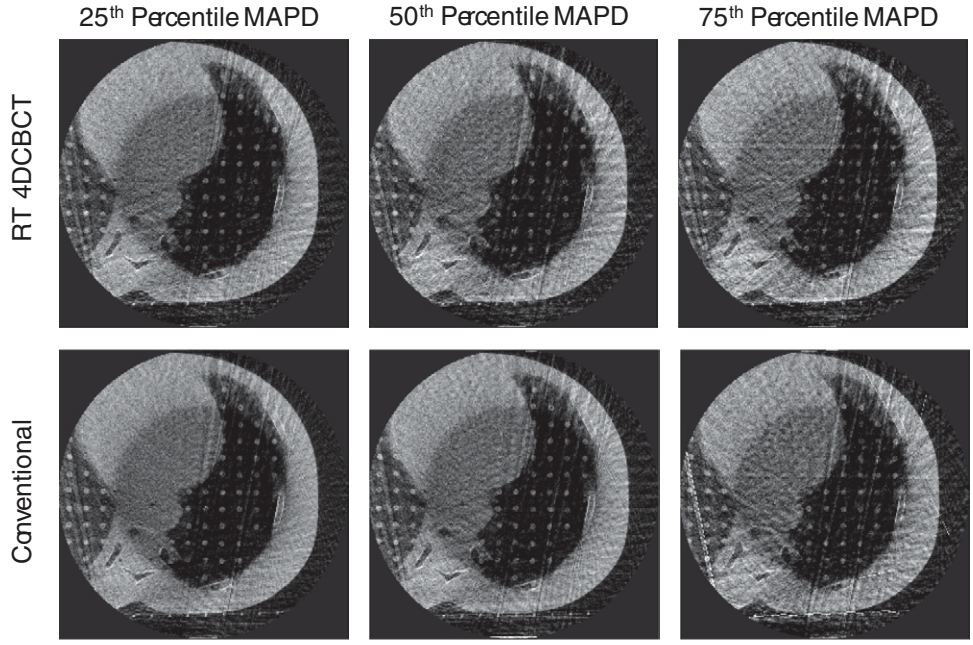

Figure 11. RT 4D CBCT (top row) and conventional (bottom row) showing images from the 25th, 50th, and 75th percentile of mean absolute pixel difference (*MAPD* from ground truth) between the reconstructed image and the ground truth.

3.4. Representative coronal reconstructions from XCAT phantom simulations

A subset of XCAT phantoms studies representing the 25th, 50th, and 75th percentile of *MAPD* from ground truth gives a visualization of the image quality and spatial resolve of the tumour. Single coronal image slices through the moving tumour from the RT 4D CBCT and conventional simulations and each of the 25th, 50th, and 75th percentile *MAPD* distributions are

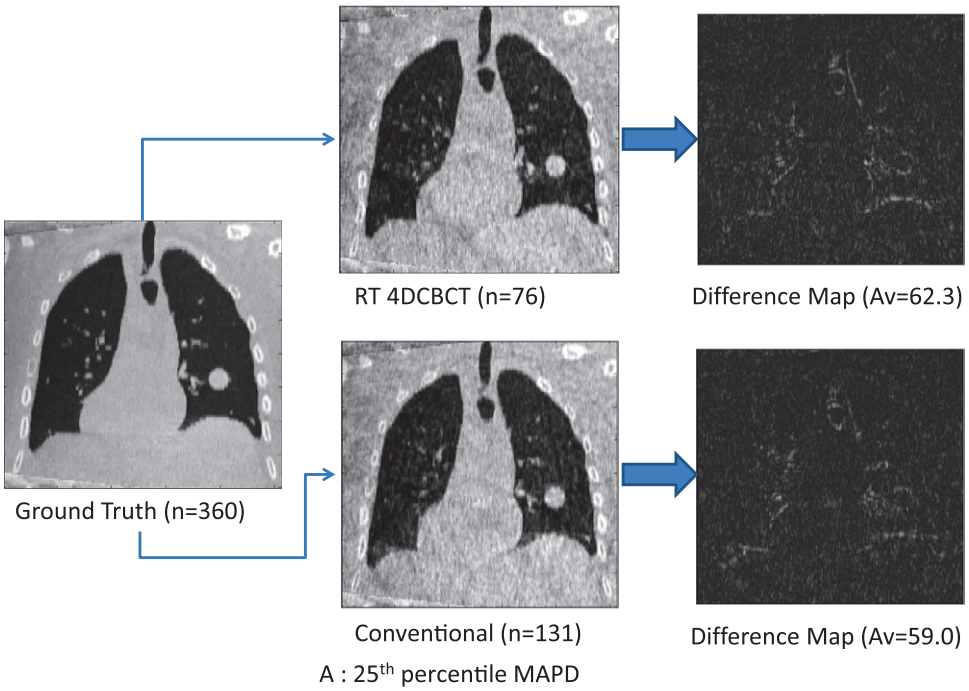

Figure 12. Coronal slices from XCAT simulation corresponding to 25th percentile of *MAPD*. Ground truth image (left), RT 4D CBCT (top) and conventional (bottom), difference maps (right). 'n' is number of projections required, 'Av' is average pixel difference from ground truth image.

shown (figures 12–14). The 'ground truth' image in the XCAT simulations is the tumour in the middle of its trajectory between inhale and exhale (described in section 2.5.1). The respiratory bin 'capturing' the tumour midway through its trajectory is shown for simulations using RT 4D CBCT and conventional acquisition methods (figures 12–14, top and bottom rows, respectively). Using equation (2) the defined *MAPD* for the displayed coronal slice is calculated for RT 4D CBCT and conventional reconstruction techniques denoted as 'Av = ...' in the figures. The number of required projections are reported for each simulation and is denoted as 'n' (figures 12–14).

The vertical line over the tumour in figure 15 represents the pixels along which the previously defined *SupInf* image gradient is calculated (see equation (3)). figures 16–18 show the resulting calculations for the *SupInf* image gradient: the thick solid black line is the gradient for the ground truth and is repeated in each plot for reference. The dashed lines represent the gradient for RT 4D CBCT and the dotted lines represent the gradient for conventional simulations.

4. Discussion

It is likely that 4D CBCT will continue to grow as a clinical tool along with an accompanying increase in imaging dose for the patient. It is imperative that any extra imaging dose burden on the patient is utilized in the most efficient way possible. We have demonstrated through simulation studies that the RT 4D CBCT method can offer a substantial saving in imaging dose

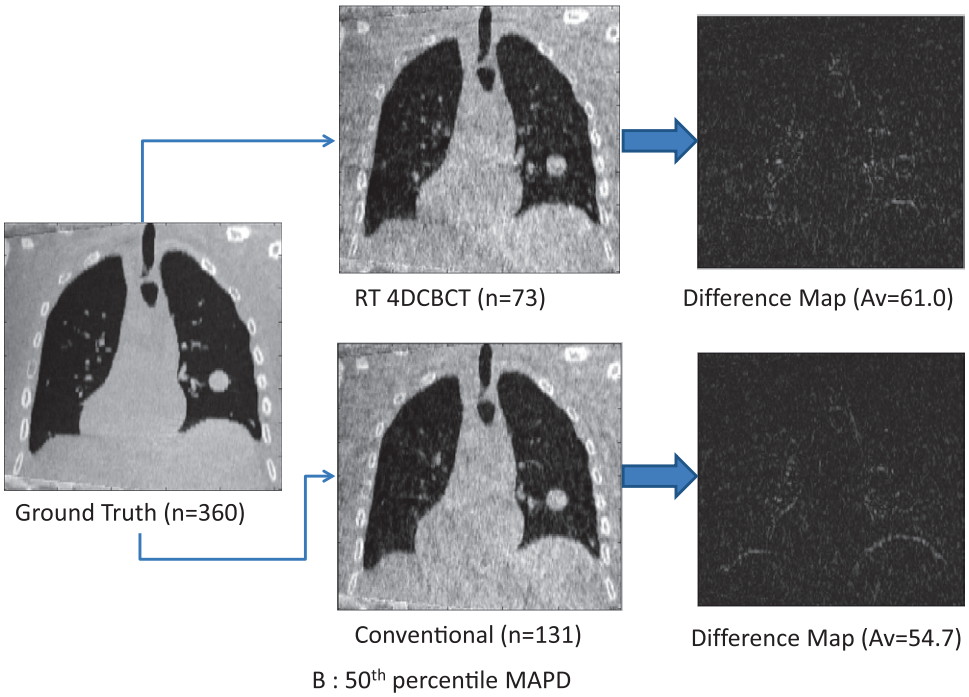

Figure 13. Coronal slices from XCAT simulation corresponding to 50th percentile of *MAPD*. Ground truth image (left), RT 4D CBCT (top) and conventional (bottom), difference maps (right). 'n' is number of projections required, 'Av' is average pixel difference from ground truth image.

compared to conventional 4D CBCT. Simulations of RT 4D CBCT and conventional acquisition techniques have been performed for 111 patient-measured breathing traces. Taking the ground truth dataset as a reference, comparisons are presented between the RT 4D CBCT and conventional acquisition methods of the following items:

(i) Adjacent projection angular spacing distributions;
(ii) Distributions of *MAPD* from reference ground truth;
(iii) Distributions of *MAPD* from reference ground truth versus imaging dose;
(iv) Representative reconstructed images for 25th, 50th, and 75th percentile of *MAPD*.

4.1. Adjacent projection angular spacing distribution

The stand out feature of the two distributions in figure 5 is that the conventional method exhibits an isolated peak in the first histogram bin ($\leqslant 0.2°$) meaning that a large number of adjacent projections are clustered within a respiratory bin and have a small angular separation. This means we have extraneous projections that cost imaging dose but do not add much 'new' anatomical information because the separation is so small. This clustering is a result of the imager triggering at a fixed frequency of roughly 5.5 Hz for the conventional simulations based on Elekta's Symmetry 4D CBCT parameters. In contrast, the RT 4D CBCT method gives rise to a distribution whose mode is somewhere between 2° and 3° owing to the RT 4D CBCT method triggering once per bin per respiratory cycle. This makes sense as the gantry speed is 0.83 deg. $s^{-1}$and multiplying this by a population average respiration period of 3.8 s (George *et al* 2005)

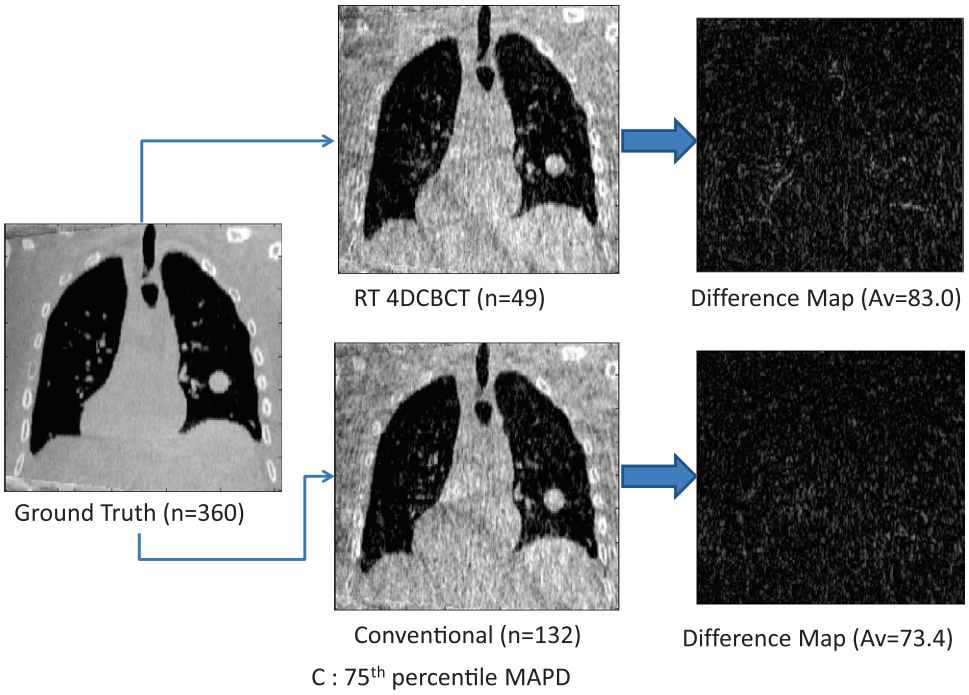

Figure 14. Coronal slices from XCAT simulation corresponding to 75th percentile of *MAPD*. Ground truth image (left), RT 4D CBCT (top) and conventional (bottom), difference maps (right). 'n' is number of projections required, 'Av' is average pixel difference from ground truth image.

gives roughly 3° degrees which is similar to the RT 4D CBCT modal angular separation of 2–3°. The other noteworthy feature is the difference in the average number of projections over the 111 breathing traces between conventional (1320) and RT 4D CBCT (617) with the RT 4D CBCT average being about 53% lower than the conventional.

4.2. Mean absolute pixel difference from reference ground truth, imaging dose and reconstruction images

Quantitatively, for the 111 breathing traces used in the Rando studies, the RT 4D CBCT method's average *MAPD* value of 119.2 raw pixel value units is worse than the conventional method's average value of 110.8 raw pixel value units (figure 6); however, qualitatively there is not much difference. Similarly for the XCAT studies the average *MAPD* values are 65.1 and 58.6 for the RT 4D CBCT and conventional methods respectively (figure 7). Representative images from the 25th, 50th and 75th percentiles of *MAPD* from figure 6 are shown in figure 11 and there is little difference between the image progression in the top row (RT 4D CBCT) and the bottom row (conventional). If we now consider the imaging dose for both RT 4D CBCT and conventional simulations there is a stark difference in behaviour. Irrespective of an individual's breathing period, the conventional method will always use about 1320 projections. Figure 8 demonstrates the fixed nature of the conventional method and a sub-optimal use of imaging dose. For the Rando studies, the interquartile range of *MAPD* is 34.55 (89.36–123.91) and for the XCAT studies, the interquartile range is 15.73 (47.83–63.56) but always for a fixed imaging dose. In contrast, for the Rando studies the RT 4D CBCT method

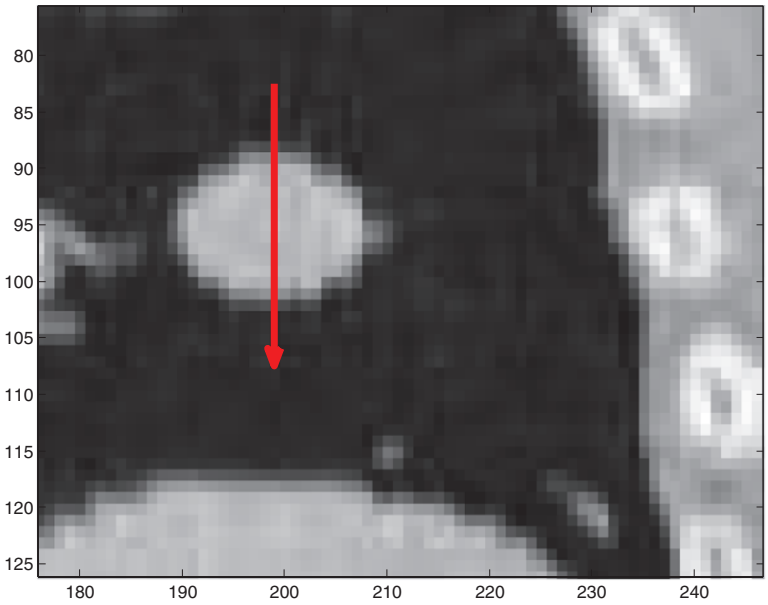

Figure 15. Arrow showing pixel gradient calculation direction (superior to inferior).

gives an interquartile range of *MAPD* of 32.36 (97.85–130.21) and a corresponding spread in dose (486.25–761.25). For the XCAT studies we have an interquartile range of *MAPD* of 19.94 (52.28–72.22) and dose spread of (492.5–770.0). The *MAPD* metric provides a single distilled figure of image difference. One of the limitations of this metric is that it does not give detailed information about the nature of the differences between two images. In this work, both image noise and streaking artifacts contribute to a higher (worse) *MAPD* value; however, the reconstructed images suggest that the streaking artifacts could be the dominant factor in determining the *MAPD*. Suppose we can choose an *MAPD* value of 100. Referring to figure 8 we see that the RT 4D CBCT method requires slightly less than 800 units of imaging dose whereas the conventional method is a flat rate of 1320, representing roughly a 40% saving in imaging dose for the same *MAPD* value. The reason this occurs is because for slower breathers in a fixed 240 s acquisition, there will be fewer breathing cycles compared to a faster breather. Using the RT 4D CBCT method, there is only one projection per bin per breathing cycle and so slower breathers will have fewer projections and thus use less dose compared to a faster breather. In its current form, the RT 4D CBCT algorithm is 'tied' to the respiratory rate of the patient and so slow breathers will always result in fewer projections (and worse images) for a given fixed acquisition time (240 s), in these studies . It is remarkable that the RT 4D CBCT yields a comparable image quality metric (*MAPD*) to conventional 4D CBCT for the very slow breathing outliers (open circles between about 200 and 300 projections in figure 8). This is a 'worst case' for conventional 4D CBCT as it will still use 1320 projections for slow breathers but results in images of similar quality to RT 4D CBCT using 200 to 300 projections. To overcome this problem for slow breathers, an extension to the RT 4D CBCT algorithm could incorporate two projections per phase bin per breath: one at the beginning and one at the end of a phase bin. The goal of such an approach would be to strive for as wide an angular separation as possible within a given phase bin. This would certainly increase projections, but we would see the return to a more 'bunched' pattern of projection acquisitions, although not as bad as conventional 4D CBCT bunching (figure 1). The implication is that if

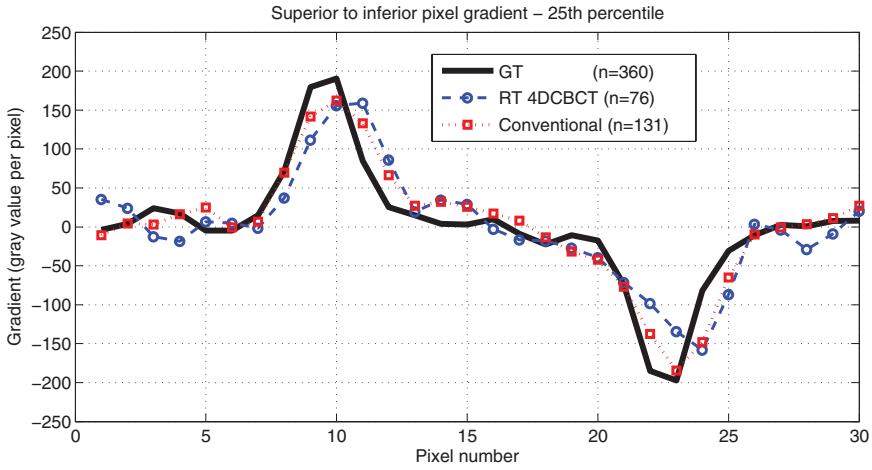

Figure 16. Image gradient calculated in superior to inferior direction for 25th percentile of MAPD simulation. 'n' is the number of projections.

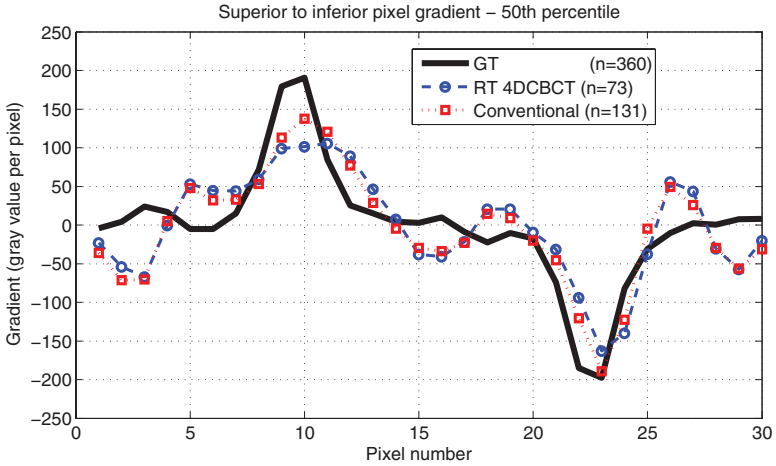

Figure 17. Image gradient calculated in superior to inferior direction for 50th percentile of MAPD simulation. 'n' is the number of projections.

one would like to control the image quality using RT 4D CBCT, then both the gantry velocity and the imaging frequency should be 'tuned' to the respiration rate of the patient, a similar finding to other investigators (Lu *et al* 2007, Ahmad and Pan 2012, Fast *et al* 2013, O'Brien *et al* 2013, 2014).

4.3. Tumour motion in XCAT studies

The XCAT studies have shown that the RT 4D CBCT method can produce reconstructed images of a moving target that are of comparable quality to conventional 4D CBCT but with fewer projections. Figures 12–14 illustrate no remarkable qualitative or quantitative difference comparing the RT 4D CBCT and conventional 4D CBCT reconstructed images. There are some discernible patterns of brightness in the difference maps about the liver / lung boundary

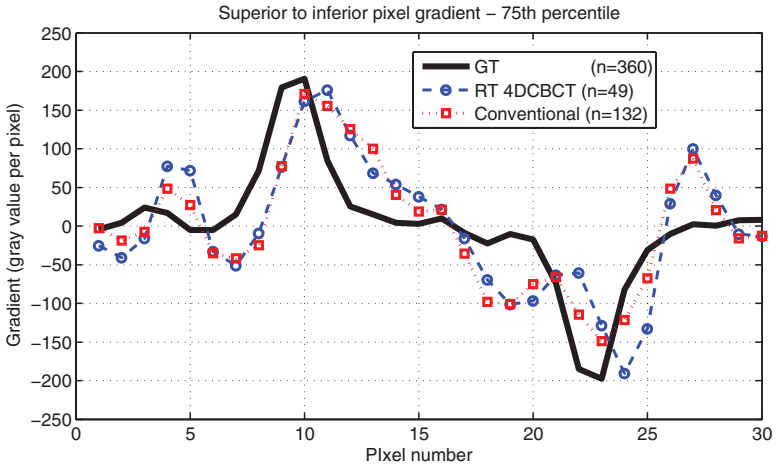

Figure 18. Image gradient calculated in superior to inferior direction for 75th percentile of MAPD simulation. 'n' is the number of projections.

and the tumour boundaries. The overall noise and graininess is worst for the 75th percentile (figure 14). The crucial feature to note is that conventional 4D CBCT reconstruction effectively 'wastes' projections (and thus dose) because of the 'bunched' projection pattern that forms (see figure 1(B)). Mauer *et al* have described a step-and-shoot approach whereby fixed stationary gantry positions are chosen and a set of projections are acquired over at least one respiratory period, potentially removing the bunched projection problem; however, this does increase the acquisition time by a few minutes (Maurer *et al* 2010). Similarly to the Rando phantom experiments, the number of projections for a given phase bin (n) used for the RT 4D CBCT simulations is directly proportional to the rate of respiration in the patient ($n = 49$–76), unlike conventional 4D CBCT which uses roughly the same number of projections regardless of the patient's respiration rate ($n = 131$–132) (figures 12–14). Referring to figures 16–18, the ground truth image gradient plot (solid line) compared to both the RT 4D CBCT and conventional plots follow the same general shape; however the maxima and minima are quite variable and the'0' gradient regions become noisier going from figures 12–14 for both RT 4D CBCT and conventional simulations. The gradient data is taken to represent tumour detectability by eye. The plots in figures 16–18 suggest that there is little difference between the RT 4D CBCT and conventional lesion detectability although there is evidence of a minor positional shift in both the RT 4D CBCT and conventional plots. The maxima and minima appear to be shifted by roughly 1 pixel (1.2 mm is the CBCT slice thickness in the z-direction) in the superior-inferior direction suggesting a lag between the where the tumour actually is (according to the ground truth gradient plot) and the detected tumour location (RT 4D CBCT and conventional plots). The positional error in tumour location detection in these studies implies a targeting accuracy no better than 1.2 mm. There is a substantially higher cost in dose to achieve this level of accuracy (number of projections 'n') for conventional 4D CBCT compared to RT 4D CBCT.

5. Conclusion

The simulation studies have demonstrated that the RT 4D CBCT method can potentially offer a substantial saving of imaging dose in the order of about 53% on average compared to

conventional 4D CBCT using a wide range of patient breathing traces with a minimal impact on image quality.

References

Abdelnour A *et al* 2007 Phase and amplitude binning for 4D-CT imaging *Phys. Med. Biol.* **52** 3515

Ahmad M and Pan T 2012 Target-specific optimization of four-dimensional cone beam computed tomography *Med. Phys.* **39** 5683–96

Brehm M, Berkus T, Oehlhafen M, Kunz P and Kachelriess M 2011 Motion-compensated 4D cone-beam computed tomography *Nuclear Science Symp. and Medical Imaging Conf.* pp 3986–93

Brehm M, Paysan P, Oelhafen M and Kachelrieß M 2013 Artifact-resistant motion estimation with a patient-specific artifact model for motion-compensated cone-beam CT *Med. Phys.* **40** 101913

Cooper B J, O'Brien R T, Balik S, Hugo G D and Keall P J 2013 Respiratory triggered 4D cone-beam computed tomography: a novel method to reduce imaging dose *Med. Phys.* **40** 41901

Fast M F, Wisotzky E, Oelfke U and Nill S 2013 Actively triggered 4d cone-beam CT acquisition *Med. Phys.* **40** 91909

Feldkamp L A, Davis L C and Kress J W 1984 Practical cone-beam algorithm *J. Opt. Soc. Am.* A **1** 612–9

George R, Chung T D, Vedam S S, Ramakrishnan V, Mohan R, Weiss E and Keall P J 2006 Audio-visual biofeedback for respiratory-gated radiotherapy: impact of audio instruction and audio-visual biofeedback on respiratory-gated radiotherapy *Int. J. Radiat. Oncol. Biol. Phys.* **65** 924–33

George R, Vedam S S, Chung T D, Ramakrishnan V and Keall P J 2005 The application of the sinusoidal model to lung cancer patient respiratory motion *Med. Phys.* **32** 2850

Giaddui T, Cui Y, Galvin J, Yu Y and Xiao Y 2013 Comparative dose evaluations between XVI and OBI cone beam CT systems using Gafchromic XRQA2 film and nanoDot optical stimulated luminescence dosimeters *Med. Phys.* **40** 62102

Ionascu D, Jiang S B, Nishioka S, Shirato H and Berbeco R I 2007 Internal-external correlation investigations of respiratory induced motion of lung tumors *Med. Phys.* **34** 3893–903

Jia X, Dong B, Lou Y and Jiang S B 2011 GPU-based iterative cone-beam CT reconstruction using tight frame regularization *Phys. Med. Biol.* **56** 3787–807

Jia X, Lou Y, Li R, Song W Y and Jiang S B 2010 GPU-based fast cone beam CT reconstruction from undersampled and noisy projection data via total variation *Med. Phys.* **37** 1757–60

Keall P J *et al* 2006 The management of respiratory motion in radiation oncology report of AAPM Task Group 76a *Med. Phys.* **33** 3874–900

Kim S, Yoo S, Yin F F, Samei E and Yoshizumi T 2010 Kilovoltage cone-beam CT: comparative dose and image quality evaluations in partial and full-angle scan protocols *Med. Phys.* **37** 3648

Kincaid R E Jr, Yorke E D, Goodman K A, Rimner A, Wu A J and Mageras G S 2013 Investigation of gated cone-beam CT to reduce respiratory motion blurring *Med. Phys.* **40** 41717

Leng S, Tang J, Zambelli J, Nett B, Tolakanahalli R and Chen G H 2008a High temporal resolution and streak-free four-dimensional cone-beam computed tomography *Phys. Med. Biol.* **53** 5653

Leng S, Zambelli J, Tolakanahalli R, Nett B, Munro P, Star-Lack J, Paliwal B and Chen G H 2008b Streaking artifacts reduction in four-dimensional cone-beam computed tomography *Med. Phys.* **35** 4649–59

Li T and Xing L 2007 Optimizing 4D cone-beam CT acquisition protocol for external beam radiotherapy *Int. J. Radiat. Oncol. Biol. Phys.* **67** 1211–9

Lu J, Guerrero T M, Munro P, Jeung A, Chi P C M, Balter P, Zhu X R, Mohan R and Pan T 2007 Four-dimensional cone beam CT with adaptive gantry rotation and adaptive data sampling *Med. Phys.* **34** 3520

Maurer J, Pan T and Yin F F 2010 Slow gantry rotation acquisition technique for on-board four-dimensional digital tomosynthesis *Med. Phys.* **37** 921–33

O'Brien R T, Cooper B J and Keall P J 2013 Optimizing 4D cone beam computed tomography acquisition by varying the gantry velocity and projection time interval *Phys. Med. Biol.* **58** 1705

O'Brien R T, Cooper B J, Kipritidis J, Shieh C C and Keall P J 2014 Respiratory motion guided four dimensional cone beam computed tomography: encompassing irregular breathing *Phys. Med. Biol.* **59** 579

Qi Z and Chen G H 2011 Extraction of tumor motion trajectories using PICCS-4DCBCT: a validation study *Med. Phys.* **38** 5530

Rit S, Sarrut D and Desbat L 2009 Comparison of analytic and algebraic methods for motion-compensated cone-beam CT reconstruction of the thorax *IEEE Trans. Med. Imaging* **28** 1513–25

Rit S, Oliva M V, Brousmiche S, Labarbe R, Sarrut D and Sharp G C 2014 The reconstruction toolkit (RTK), an open-source cone-beam CT reconstruction toolkit based on the insight toolkit (ITK) *J. Phys.: Conf. Ser.* **489** 2079

Rosu M and Hugo G D 2012 Advances in 4D radiation therapy for managing respiration: part II–4D treatment planning *Z. Med. Phys*. **22** 272–80

Ruan D, Fessler J A, Balter J and Keall P 2009 Real-time profiling of respiratory motion: baseline drift, frequency variation and fundamental pattern change *Phys. Med. Biol.* **54** 4777

Santoro J P, Yorke E, Goodman K A and Mageras G S 2009 From phase-based to displacement-based gating: a software tool to facilitate respiration-gated radiation treatment *J. Appl. Clin. Med. Phys.* **10** 2982

Segars W P, Sturgeon G, Mendonca S, Grimes J and Tsui B M W 2010 4D XCAT phantom for multimodality imaging research *Med. Phys.* **37** 4902–15

Shrimpton P, Wall B and Fisher E 1981 The tissue-equivalence of the Alderson Rando anthropomorphic phantom for x-rays of diagnostic qualities *Phys. Med. Biol.* **26** 133

Sonke J J, Lebesque J and van Herk M 2008 Variability of four-dimensional computed tomography patient models *Int. J. Radiat. Oncol. Biol. Phys.* **70** 590–8

Sweeney R, Seubert B, Stark S, Homann V, Muller G, Flentje M and Guckenberger M 2012 Accuracy and inter-observer variability of 3D versus 4D cone-beam CT based image-guidance in SBRT for lung tumors *Radiat. Oncol.* **7** 81

Takahashi W, Yamashita H, Kida S, Masutani Y, Sakumi A, Ohtomo K, Nakagawa K and Haga A 2013 Verification of planning target volume settings in volumetric modulated arc therapy for stereotactic body radiation therapy by using in-treatment 4-dimensional cone beam computed tomography *Int. J. Radiat. Oncol. Biol. Phys*. **86** 426–31

Wang J and Gu X 2013 High-quality four-dimensional cone-beam CT by deforming prior images *Phys. Med. Biol.* **58** 231

Zhang Y, Yin F F, Segars W P and Ren L 2013 A technique for estimating 4D-CBCT using prior knowledge and limited-angle projections *Med. Phys.* **40** 121701

6

REAL-TIME RESPIRATORY TRIGGERED FOUR DIMENSIONAL CONE-BEAM CT HALVES IMAGING DOSE COMPARED TO CONVENTIONAL 4D CBCT

The work up until this point in the project had not attempted to study the RT 4D CBCT imaging technique with a *physically* moving tumour target analogue in a dynamic phantom. In this chapter, the experimental platform that implements RT 4D CBCT using a moving target in a dynamic phantom, and that could possibly be used with a patient, is presented. This work makes the critical step of moving on from theoretical and *in silico* simulation work to a real-time, working system that performs RT 4D CBCT. This work is currently (7 December 2018) under review for publication in *Physics in Medicine and Biology*.

Real-time respiratory triggered four dimensional cone-beam CT halves imaging dose compared to conventional 4D CBCT

Benjamin J Cooper[1,2], Ricky T O'Brien[1], Chun-Chien Shieh[1] and Paul J Keall[1]

[1] ACRF Image X Institute, Biomedical Building (C81), 1 Central Ave, Australian Technology Park, Eveleigh, NSW 2015, Australia

[2] Department of Medical Physics and Radiation Engineering, The Canberra Hospital, Canberra, ACT 2605, Australia

E-mail: ben.cooper@act.gov.au

Abstract. Four dimensional cone-beam computed tomography (4D CBCT) improves patient positioning and the accuracy of radiation therapy for patients with mobile tumours. Generally, 4D CBCT requires many hundreds of x-ray projections to measure target trajectories and the imaging frequency is not adapted to the patient's respiratory signal resulting in over-sampling. In contrast, respiratory triggered 4D CBCT (RT 4D CBCT) is an acquisition technique that has been experimentally implemented and has shown to reduce the number of x-ray projections and thus 4D CBCT dose with minimal impact on image quality. The aim of this work is to experimentally investigate RT 4D CBCT *in situ* and measure target trajectory mean position, image quality and imaging dose from this approach. A commercially available phantom with programmable target motion was programmed with nine target trajectories derived from patient-measured respiratory traces known to span the range of image quality when used for 4D CBCT reconstruction. 4D CBCT datasets were acquired for each target trajectory using the RT 4D CBCT acquisition technique and the conventional 4D CBCT acquisition technique. From the reconstructed 4D CBCT datasets, target trajectory mean positions, imaging dose and image quality metrics were calculated and compared between the two techniques. Target trajectory and mean position were measured by tracking the target's displacement in the phantom; imaging dose was measured by counting the total number of x-ray projections acquired; and image quality was assessed by calculating the contrast-to-noise ratio (CNR), signal-to-noise ration (SNR) and edge response width (ERW). For each of the nine cases, the target trajectory mean position as determined by RT 4D CBCT and conventional 4D CBCT varied from the reference source trajectory mean position by 0.7 mm or less except for one case where a conventional 4D CBCT mean position varied by 1.3 mm. On the average of these nine studies, RT 4D CBCT required half as many projections as conventional 4D CBCT giving a 50% reduction in imaging dose. Overall, the image quality metrics (CNR and SNR) were marginally worse for RT 4D CBCT; ERW metric showed no statistically significant difference between the RT 4D CBCT and conventional 4D CBCT reconstructed datasets. Respiratory triggered 4D CBCT couples the real-time respiratory signal to the 4D CBCT image acquisition system and requires less imaging dose than conventional 4D CBCT to determine target trajectory mean positions.

1. Introduction

Modern linac based radiation therapy has the ability to acquire images of the patient prior to treatment to verify patient and target position accuracy. These systems are commonly shipped with kilo-voltage (kV) x-ray imaging systems as standard which can be used for acquiring orthogonal 2D planar x-ray images or for acquiring 3D cone-beam computed tomographic image datasets.

Four dimensional cone-beam computed tomography (4D CBCT) acquisition techniques began to emerge around 2005 (Sonke et al.; 2005; Dietrich et al.; 2006; Li et al.; 2006) and became commercially available in 2010†. 4D CBCT enables the ability to assess and verify that the range and mean position of target motion, due to respiration, is contained within the planned treatment volume (PTV) during treatment delivery. This provides the treating staff with visual feedback that the target is correctly aligned to the radiation treatment beam. Having confidence in the alignment of the patient and treatment beam is paramount, especially in lung stereotactic body radiation therapy (SBRT) where ablative doses are delivered to the target. SBRT is described in the literature as having the highest need for respiratory motion management (Benedict et al.; 2010).

The use of *in situ* patient imaging continues to grow (Simpson et al.; 2009). On the one hand, the increased use of *in situ* patient imaging can lead to better guidance and targeting of the radiation treatment beam (Hendee and O'Connor; 2012). On the other hand, a consequence of increased imaging potentially results in a higher imaging dose burden to the patient. A conventional 4D CBCT typically requires more projections than a static CBCT because the acquired projections need to be subdivided into respiratory phase bins and reconstructed separately for each bin. More projections may increase the imaging dose to the patient. Furthermore, 4D CBCT necessitates a slower acquisition so that there is sufficient data for CBCT reconstruction. In a conventional 4D CBCT acquisition there is no real-time adaptation of the projection acquisition frame rate to the patient's respiratory rate, it is set to a fixed frame rate. This can lead to projection clustering where the extra projections in the cluster are too similar to one another giving rise to data over-sampling. The extra projections in the cluster are redundant and unnecessarily increase imaging dose.

To avoid excess imaging dose, Fast et al. (2013) have developed a system called "Actively triggered 4D cone-beam CT" that actively triggers projections based on either an electro-magnetic or external motion sensor supplying the respiratory signal. Feasibility of their method was demonstrated with sinusoidal trajectories only. Respiratory triggered 4D CBCT (RT 4D CBCT) is an experimental technique that has been developed from previous *in silico* work whereby the real-time respiratory signal is processed and interfaced with the kV imaging x-ray source to trigger when the CBCT x-ray projections are acquired during the 4D CBCT acquisition process (Cooper

† https://www.elekta.com/meta/press-intern.html?id=378cfff6-b75e-4396-bf5b-a2660accab13 - web page retrieved June 2018

et al.; 2015; O'Brien et al.; 2016). The key benefit of this technique is a considerable reduction in imaging dose to the patient with minimal impact on image quality(O'Brien et al.; 2014; Cooper et al.; 2015). The RT 4D CBCT technique effectively removes the redundant projections in a projection cluster by adapting the projection acquisition frame rate according to the respiratory signal. Previous work on this technique has described: the theoretical concept (Cooper et al.; 2013); *in silico* modelling with XCAT phantom (Cooper et al.; 2015), and implementation on an Elekta‡ linear accelerator for sinusoidal respiratory traces (O'Brien et al.; 2016).

This study is the first description of how to implement RT 4D CBCT for non sinusoidal respiratory signals on a Varian§ linear accelerator. For the first time, nine patient-measured respiratory traces will be used to perform clinically realistic phantom based experiments to investigate clinically relevant target trajectory and mean positions, imaging dose and image quality for both RT 4D CBCT and conventional 4D CBCT.

2. Methods

2.1. Respiratory triggered 4D CBCT

A detailed description of the respiratory triggered 4D CBCT algorithm is available (Cooper et al.; 2013, 2015); a high level description is included here for completeness. The main feature of RT 4D CBCT is the coupling of real-time respiratory signal data to adapt the projection acquisition frequency in the linac kV x-ray imaging system during CBCT acquisition. In RT 4D CBCT, the x-ray projections are triggered so that only one projection per respiratory phase bin is acquired, based on the real-time respiratory signal. This differs from a conventional 4D CBCT acquisition where the x-ray projection triggering rate is constant and uncoupled to the patient respiratory phase. It has been shown that RT 4D CBCT reduces x-ray imaging dose with minimal impact on image quality compared to conventional (O'Brien et al.; 2014; Cooper et al.; 2015).

2.2. Overview of experimental work

An overview of the experimental workflow carried out in this work is presented (figure 1) with details in the following sections. Patient respiratory traces were used to move the target inside the CIRS dynamic thorax phantom with an external infra-red marker block moving as a surrogate. An RPM‖ monitoring system was used to record the infra-red marker block motion and produce a real-time data stream for implementation of the RT 4D CBCT algorithm (Cooper et al.; 2013, 2015) and for post-acquisition sorting of projections into phase bins for both RT 4D CBCT and conventional 4D CBCT. The target trajectory mean position is clinically important as it represents the position to which treatment beams should be aligned. Target trajectory mean position was

‡ Elekta, Box 7593, SE-103 93 Stockholm, Sweden
§ Varian Medical Systems, Inc. 3100 Hansen Way, Palo Alto, CA 94304-1038, USA
‖ Real-time position management, Varian Medical Systems

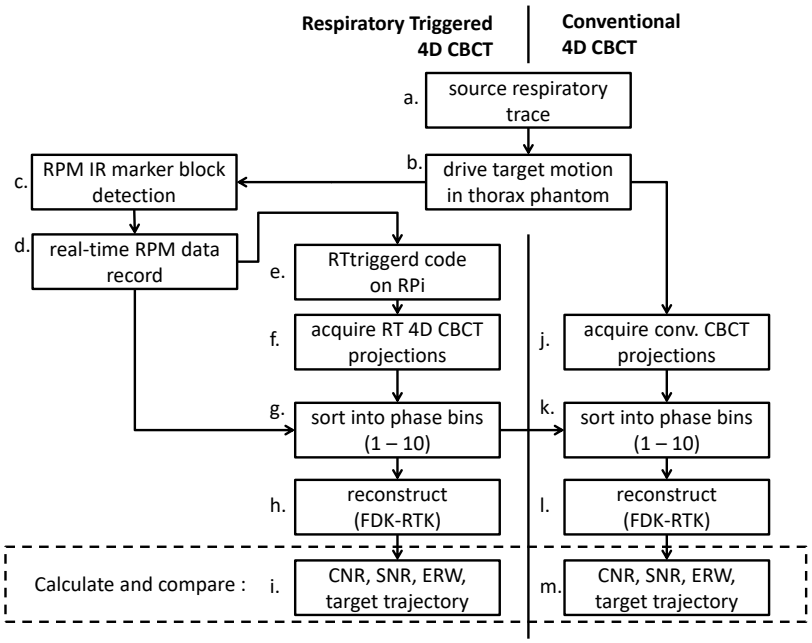

Figure 1. Workflow of experimental work. Boxes e–i represent RT 4D CBCT and j–m represent conventional 4D CBCT. The arrow d–g–k represents the use of the RPM data record for sorting projections into phase bins for both RT 4D CBCT and conventional 4D CBCT. See text for further details.

measured for the two techniques; this will be referred to as the "clinical task" in this article. The contrast-to-noise ratio andsignal-to-noise ratio (CNR and SNR) indicate how well the target is visualised against a potentially noisy background. The edge response width (ERW) indicates the image sharpness of the edge of the target where a sharper edge has a lower value for ERW. Following the same method as O'Brien et al. (2016), the CNR, SNR and ERW were calculated for both RT 4D CBCT and 4D CBCT and compared.

2.3. Source respiratory traces (figure 1a)

A previous study ranked 111 patient-measured respiratory traces according to the image quality of their respective *in silico* 4D CBCT reconstructions. The image quality metric used to rank them was the mean absolute pixel difference ($MAPD$) of the reconstructed image compared to a ground truth image (Cooper et al.; 2015). The respiratory traces were grouped into nine percentiles: <5, 5-10, 10-20, 20-40, 40-60, 60-80, 80-90, 90-95, >95 representing the variation in image quality from the various breathing patterns across the 111 patient-measured respiratory traces. The convention herein is that a lower rank percentile represents a respiratory trace that resulted in *better* image quality (i.e. lower $MAPD$ represents a lower difference from ground truth) while a higher rank percentile represents a respiratory trace that gave a *worse* image quality (higher $MAPD$). The best (<5) and worst (>95) traces were selected and the other 7 traces

were selected randomly from the other seven percentiles (5-10, 10-20, 20-40, 40-60, 60-80, 80-90, 90-95) from the cohort of 111 respiratory traces and used for the RT 4D CBCT and conventional 4D CBCT experiments in this work. The nine respiratory traces were used to drive the target motion in the commercially available CIRS dynamic thorax phantom (model 008A)¶. Each trace was normalised such that the maximal range of the target trajectory was fixed to 2 cm. This was necessary to ensure the target motion did not exceed the CIRS phantom's target motion driving capability.

2.4. Driving target motion in thorax phantom (figure 1b)

The CIRS dynamic thorax phantom has the ability to "playback" previously recorded respiratory signals from systems such as the Varian RPM$^+$ monitoring system. A 1 cm diameter spherical target of water analogue material surrounded by lung analogue material is driven back and forth in a superior-inferior direction via a stepper-motor system interfaced to the CIRS computer application which has the source respiratory trace loaded. The phantom serves as a tool for studying tumour target motion and its interplay effects during 4D CBCT imaging acquisition. Each of the nine respiratory traces were used as separate sources of motion for each of the RT 4D CBCT and conventional 4D CBCT experimental image set acquisitions.

2.5. RPM IR marker block detection (figure 1c)

The Varian RPM system (version 1.4) was used as a motion monitoring system. A two-dot infra-red reflector marker block was mounted on the external marker block platform on the CIRS phantom. The IR-marker block was set up to move completely in-phase with the internal target motion and thus becomes the surrogate for target motion in this experiment as mentioned in section 2.2. The RPM system was set up to enable RS-232 serial communications. The serial output data stream contained the real-time marker block position data including displacement, phase, and time elapsed. This data was fed into RT 4D CBCT program as input to decide when to trigger the x-ray projections; the data stream is also recorded for subsequent sorting of projections into respective phase bins.

2.6. RPM data record (figure 1d)

A Raspberry Pi 2 (model B v1.1)* was employed to serve a number of functions: (1) receiving and recording the RS-232 serial data stream from the RPM system giving the marker displacement, phase and time; (2) controlled suppression of x-ray trigger pulses from the on-board imaging (OBI) "Supervisor" computer to the kilo-voltage (kV)

¶ CIRS Tissue Simulation & Phantom Technology, 900 Asbury Ave, Norfolk, VA 23513, USA
$^+$ Varian Medical Systems, Inc. 3100 Hansen Way, Palo Alto, CA 94304-1038, USA
* Raspberry Pi Foundation, UK Registered Charity 1129409, UK

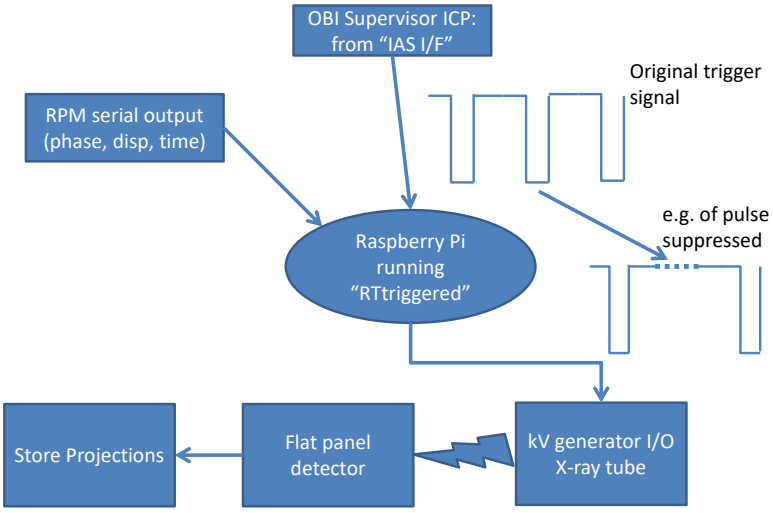

Figure 2. Schematic showing the interfaces with the Raspberry Pi

generator system via its General Programmable Input/Output interface and a custom designed circuit.

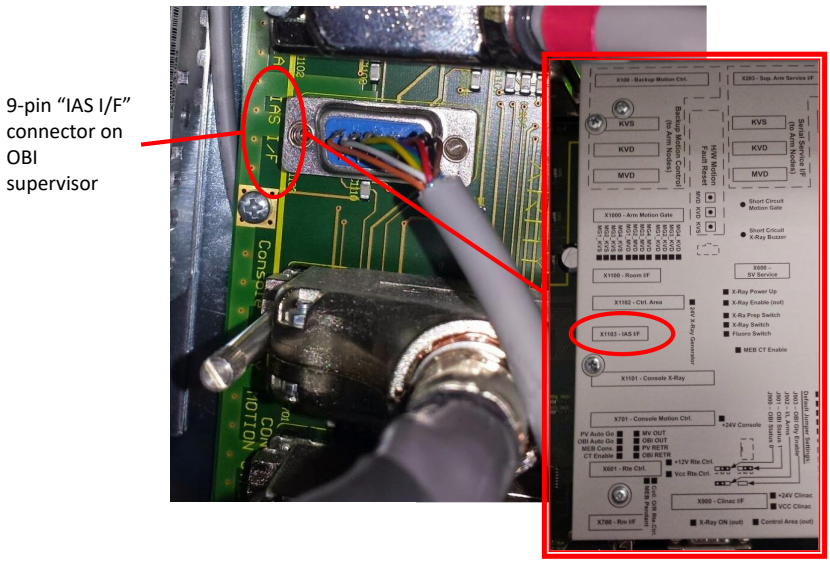

Figure 3. Interfacing with the OBI Supervisor. The IAS I/F cable running to the kV generator is re-routed to the Raspberry Pi micro computer hosting the "RTtriggered" program which implements the RT 4D CBCT algorithm and sends on the trigger signals to the kV generator.

2.7. "RTtriggered" code on Raspberry Pi and interface with OBI system (figure 1e, figs. 2 and 3)

The Raspberry Pi mini computer hosted the "RTtriggered" program which implements the RT 4D CBCT technique by interfacing with the OBI as follows. Inside the OBI Supervisor circuits there is a 9-pin plug labelled "IAS I/F", the Image Acquisition System Interface (figure 3). The *IAS I/F* cable carries the x-ray triggering signal to the kV generator circuitry responsible for developing the pulses for x-ray output. During conventional CBCT image acquisition, the triggering signal is a periodic normally high (24 V) signal that drops to a nominal 0 V potential for approximately 4 mS during an x-ray trigger pulse event. Thus for a 5 Hz fluoroscope the signal is high for approximately 196 mS, then low for 4 mS (imaging trigger event) completing one cycle. It was this signal which the Raspberry Pi computer is programmed to manipulate x-ray triggers via suppressing the signal drop to 0 V to prevent a trigger event (figure 2).

2.8. Acquiring RT 4D CBCT and conventional 4D CBCT projections (figure 1f,j)

Acquiring the projections for the CBCT experiments required a constant gantry rotational velocity and the use of fluoroscopic imaging available in the OBI service mode rather than clinical mode. Inspired by the image acquisition technique developed by Kincaid et al. (2013), a customised imaging protocol for the experiments was developed with the following parameters : x-ray voltage: 110 kV; x-ray current: 20 mA; x-ray exposure time: 20 mS; trigger frequency: 5 Hz; filter: half bow-tie; flat panel offset: 14.6 cm lateral offset.

A gantry rotational velocity of $1.3\dot{3}$ $deg.s^{-1}$ was achieved by setting a dummy treatment arc to deliver 400 MU at 100 MU/minute yielding a full 360° arc in four minutes. The treatment arc field had all MLC leaves and jaws closed down so that there was no physical opening thus minimising unwanted MV x-rays. Based on a report from Kincaid et al. (2013), the estimated MV x-ray leakage at isocentre is 1 cGy. No special treatment for MV scatter onto the kV imaging panel was applied. The dummy treatment plan was attached to a dummy test patient registered in the oncology information system, Aria and was delivered in "QA mode". The custom fluoro imaging protocol together with the 360° arc gantry motion gave the necessary set up for the experimental CBCT projection acquisitions.

2.8.1. Running the RT 4D CBCT experiments Each of the nine respiratory traces (cf. 2.3) were the sources of motion for the nine pairs of RT 4D CBCT and conventional 4D CBCT dataset acquisitions. Each trace was loaded one at a time into the computer that drives the target in the CIRS dynamic thorax phantom. The sequence of steps shown below were followed to run the experimental CBCT acquisitions:

Step 1. Start the RPM acquisition

Step 2. Start fluoro running at 5 frames per second

Step 3. Initiate target motion in the CIRS dynamic thorax phantom

Step 4. Start the Raspberry Pi "RTtriggered" program (RT 4D CBCT experiments only)

Step 5. Start the gantry arc "treatment"

Step 6. Acquisition of RT 4D CBCT or conventional 4D CBCT projection data

Step 7. Gantry stop; stop fluoro; stop motion; stop "RTtriggered"

2.9. Sort projections into phase bins (figure 1g,k)

The time stamps of each projection were used to correlate the data frames received from the RPM data stream recorded in a text file in the Raspberry Pi computer. This was achieved through visualising the projections in a scrollable image stack and determining which projections showed the peaks in target trajectory. For example, suppose that projection 12 showed the first peak of the target trajectory; the corresponding projection 12 time stamp and the time stamp of the RPM data frame showing the same peak displacement are taken to signify "time zero" for both the RPM data stream and the acquired projections thus correlating the RPM data stream and the projections acquired.

2.10. Image Reconstruction (figure 1h,l)

The projections were divided into 10 phase bins based on the recorded phase information from the RPM data stream. The projections contained within each phase bin folder were fed as input to the Reconstruction Toolkit (RTK) code package (Rit et al.; 2014) using its implementation of the Feldkamp-Davis-Kress (FDK) cone-beam reconstruction algorithm. The 3D reconstruction volume dimension was set to 256x256x256 with a 1 mm^3 voxel size giving 10 reconstructed CBCT datasets, one for each of the 10 phase bins in each acquisition. The number of projections acquired in both RT 4D CBCT and conventional 4D CBCT was counted acting as a surrogate for imaging dose.

2.11. Image Analysis (figure 1i,m)

Each of the nine respiratory traces gave nine RT 4D CBCT datasets and nine conventional 4D CBCT datasets with each dataset containing 10 phase bins. Image analysis comparing the CNR, SNR, ERW, and target trajectories from both the RT 4D CBCT and conventional 4D CBCT datasets was carried out.

2.11.1. Preparation of images for calculating image metrics The coronal plane containing the target from the CIRS phantom was selected from the reconstructed CBCT dataset. Exploiting the fact that the CIRS phantom has a spherical target, the Matlab♯ function *imfindcircles* was used to identify the target's centre (x and y co-ordinates) for each phase bin. The number of projections required for : (1) an optimal

♯ MathWorks, 1 Apple Hill Drive, Natick, MA 01760-2098; version 8.0.0.783

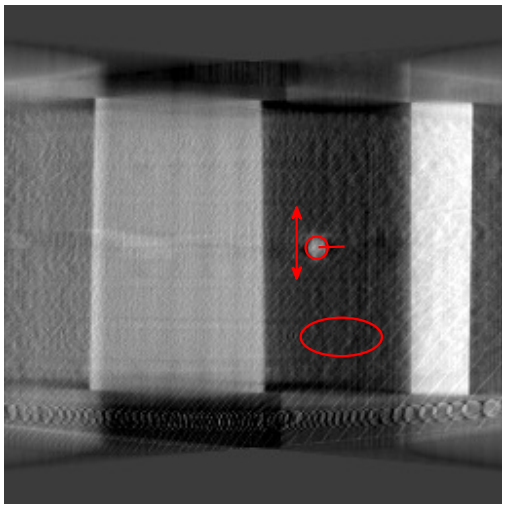

Figure 4. Representative ROIs for target (small circle) and lung background tissue (ellipse) in calculation of CNR and SNR. The horizontal line starting in the centre of the target indicates the L-R laterally directed path of the line profile for calculating ERW. Double headed arrow indicates the superior-inferior motion of the target.

RT 4D CBCT projection schedule; (2) the RT 4D CBCT and (3) conventional 4D CBCT experiments are reported as relative imaging dose metrics. Figure 4 indicates the regions of interest used to calculate the CNR and SNR and the L–R line profile to calculate the ERW. The arrows indicate the superior-inferior target trajectory motion.

2.11.2. Target trajectories The target trajectories from both the respiratory triggered and conventional 4D CBCT image sets were extracted and compared. The y co-ordinates from each of the target circles' centres (found using *imfindcircles* for each of the ten phase bins) are plotted yielding the CBCT measured target trajectory in the superior-inferior direction.

2.11.3. Contrast-to-Noise Ratio, Signal-to-Noise and Edge Response Width The contrast-to-noise ratio (CNR) and signal-to-noise ratio (SNR) are defined as follows:

$$CNR = \frac{|\overline{ROI}_{targ} - \overline{ROI}_{bg}|}{\sigma_{ROIbg}} \tag{1}$$

$$SNR = \frac{|\overline{ROI}_{targ}|}{\sigma_{ROIbg}} \tag{2}$$

where $\overline{ROI}_{targ}$ is the average pixel intensity value inside the target; $\overline{ROI}_{bg}$ is the average pixel intensity value inside a patch of "background" lung; and the σ_{ROIbg} is the variance (noise) values (cf. figure 4). Higher values for CNR and SNR represent better target contrast- and signal-to-noise.

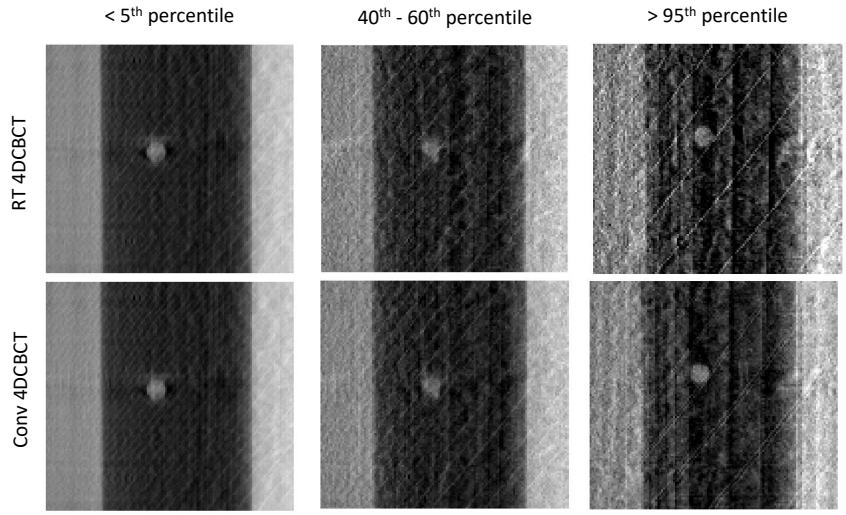

Figure 5. Coronal reconstructions through the centre of the spherical target, mid respiratory cycle (bin 6). Top row is RT 4D CBCT, bottom row is conventional 4D CBCT. Coronal reconstructions from the best, middle, and worst respiratory traces (<5th, 40th - 60th, and >95th percentiles) are shown left to right. The Window / Level in uncalibrated attenuation units is [-0.004, 0.03] mm^{-1} for all images.

The edge response width (ERW) is defined as follows: a line profile in the L-R direction (perpendicular to the direction of target motion), starting in the centre of the target (higher pixel intensities) and continuing laterally into lung (lower pixel intensities) then ending in lung. The line profile segment length (in millimetres) between the 75% to 25% value of the mean intensity value in the target ROI is the value of ERW. Lower values of ERW represent a "sharper" edge. The CNR, SNR and ERW values were calculated for all ten phase bins and for all nine RT 4D CBCT and conventional 4D CBCT datasets.

3. Results

3.1. Image reconstruction

Image datasets for all 10 phase bins for all 9 respiratory traces for both RT 4D CBCT and conventional 4D CBCT were reconstructed. Cropped and zoomed coronal and axials slices through the target corresponding to the best, middle, and worst (<5th, 40th–60th, >95th percentiles) ranked respiratory traces are shown respectively (figure 5, figure 6, L–R).

The target can be seen located roughly in the middle of the lung. Qualitatively, the image quality deteriorates with more pronounced reconstruction artefacts appearing in the >95th percentile images. On inspection, note that there are some differences between the RT 4D CBCT (top row) and conventional 4D CBCT (bottom row), particularly some diagonal streaking artefacts in the RT 4D CBCT images (figure 5). Figure 6 shows the

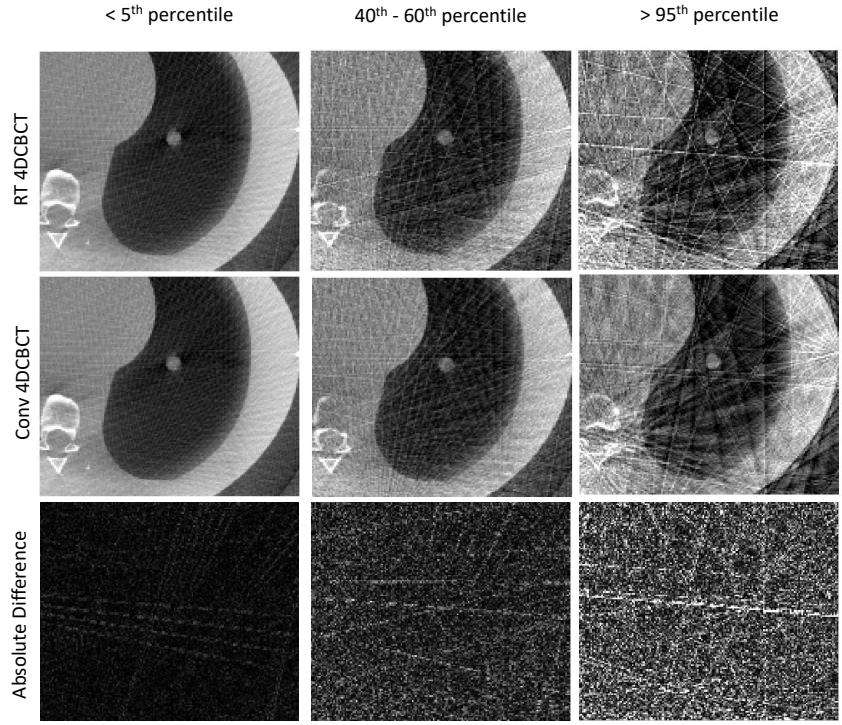

Figure 6. Axial reconstructions through the centre of the spherical target, mid respiratory cycle (bin 6). Top row is RT 4D CBCT, middle row is conventional 4D CBCT, bottom row is absolute difference. Axial reconstructions from the best, middle, and worst respiratory traces (<5th, 40th - 60th, and >95th percentiles) are shown left to right. The Window / Level in uncalibrated attenuation units is [-0.004, 0.03] mm^{-1} for all axial images; for the difference images it is narrower to highlight differences: [0, 0.009].

more obvious streaking artefacts in the >95th percentile axial reconstructions. Absolute pixel difference maps between the RT 4D CBCT and conventional 4D CBCT axial images are included to give a visual comparison with a notable increase in noise and streaks on the >95th percentile images.

3.2. Imaging dose

Imaging dose is compared in a relative way by counting the number of projections acquired for RT 4D CBCT and conventional 4D CBCT for each of the nine respiratory traces. Due to a hardware limitation of the on-board imaging system, it was only possible to suppress every second imaging pulse when running the RT 4D CBCT experiments. Reflecting this experimental limitation, the imaging dose is presented on the bar graph (figure 7) as "RT" (optimal RT 4D CBCT imaging dose with hardware limitation circumvented), "RT*" (experimental RT 4D CBCT imaging dose including hardware limitation), and "CONV" (imaging dose from conventional 4D CBCT). Note that all analyses have been carried out using the number of projections from the optimal "RT"

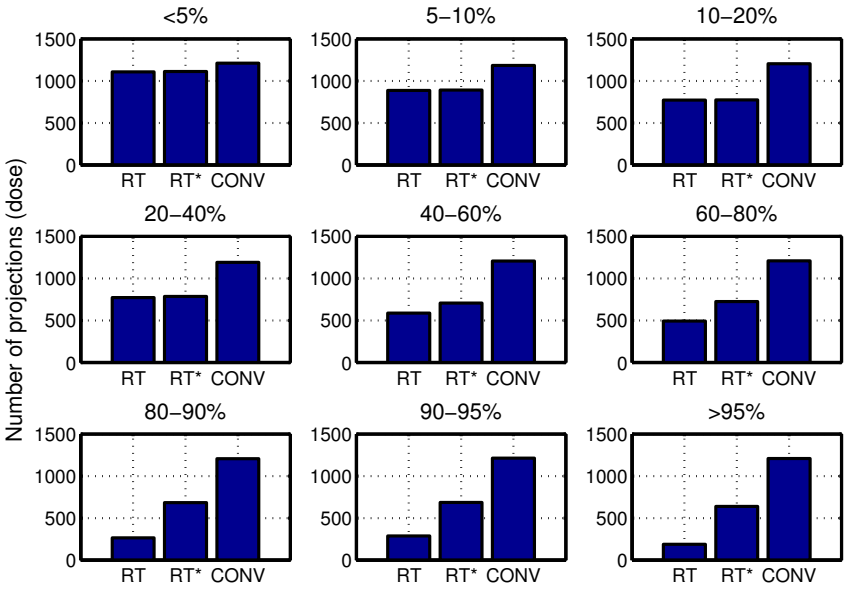

Figure 7. Imaging dose comparisons for each of the nine respiratory traces from their respective rank percentile (cf. 2.3) for optimal and experimental RT 4D CBCT ("RT" and "RT*" respectively), and for conventional 4D CBCT ("CONV").

dose schedule to understand the limits, or worst case imaging performance of an optimal implementation of RT 4D CBCT. The current achievable reduction in projections in these experiments due to the hardware limitation is 50% of the conventional technique. Further discussion on these experimental limitations in dose reduction in RT 4D CBCT follows in section 4.

3.3. Clinical task : measured target trajectory and mean position

The clinical task of measuring the target trajectory and mean position is presented for each of the nine respiratory traces. Phase based binning was used with each plot showing the position of the target over the phase bins 1–10. The reference "ground truth" source trajectory is shown as the heavy weighted line along with both the RT 4D CBCT (solid line) and conventional 4D CBCT (dashed line) trajectories (figure 8). The trajectories are broadly similar comparing the RT 4D CBCT and conventional techniques with the exceptions of the trajectories in 80th–90th percentile, where the RT 4D CBCT trace flattens out at bin 8, and >95 percentile where there are small positional discrepancies. The time-averaged mean target positions are indicated with an O for the ground truth source trajectory, x for the RT 4D CBCT and $*$ for the conventional 4D CBCT trajectories respectively. Across all nine trajectories, the absolute mean target position difference between RT 4D CBCT and the reference ground truth is <0.7 mm. Similarly for conventional 4D CBCT, the absolute mean target position difference is <0.7 mm except for the >95 percentile plot where the difference is 1.3 mm.

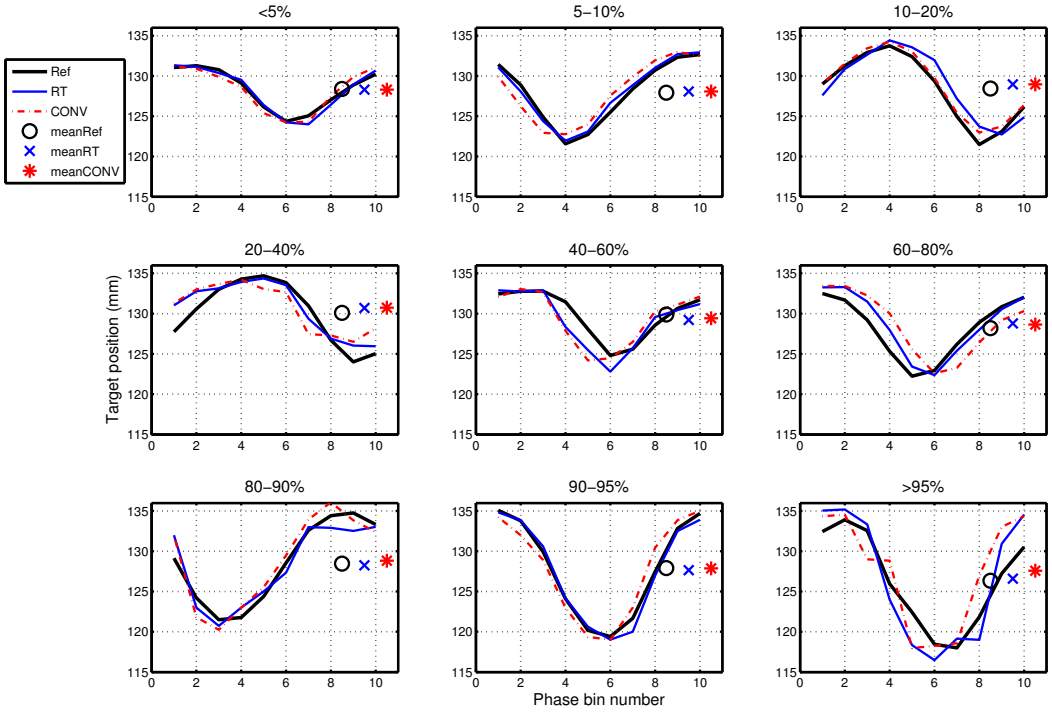

Figure 8. Clinical task showing trajectories of target for all nine respiratory traces and the respective rank percentile (cf. section 2.3). Heavy solid lines are the reference ground truth source trajectory, light solid lines are RT 4D CBCT and dash-dot lines are conventional 4D CBCT trajectories. Markers O, x and $*$ represent the mean target positions for the reference ground truth, RT 4D CBCT and conventional 4D CBCT trajectories respectively.

3.4. Contrast-to-Noise Ratio, Signal-to-Noise Ratio and Edge Response Width

The CNR, SNR and ERW values from all ten phase bins from all nine 4D CBCT datasets are summarised into boxplots for both RT 4D CBCT and conventional 4D CBCT with whiskers representing the maximum and minimum values (figure 9). The median values for both CNR and SNR are slightly higher for conventional 4D CBCT. Based on the Wilcoxon rank-sum test, there is a statistically significant difference for both the CNR and SNR distributions with conventional 4D CBCT scoring better ($p = 0.01$, $p = 0.02$ respectively). There is no statistically significant difference for the ERW distributions from RT 4D CBCT and conventional 4D CBCT ($p = 0.25$).

4. Discussion

For the first time, the RT 4D CBCT acquisition technique has been implemented on a Varian linear accelerator imaging system using a range of patient-measured breathing traces in the experimental work. The experimental platform utilises the real-time

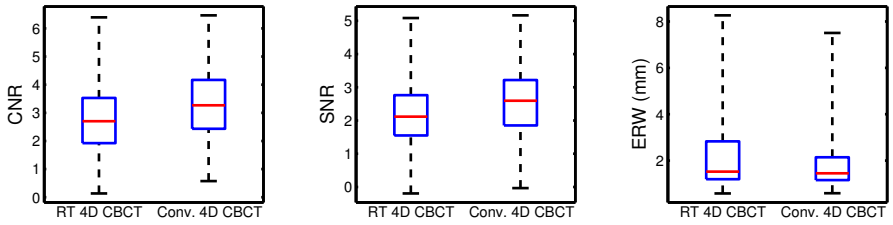

Figure 9. Box plots showing range of CNR values (left), SNR values (middle) and ERW values (right) for all RT 4D CBCT and 4D CBCT datasets. Whiskers represent maximum and minimum values.

respiratory signal being monitored by the Varian RPM system to decide when to drop imaging x-ray pulses so that one projection per phase bin is acquired during the RT 4D CBCT image acquisition. A consequence of RT 4D CBCT is that its projection acquisition rate is in direct proportion to respiration rate of the patient: the slower the respiration rate, the slower the imaging trigger rate and the lower the imaging dose. In contrast, the conventional 4D CBCT acquisition technique simply uses a fixed x-ray fluoroscopic trigger rate (and imaging dose) irrespective of the patient respiration rate. The conventional 4D CBCT technique "wastes" imaging dose when the default constant fluoroscopic trigger rate is higher than is required for a slower respiration rate.

Many efforts have been made to avoid this wastage. CBCT image reconstruction algorithms based on iterative approaches (Sidky and Pan; 2008; Chen et al.; 2008) have been proposed to reduce imaging dose and/or improve image quality in 4D CBCT. Bergner et al. (2010) describe and evaluate a number of classes of iterative algorithms for the purpose of artefact reduction. Iterative image reconstruction approaches often require prior image information and can be time consuming during reconstruction. Nevertheless, Rit et al. (2009) developed an on-the-fly motion compensated CBCT technique which can be used to determine the mean position of each organ despite respiration induced organ motion. The authors suggest their on-the-fly motion compensated technique could replace the need for a 4D CBCT image dataset. Wang and Gu (2013) describe an iterative algorithm which simultaneously estimates target motion and performs reconstruction in 4D CBCT. Here all the measured projections are used for a motion compensated primary CBCT and are then used again to obtain an optimal deformation vector field set that describes tumour motion in all respiratory phases. Yan et al. (2014) report that high quality linac based 4D CBCT imaging can be obtained from a 1 minute CBCT acquisition by solving two optimisation problems: (1) image reconstruction and (2) deformable image registration (utilising a planning CT) to yield anatomical motion. More recently Hansen and Sørensen (2018) demonstrated an iterative reconstruction algorithm that utilises projections from a fixed 4D CBCT scan time of 60 s allowing tumour localisation, even for slow breathers.

The primary clinical use case for 4D CBCT is to measure the range and mean position of mobile targets at patient set-up to determine the positional offset with respect to the treatment beam. This offset is then used to move the patient into alignment

with the treatment beam. This study has demonstrated that the RT 4D CBCT acquisition technique achieves this clinical task with less imaging dose than conventional 4D CBCT. The target trajectory mean positions from the experiments are very similar for RT 4D CBCT and conventional 4D CBCT (figure 8). In all cases the target mean position difference from reference ground truth was found to be <0.7 mm using RT 4D CBCT, as it was also for the first 8 out of 9 cases for conventional 4D CBCT, the exception being for the >95th percentile where the difference was 1.3 mm for conventional 4D CBCT.

In this particular case (>95th percentile), the relative difference in imaging would be stark: 190 against 1208 projections for RT 4D CBCT and conventional 4D CBCT respectively. This was due to the unusually long average respiratory period of 12 s in this respiratory trace and with RT 4D CBCT allowing only one projection per phase bin, this greatly reduces projections required. In contrast, the best case (<5th percentile) required 1107 against 1210 projections for RT 4D CBCT and conventional 4D CBCT respectively. The average respiratory period in this case was a much faster 2.2 s and so RT 4D CBCT only makes a marginal reduction in imaging dose. In all cases RT 4D CBCT uses fewer projections compared to conventional 4D CBCT thus saving in imaging dose to carry out the clinical task of accurate target and treatment beam alignment.

During the course of the experimental work, a limitation of the imaging equipment was identified whereby only every alternate x-ray trigger pulses could be dropped or suppressed without the image acquisition sequence aborting. This currently limits the practical reduction in imaging dose to 50%. A simple work around to this limitation was implemented in the "RTtriggered" program by tagging and rejecting projections that were not triggered from the RT 4D CBCT algorithm. All image reconstruction and analyses for RT 4D CBCT in this work is based on the "unlimited" RT 4D CBCT implementation, not the RT 4D CBCT limited to 50% dose reduction. In principle, it would be a simple matter to remove the current equipment limitation in the implementation of the RT 4D CBCT algorithm with equipment manufacturer support.

The use of the Matlab function *imfindcircles* failed to segment the target circle in 7 out of 90 phase bins for RT 4D CBCT and 4 out of 90 phase bins for conventional 4D CBCT. All failures were from the worst three respiratory traces (80th–90th, 90th–95th, and >95th percentiles). In each case, the target centre and radius were placed manually by visual inspection of the coronal slices. A limitation of this study is the use of a 1 cm diameter spherical target. It facilitated the use of *imfindcircles*, which removes inter- and intra-observer target segmentation, but is a simplified representation of target morphology. The 1 cm diameter target was the smallest available and is more representative of tumour target sizes from the smaller end of the spectrum, for example those targets that might be treated in SBRT. In general, smaller targets are harder to resolve with on-board imaging systems and so the choice to use the 1 cm target in the experimental work approaches the limit of detectability with the conventional 4D CBCT and the RT 4D CBCT techniques.

On inspection of Figure 9, the ERW distributions are comparable for both; the CNR and SNR distributions are slightly better for conventional 4D CBCT compared with RT 4D CBCT. The results from this work are consistent with our previous *in silico* findings (Cooper et al.; 2015) whereby comparable image quality (though quantitatively marginally worse in this work) is achievable with less imaging dose. For the clinical purpose of assessing the range of movement and aligning to the target trajectory mean position, RT 4D CBCT can achieve these clinical goals with less imaging dose.

5. Conclusion

The experimental realisation of real-time Respiratory Triggered 4D CBCT acquisition technique has been demonstrated. RT 4D CBCT couples the respiratory signal to adapt the frame rate of image acquisition system to the patient's respiration rate and requires fewer projections, and therefore less x-ray imaging dose, compared to conventional 4D CBCT. In this study, the target trajectory mean position can be determined by RT 4D CBCT to within 0.7 mm of the reference ground truth target trajectory mean position.

References

Benedict, S. H., Yenice, K. M., Followill, D., Galvin, J. M., Hinson, W., Kavanagh, B., Keall, P., Lovelock, M., Meeks, S., Papiez, L. et al. (2010). Stereotactic body radiation therapy: the report of aapm task group 101, *Medical physics* **37**(8): 4078–4101.

Bergner, F., Berkus, T., Oelhafen, M., Kunz, P., Pan, T., Grimmer, R., Ritschl, L. and Kachelrieß, M. (2010). An investigation of 4d cone-beam ct algorithms for slowly rotating scanners, *Medical physics* **37**(9): 5044–5053.

Chen, G.-H., Tang, J. and Leng, S. (2008). Prior image constrained compressed sensing (piccs): a method to accurately reconstruct dynamic ct images from highly undersampled projection data sets, *Medical physics* **35**(2): 660–663.

Cooper, B. J., O'Brien, R. T., Balik, S., Hugo, G. D. and Keall, P. J. (2013). Respiratory triggered 4d cone-beam computed tomography: A novel method to reduce imaging dose, *Medical physics* **40**(4).

Cooper, B. J., O'Brien, R. T., Kipritidis, J., Shieh, C.-C. and Keall, P. J. (2015). Quantifying the image quality and dose reduction of respiratory triggered 4d cone-beam computed tomography with patient-measured breathing, *Physics in Medicine & Biology* **60**(24): 9493.

Dietrich, L., Jetter, S., Tücking, T., Nill, S. and Oelfke, U. (2006). Linac-integrated 4d cone beam ct: first experimental results, *Physics in Medicine & Biology* **51**(11): 2939.

Fast, M. F., Wisotzky, E., Oelfke, U. and Nill, S. (2013). Actively triggered 4d cone-beam ct acquisition, *Medical Physics* **40**: 091909.

Hansen, D. C. and Sørensen, T. S. (2018). Fast 4d cone-beam ct from 60 s acquisitions, *Physics and Imaging in Radiation Oncology* **5**: 69–75.

Hendee, W. R. and O'Connor, M. K. (2012). Radiation risks of medical imaging: separating fact from fantasy, *Radiology* **264**(2): 312–321.

Kincaid, R. E., Yorke, E. D., Goodman, K. A., Rimner, A., Wu, A. J. and Mageras, G. S. (2013). Investigation of gated cone-beam ct to reduce respiratory motion blurring, *Medical physics* **40**(4).

Li, T., Xing, L., Munro, P., McGuinness, C., Chao, M., Yang, Y., Loo, B. and Koong, A. (2006). Four-dimensional cone-beam computed tomography using an on-board imager, *Medical physics* **33**(10): 3825–3833.

O'Brien, R. T., Cooper, B. J., Shieh, C.-C., Stankovic, U., Keall, P. J. and Sonke, J.-J. (2016). The first implementation of respiratory triggered 4dcbct on a linear accelerator, *Physics in Medicine & Biology* **61**(9): 3488.

O'Brien, R. T., Kipritidis, J., Shieh, C.-C. and Keall, P. J. (2014). Optimizing 4dcbct projection allocation to respiratory bins, *Physics in Medicine & Biology* **59**(19): 5631.

Rit, S., Oliva, M. V., Brousmiche, S., Labarbe, R., Sarrut, D. and Sharp, G. C. (2014). The reconstruction toolkit (rtk), an open-source cone-beam ct reconstruction toolkit based on the insight toolkit (itk), *Journal of Physics: Conference Series*, Vol. 489, IOP Publishing, p. 012079.

Rit, S., Wolthaus, J. W., van Herk, M. and Sonke, J.-J. (2009). On-the-fly motion-compensated cone-beam ct using an a priori model of the respiratory motion, *Medical physics* **36**(6Part1): 2283–2296.

Sidky, E. Y. and Pan, X. (2008). Image reconstruction in circular cone-beam computed tomography by constrained, total-variation minimization, *Physics in Medicine & Biology* **53**(17): 4777.

Simpson, D. R., Lawson, J. D., Nath, S. K., Rose, B. S., Mundt, A. J. and Mell, L. K. (2009). Utilization of advanced imaging technologies for target delineation in radiation oncology, *Journal of the American College of Radiology* **6**(12): 876–883.

Sonke, J.-J., Zijp, L., Remeijer, P. and van Herk, M. (2005). Respiratory correlated cone beam ct, *Medical physics* **32**(4): 1176–1186.

Wang, J. and Gu, X. (2013). Simultaneous motion estimation and image reconstruction (smeir) for 4d cone-beam ct, *Medical physics* **40**(10).

Yan, H., Zhen, X., Folkerts, M., Li, Y., Pan, T., Cervino, L., Jiang, S. B. and Jia, X. (2014). A hybrid reconstruction algorithm for fast and accurate 4d cone-beam ct imaging, *Medical physics* **41**(7).

7

CONCLUSION

Imaging in radiation therapy is an essential component to achieving therapeutic goals for oncology patients. However, as a general principle it is always necessary to find the balance between clinically suitable radiological imaging and minimal radiation exposure, the so called ALARA principle - As Low As Reasonably Achievable. The ARPANSA[1] Code of Practice states:

> *"Radiation doses that arise from medical radiation exposures and those received by the public and occupationally exposed persons must be kept as low as reasonably achievable, economic and social factors being taken into account"* (ARPANSA, 2008).

To this end, Respiratory Triggered 4D Cone-beam Computed Tomography helps to reduce imaging dose for patients receiving 4D imaging prior to radiation treatment and it is capable of producing clinically relevant information with less radiation exposure to patients.

Chapter 4 focuses on the investigation and establishment of the RT 4D CBCT concept, where projection acquisitions are restricted temporally according to the patient's respiration rate, revealed some initial properties of the algorithm: (1) the possible projection (imaging dose) reduction is directly proportional to the rate of respiration; (2) removes "clustering" effect that causes redundant projections; (3) phase based binning gives better quality images compared to displacement based binning when applying the RT 4D CBCT acquisition technique.

Perhaps the biggest limitation of this first study was the assumption of a sinusoidal respiratory signal. The perfectly regular pattern allowed an exploratory study of a "best case" performance of the RT 4D CBCT algorithm and sets an upper bound of what to expect with the following experiments in Chapter 5 and Chapter 6 where real patient respiratory signals were utilised.

1 Australian Radiation Protection and Nuclear Safety Agency

Chapter 5 addresses the sinusoidal respiratory signal limitation of the first study (Chapter 4). To achieve this, 111 patient-measured respiratory signals were used to model the imaging acquisitions for RT 4D CBCT and conventional 4D CBCT. Simulations were conducted with both a stationary thorax phantom and *in silico* using a dynamic digital phantom, "XCAT" (Segars et al., 2010). These approaches enabled a comparison of the RT 4D CBCT and conventional 4D CBCT acquisition techniques with and without the potential confounding effects of target motion respectively. To be clear, there is no target motion with the stationary thorax phantom. In this case, the 111 respiratory signals are still used for subdividing or binning the projections according to respiratory phase, allowing the investigation of RT 4D CBCT and conventional 4D CBCT behaviour in isolation from motion.

Major findings from this work are (1) RT 4D CBCT removes redundant projections in a phase bin; (2) RT 4D CBCT is much more efficient with imaging dose to produce similar, albeit marginally worse, quality images (see figures 6 and 7 from chapter 4); and (3) these findings hold true for a diverse range of respiratory signal traces (111 traces from 24 patients). The image quality versus image dose plots (figures 8 and 9 from chapter 4) is suggestive that RT 4D CBCT might be approaching an optimal allocation in terms of dose, i.e. 1 projection per phase bin, for a given image quality value. The problem with this is that image quality is bound by the respiration rate - slower breathers will need less dose but results in poorer quality images. Nevertheless, even though a poor quality image may not be aesthetically pleasing, it may still be of value depending on the clinical task at hand. A central clinical task that 4D CBCT imaging helps to fulfil is verifying mobile tumour target's motion range and mean position immediately before a therapy dose of radiation is delivered to the patient.

Chapter 6 builds on the previous two chapters. This work focuses on the development of RT 4D CBCT in a prototype experimental system in real-time, taking a live respiratory signal and realising the RT 4D CBCT algorithm by triggering the linear accelerator's on-board kilovoltage x-ray imaging system. Based on a wide range of patient respiratory traces from Chapter 5, tumour trajectories were created for a

dynamic thorax phantom for nine patient traces. Each trajectory was "played back" individually, thus creating conditions for imaging as it would be for a patient, and both RT 4D CBCT and conventional 4D CBCT imaging was performed.

Analyses of the resulting cone-beam CT datasets led to a major result that RT 4D CBCT is able to reproduce a target trajectory mean position to within 0.7 mm of the reference source target trajectory in a dynamic thorax phantom for the range of trajectories studied, including fast and slow respiration rates. This was achievable with a mean imaging dose reduction of 50% over the nine patient traces compared to conventional 4D CBCT. The image quality for slower breathers was a little worse for RT 4D CBCT (see figure 6 from chapter 5) but crucially, the degradation in image quality for RT 4D CBCT did not adversely affect the ability to extract tumour target trajectories and mean positions (see figure 8 from chapter 5).

The obligation as set out in the ARPANSA Code of Practice (ARPANSA, 2008), that only the minimal dose required for the clinical need is justified, is being achieved. In this case, RT 4D CBCT is a demonstrably more optimal use of ionising radiation than conventional 4D CBCT.

7.1 FUTURE DIRECTIONS

Based on the outcomes from this project, a small retrospective clinical pilot study with real patients could be justified. Such a pilot study could be conducted with minimal risk as follows. Exploiting the fact that RT 4D CBCT is a subset of conventional 4D CBCT, the only additional requirement would be a respiratory signal that is correlated to the conventional 4D CBCT scan. Informed patients willing to participate and indicated for a 4D CBCT scan could give consent for a copy of the imaging projection data to be reconstructed retrospectively according to the RT 4D CBCT algorithm. Similar analyses as outlined in this project would provide further evidence of whether RT 4D CBCT can achieve the same clinical goal(s) as conventional 4D CBCT but with a considerably more optimal use of x-ray radi-

ation. If a positive outcome can be demonstrated from the retrospective study, then a more detailed prospective study could follow where RT 4D CBCT is applied prospectively.

Another direction for exploring is utilising a different cone-beam CT reconstruction package. The Feldkamp-Davis-Kress (FDK) cone-beam reconstruction algorithm has been used exclusively in this work. Shieh et al. (2014) found that "better [than FDK] reconstruction algorithms were shown to improve image quality almost 100% of the time." In this space, an interesting study would examine whether RT 4D CBCT might give better quality or more clinically useful images when using an iterative-based CBCT reconstruction algorithm instead of FDK.

A related and more complex approach for improved 4D imaging is "respiratory motion guided four dimensional cone beam computed tomography" (RMG-4DCBCT) as described by O'Brien et al. (2014) and is included as an appendix (see Chapter 8). In this approach, an optimisation routine is used to solve an objective function that minimises the difference between the angular separation of any consecutive projections within the phase bins and the mean angular separation for projections. The respiratory signal is used to compute optimal time windows for projections to be acquired and there are two constrained degrees of freedom to achieve this: imaging frequency and gantry velocity. Despite the complexities, one major advantage of RMG-4DCBCT is that image acquisition time and projection clustering may be further reduced by means of the additional degree of freedom (ability to slow or hasten gantry velocity). Recent work modelling a robotic C-Arm CBCT system's capabilities for the purpose of efficient surgical cardiac imaging (Reynolds et al., 2018) suggest that these robotic CBCT imaging systems could overcome some of the optimisation constraints relating to physical limitations of existing kilovoltage x-ray imaging systems that are attached to linacs.

The experimental platform for Respiratory Triggered 4D CBCT as a dose sparing imaging technique for pre-treatment radiation therapy patients has been demonstrated, at least for an anthropomorphic dynamic phantom. There are several future directions that could be pursued for the further development of RT 4D CBCT.

In its current implementation, it is an uncomplicated concept that would not pose great technical difficulty for medical linear accelerator (linac) manufacturers to implement. The major equipment components required, i.e. external respiratory sensor, on-board kilovoltage x-ray imaging system, are generally packaged as standard accessories for Varian[2] linacs. A small additional control circuit containing the RT 4D CBCT algorithm logic would be needed, currently implemented on a Raspberry Pi[3] mini computer for the experiments in Chapter 6, to realise the feedback loop between the respiratory signal and the projection triggering.

2 Varian Medical Systems, Inc. 3100 Hansen Way, Palo Alto, CA 94304-1038, USA
3 Raspberry Pi Foundation, UK Registered Charity 1129409, UK

REFERENCES

ARPANSA 2008 'Code of practice for radiation protection in the medical applications of ionizing radiation' ARPANSA, 619 Lower Plenty Road, Yallambie, Victoria, 3085.

O'Brien R T, Cooper B J, Kipritidis J, Shieh C C and Keall P J 2014 *Phys Med Biol* **59**(3), 579.

Reynolds T, Shieh C, O'Brien R and Keall P 2018 *in* '60th Annual Meeting of the American Association of Physics in Medicine'.
URL: *https://w3.aapm.org/meetings/2018AM/programInfo/programAbs.php?sid=7511&aid=39670*

Segars W, Sturgeon G, Mendonca S, Grimes J and Tsui B 2010 *Medical Physics* **37**(9), 4902–4915.

Shieh C C, Kipritidis J, O'Brien R T, Kuncic Z and Keall P J 2014 *Medical Physics* **41**(4), 041912.

8

APPENDIX 1

Respiratory Motion Guided 4-dimensional cone-beam computed tomography is a experimental CBCT acquisition technique where both the gantry speed and the imager frequency is optimised according to the detected respiratory signal of a patient. I was the second author of the paper presented below.

IOP Publishing | Institute of Physics and Engineering in Medicine Physics in Medicine and Biology

Phys. Med. Biol. **59** (2014) 579–595 doi:10.1088/0031-9155/59/3/579

Respiratory motion guided four dimensional cone beam computed tomography: encompassing irregular breathing

Ricky T O'Brien[1], Benjamin J Cooper[1,2], John Kipritidis[1], Chun-Chien Shieh[1,3] and Paul J Keall[1]

[1] Radiation Physics Laboratory, Sydney Medical School, The University of Sydney, NSW 2006, Australia
[2] Department of Medical Physics, The Canberra Hospital, ACT 2605, Australia
[3] Institute of Medical Physics, School of Physics, The University of Sydney, NSW 2006, Australia

E-mail: ricky.obrien@sydney.edu.au

Received 22 August 2013, revised 30 October 2013
Accepted for publication 29 November 2013
Published 17 January 2014

Abstract

Four dimensional cone beam computed tomography (4DCBCT) images suffer from angular under sampling and bunching of projections due to a lack of feedback between the respiratory signal and the acquisition system. To address this problem, respiratory motion guided 4DCBCT (RMG-4DCBCT) regulates the gantry velocity and projection time interval, in response to the patient's respiratory signal, with the aim of acquiring evenly spaced projections in a number of phase or displacement bins during the respiratory cycle. Our previous study of RMG-4DCBCT was limited to sinusoidal breathing traces. Here we expand on that work to provide a practical algorithm for the case of real patient breathing data. We give a complete description of RMG-4DCBCT including full details on how to implement the algorithms to determine when to move the gantry and when to acquire projections in response to the patient's respiratory signal. We simulate a realistic working RMG-4DCBCT system using 112 breathing traces from 24 lung cancer patients. Acquisition used phase-based binning and parameter settings typically used on commercial 4DCBCT systems (4 min acquisition time, 1200 projections across 10 respiratory bins), with the acceleration and velocity constraints of current generation linear accelerators. We quantified streaking artefacts and image noise for conventional and RMG-4DCBCT methods by reconstructing projection data selected from an oversampled set of Catphan phantom projections. RMG-4DCBCT allows us to optimally trade-off image quality, acquisition time and image dose.

0031-9155/14/030579+17$33.00 © 2014 Institute of Physics and Engineering in Medicine Printed in the UK & the USA

For example, for the same image quality and acquisition time as conventional 4DCBCT approximately half the imaging dose is needed. Alternatively, for the same imaging dose, the image quality as measured by the signal to noise ratio, is improved by 63% on average. C-arm cone beam computed tomography systems, with an acceleration up to $200^\circ/s^2$, a velocity up to $100^\circ/s$ and the acquisition of 80 projections per second, allow the image acquisition time to be reduced to below 60 s. We have made considerable progress towards realizing a system to reduce projection clustering in conventional 4DCBCT imaging and hence reduce the imaging dose to the patient.

Keywords: respiratory motion guided 4DCBCT, RMG-4DCBCT, 4DCBCT

(Some figures may appear in colour only in the online journal)

1. Introduction

The United States Food and Drugs Administration's (FDA's) initiative to reduce unnecessary radiation exposure from medical imaging, Image Wisely and Image Gently[4] are three high profile campaigns to increase public and clinical awareness on the risks and undesirable side effects associated with radiation delivered during medical imaging. In an ideal world, preference would be given to an imaging modality if medically relevant images can be acquired with a lower radiation dose. However, in practice, the financial cost of the imaging modality, the benefit to the patient, the time required to acquire the images, patient discomfort and the imaging dose are all balanced before an imaging modality is selected.

An emerging clinical image guidance strategy for tumour sites affected by respiratory motion is four dimensional cone beam computed tomography (4DCBCT) in which a series of approximately 1200 kV images, or projections, are used to reconstruct a 3D view of the patient's anatomy (Taguchi 2003, Sonke *et al* 2005). Elekta released 4DCBCT as part of their Symmetry product in 2009 while Varian released 4DCBCT in 2013 as part of their Advanced IGRT package on TrueBeam 2.0. The clinical drivers for 4DCBCT are the desire to obtain, on the day of treatment, information on the average tumour position, the amplitude of the tumour motion, validation of the treatment plan, inter fraction changes in the tumour size and shape and to improve the accuracy of image-guidance (Sweeney *et al* 2012). 4DCBCT is also the subject of substantial research and development efforts. A pubmed search of '4d Cone Beam CT' on 18/10/2013 yielded 119 articles, with over half of these articles (63) published in the last 2.5 yr indicating substantial growth in the 4DCBCT topic. However, the accumulated radiation dose delivered to a patient from frequent use of 4DCBCT over the course of their treatment can be significant and efforts to reduce the radiation dose from 4DCBCT imaging will have a direct benefit to the patient.

Projection clustering, that is inherent in conventional 4DCBCT techniques, is known to cause streak artefacts and degrade image quality (Leng *et al* 2008). This paper is concerned with respiratory motion guided 4DCBCT (RMG-4DCBCT), which is a technique that can be used to reduce projection clustering and improve image quality when acquiring 4DCBCT images.

[4] www.fda.gov/Radiation-EmittingProducts/RadiationSafety/RadiationDoseReduction/default.htm, www.imagewisely.org/ and www.pedrad.org/associations/5364/ig/ respectively. The International Commission on Radiological Protection's (ICRP's) As Low As Reasonably Achievable (ALARA) principle is another campaign to reduce radiation exposure.

RMG-4DCBCT utilises the real-time respiratory signal enabling two additional degrees of freedom over conventional 4DCBCT: (1) the velocity of the gantry can be varied and (2) the time interval between projections can be varied. Varying the velocity of the gantry and the time interval between projections allows us to improve the angular spacing of projections and to improve the image quality of 4DCBCT images.

In our previous study, (O'Brien *et al* 2013), we introduced a mathematical framework for the optimization algorithms that are used to compute the optimal gantry velocity and projection time interval schedule for RMG-4DCBCT. The optimization algorithms in our previous study were demonstrated only on simulated sinusoidal breathing traces and not real patient breathing data. This paper builds on our previous studies by implementing the optimization into a realistic simulation of a working RMG-4DCBCT software package. We will give complete details on the software system that is used to implement RMG-4DCBCT in a simulated environment. We will introduce the algorithms that are used to determine when to move the gantry, how to move the gantry smoothly and when to acquire a projection. To make the system more realistic we have developed a simulated gantry and a simulated kilovoltage imager and commands are issued to the simulated system. We establish that RMG-4DCBCT is an effective method to reduce projection clustering by performing a realistic simulation of a working RMG-4DCBCT system using 112 breathing traces from 24 lung cancer patients acquired in a previous study (George *et al* 2006).

2. Theory

In this section we demonstrate why projection clustering occurs in 4DCBCT and how the algorithms are implemented in an RMG-4DCBCT system.

2.1. 4DCBCT imaging and projection clustering

Modern linear accelerators are equipped with kilovoltage (kV) imagers which are used to position patients for treatment. By rotating the gantry, containing the kV imager and detector, around the patient a series of approximately 1200 images, or projections, can be acquired. We will refer to the kV images as projections throughout the remainder of this paper. The projections are used to reconstruct a three dimensional image, or cone beam computed tomography (CBCT) image, of the patient's anatomy using the Feldkamp–Davis–Kress algorithm (Feldkamp *et al* 1984). The whole process takes several minutes to acquire the projections necessary to reconstruct a CBCT image of acceptable quality for radiotherapy.

A major problem with CBCT imaging is respiratory motion, which causes artefacts and blurring in the resulting 3D image because the anatomy is continuously moving during the projection acquisition process. To overcome the problems associated with respiratory motion, 4DCBCT techniques have been developed (Taguchi 2003, Sonke *et al* 2005) and commercially released in 2009 by Elekta (Stockholm Sweden). The aim of 4DCBCT imaging is to collect a full set of projections in a number of phase or displacement respiratory bins. Within each respiratory bin there is little anatomical motion so blurring and artefacts in the resulting images are reduced. For example, projections taken at the inhale or exhale limit are allocated to the inhale or exhale limit respiratory bins respectively and are used to reconstruct a 3D image for the corresponding respiratory bin.

Common to all current 4DCBCT systems is the use of a constant gantry velocity with a constant projection pulse rate. After the projections have been acquired, they are compared to the recorded respiratory signal and then post-processed into respiratory bins. Throughout the image acquisition process there is no feedback from the respiratory signal to the acquisition

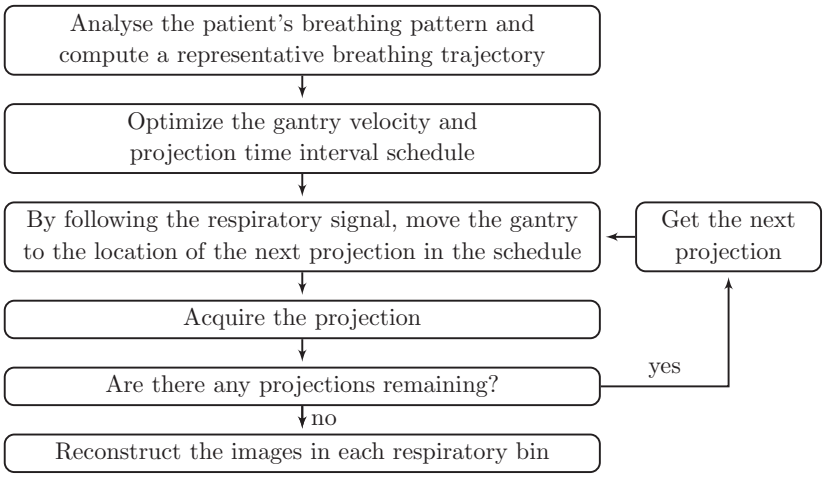

Figure 1. A flowchart showing the main algorithm controlling RMG-4DCBCT.

system. This leads to a cluster of projections while the breathing signal is in a respiratory bin, followed by a gap as the gantry continues to move while we wait for the respiratory signal to re-enter the respiratory bin. Clustering of projections leads to streak artefacts in the reconstructed images (Leng *et al* 2008).

2.2. RMG-4DCBCT

In order to reduce projection clustering there are two additional degrees of freedom used in RMG-4DCBCT. The first degree of freedom allows the velocity of the gantry to be regulated within specified limits on maximum velocity and maximum acceleration. The second degree of freedom allows the time interval between projections to be regulated, i.e. the projections can be brought forward or delayed. These two degrees of freedom allow us to speed up the gantry and delay projections with the aim of improving the angular separation between projections. Figure 1 gives a flowchart for RMG-4DCBCT. We describe each step in the process in more detail, and give implementation details, in the remainder of this section.

2.3. Analyse the patient's breathing pattern and compute a representative breathing trajectory

A respiratory signal can be derived from the projections themselves (Zijp *et al* 2004, Van Herk *et al* 2007, Berbeco *et al* 2005, Kavanagh *et al* 2009, Vergalasova *et al* 2012) or from an external respiratory sensor such as the Real-Time Position Management System (RPM) (Varian Medical Systems, Palo Alto, CA, USA). In this study we use the RPM system which has a frequency of 30 Hz because we have a large database of RPM breathing traces from lung cancer patients. We denote the respiratory signal as $R(t_i)$ for $i = 1, 2, \ldots$ where $t_{i+1} - t_i = 33$ ms for the RPM system.

The RPM data is sent via serial port to the RMG-4DCBCT software and includes the real-time displacement of a marker block placed on the patients abdomen and a real-time estimate of the patient's breathing phase. In addition to receiving respiratory data directly from the RPM computer an RPM emulator has been developed to read files saved from a previous study and to send the data to the RMG-4DCBCT software via serial port. This allows

us to use an RPM signal from data previously recorded for lung cancer patients as if the patient were present.

For the optimization in the next section a representative breathing trajectory is required. Although the optimization could be improved with an accurate prediction of the patient's breathing, a highly accurate prediction is both technically difficult and not necessary. To keep the system simple, we monitor ten breathing cycles, compute the average baseline, phase and range of motion of the respiratory signal, and then use a sine wave for the representative breathing trajectory used to optimize the acquisition schedule.

2.4. Optimize the gantry velocity and projection time interval schedule

Optimizing the gantry velocity and projection time interval schedule is achieved using mixed integer quadratic programming (MIQP) techniques (O'Brien *et al* 2013). The method minimizes the root mean square (RMS) of the difference between the angular separation and the mean angular separation for projections in the same respiratory bin. Mathematically, the RMS can be defined by assuming that we have N respiratory bins with M_b projections taken in bin b, we let $\theta_{b,l}$ for $b = 1, 2, \ldots, N$ and $l = 1, 2, \ldots, M_b$ be the lth largest gantry angle for the projections taken in respiratory bin b, then the RMS in bin b is

$$\mathrm{RMS}_b^2 = \left\{ \sum_{l=1}^{M_b-1} (\theta_{b,l+1} - \theta_{b,l} - \Delta\theta_b)^2 + (2\pi - (\theta_{b,M_b} - \theta_{b,0}) - \Delta\theta_b)^2 \right\} \Big/ M_b, \tag{1}$$

where $\Delta\theta_b = 2\pi/M_b$ is the average angular separation between projections. The term in the summation $(\theta_{b,l+1} - \theta_{b,l} - \Delta\theta_b)$ is the angular distance between projections minus the average angular separation. The final term $(2\pi - (\theta_{b,M_b} - \theta_{b,0}) - \Delta\theta_b)$ is the angular separation between the first and last projection minus the average angular separation. The objective function, or RMS, that is minimized is

$$\mathrm{RMS}^2 = \text{Minimize} \sum_{b=1}^{N} \mathrm{RMS}_b^2 / N. \tag{2}$$

Additional constraints are applied on the maximum velocity and acceleration of the gantry, the minimum time between projections and to ensure that M_b projections are collected in respiratory bin b. We refer to our previous study for more details on the implementation of the optimization algorithms (O'Brien *et al* 2013).

For safety reasons, the International Electrotechnical Commission (IEC) specifies a maximum velocity of $6^\circ/\mathrm{s}$ which is the maximum velocity for most linear accelerators. Values for acceleration have been measured at between $1.8^\circ/\mathrm{s}^2$ and $3.2^\circ/\mathrm{s}^2$, and deceleration at between $3.4^\circ/\mathrm{s}^2$ and $4.3^\circ/\mathrm{s}^2$ for the Elekta Synergy linear accelerator (Boylan *et al* 2011). Values for acceleration and deceleration for non emergency stops on the Varian Medical Systems TrueBeam are around $12^\circ/\mathrm{s}^2$ [5]. Conventional kilovoltage imagers are capable of acquiring images at a rate of at least 10 Hz, so in our optimization we will apply a constraint ensuring that projections are taken at least 100 ms apart. At the high end of the acceleration and velocity scale are the C-arm systems that are capable of a velocity of $100^\circ/\mathrm{s}$, an acceleration of $200^\circ/\mathrm{s}^2$ and a projection pulse rate of 80 Hz.[6]

A heuristic solution method to the MIQP model that obtains a near optimal gantry velocity and projection time interval schedule in under one second is given by O'Brien *et al* (2013). The

[5] Personal communication with Scott Johnson, Sr Manager, Research Collaborations, Varian Medical Systems, 5 September 2012.

[6] http://zeegolab.stanford.edu/

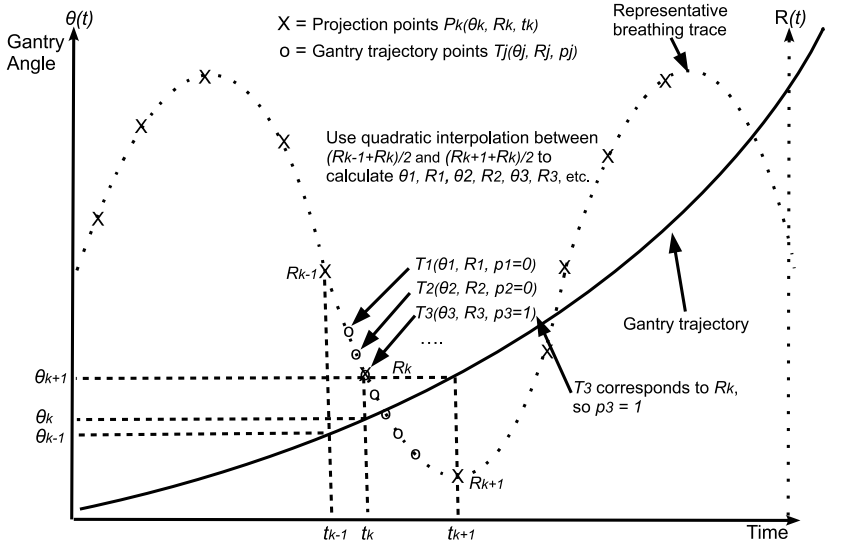

Figure 2. A schematic depicting how the projection points $P_k(\theta_k, R_k, t_k)$ are used to determine the gantry trajectory points $T_j(R_j, \theta_j, p_j)$ between $(R_{k-1} + R_k)/2$ and $(R_{k+1} + R_k)/2$.

output of the optimization is a sequence of projections points, P_k, containing the representative respiratory signal, R_k, gantry angle, θ_k, and estimated acquisition time, t_k

$$P_k(\theta_k, R_k, t_k) \text{ for } k = 1, 2, \ldots, M,$$

where M is the total number of projections $M = \sum_{b=1}^{N} M_b$.

2.5. Following the respiratory signal and moving the gantry to the location of the next projection in the schedule

The projection sequence points, P_k, are given when projections need to be taken and are separated by a time interval of at least 100 ms. To move the gantry smoothly, we need to interpolate between the projection points to obtain a trajectory for the gantry at a resolution of around 10–50 ms. There are two parameters that we could use to perform the interpolation: either use time t_k, or, the respiratory signal R_k. Time t_k is a bad choice because the patient's breathing trace will quickly drift away from the representative breathing trace. Projections need to be taken when the respiratory signal is in the correct position, so interpolation is performed using the respiratory signal, R_k. We need to continuously monitor the respiratory signal and trigger projections based on the respiratory signal and not time.

We interpolate using a quadratic function to fit gantry trajectory points, this is schematically depicted in figure 2. That is, we use the respiratory signal at, R_{k-1}, R_k and R_{k+1} to fit a quadratic curve and interpolate between $(R_{k-1} + R_k)/2 \leqslant R < (R_{k+1} + R_k)/2$

$$\theta(R) = AR^2 + BR + C \text{ for } (R_{k-1} + R_k)/2 \leqslant R < (R_{k+1} + R_k)/2,$$

where

$$A = \left[(\theta_k - \theta_{k-1})(R_{k-1} - R_{k+1}) + (\theta_{k+1} - \theta_{k-1})(R_k - R_{k-1})\right] \Big/ \left[(R_{k-1} - R_{k+1})\left(R_k^2 - R_{k-1}^2\right) + (R_k - R_{k-1})\left(R_{k+1}^2 - R_{k-1}^2\right)\right],$$

$$B = \left[(\theta_{k+1} - \theta_k) - A(R_{k+1}^2 - R_{k-1}^2)\right] / (R_k - R_{k-1}),$$

$$C = \theta_{k-1} - AR_{k-1}^2 - BR_{k-1}.$$

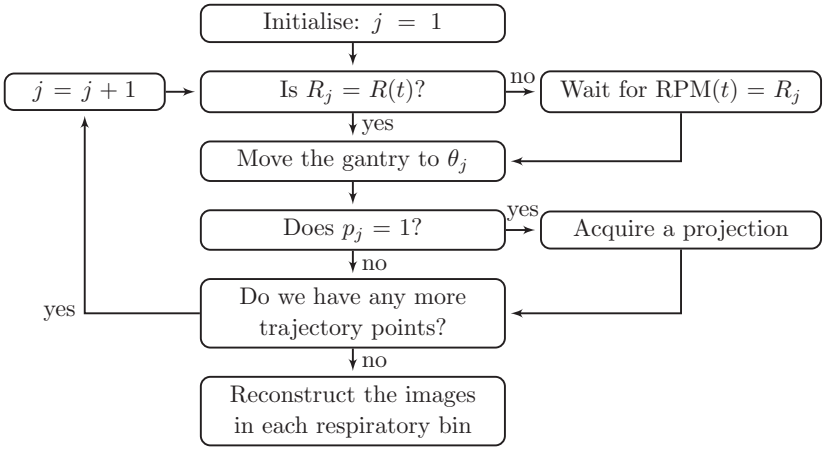

Figure 3. A flowchart showing how to move the gantry to each trajectory point. This algorithm moves the gantry to trajectory points θ_j for $j = 1, 2, \ldots$.

We use this equation to compute a sequence of gantry trajectory points, $T_j(R_j, \theta_j, p_j)$ for $j = 1, 2, \ldots$ at a resolution of around 10–50 ms. The parameter p_j is 1 if the trajectory point corresponds to a projection point and zero otherwise.

Once we have computed the gantry trajectory points, we use them to move the gantry in response to the patient's real-time respiratory signal. We start with $j = 1$, when the patient's respiratory signal, $R(t)$ is R_1 we move the gantry to θ_1. If a projection is to be taken, i.e. $p_j = 1$, we issue a command to the imager to take a projection. We then set $j = 2, 3, \ldots$ and repeat the process. A flowchart of this process is given in figure 3 with the details required to wait for $R(t) = R_j$ discussed in the next section.

2.5.1. Predicting the respiratory signal and waiting for $R(t) = R_j$. The gantry trajectory points are at a resolution of 10–50 ms while the RPM signal is received at a resolution of 33 ms. It is therefore necessary to predict the RPM signal for up to 33 ms. For example, assuming phase goes from 0 to 2π, if our next gantry trajectory point indicates that the gantry should be moved when the phase is 1.025 and the last two RPM signals were 0.9 and 1.0, we expect a phase of 1.025 to occur before we receive the next respiratory signal. With a prediction interval of at most 33 ms, we use linear extrapolation to predict the respiratory signal. More complicated algorithms can be used to predict the respiratory signal with reasonable accuracy for intervals between 200–500 ms (Krauss *et al* 2011).

2.5.2. Prediction errors. Figure 4 is a diagram showing that projections can be taken in the wrong respiratory bin because of errors in predicting the respiratory signal. In figure 4, a projection is required with a phase of 1.17. We predict that the phase will be 1.17 at 55 ms and acquire the projection at this time. However, when we receive the next signal, at 66 ms, we find that the prediction was incorrect and the projection was taken in the bin 3 not bin 2. To reduce the occurrence of prediction errors we add a buffer to respiratory bins when optimizing the projection schedule so that projections are not taken close to the boundary of a time window. We have found that a 5 ms buffer on the respiratory bins is sufficient in most cases.

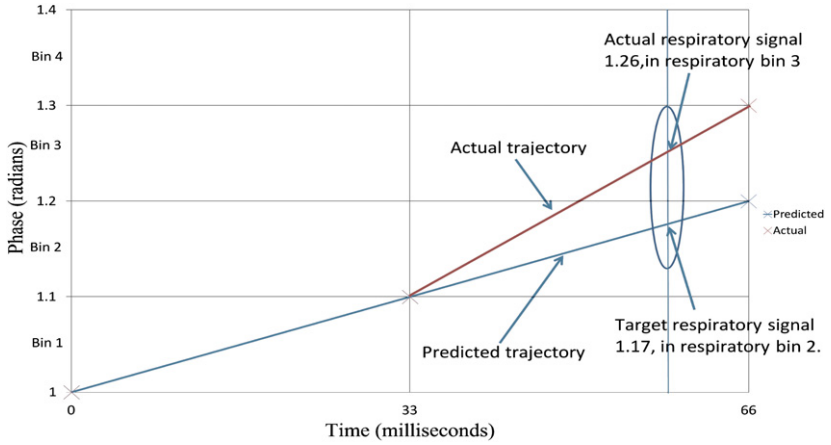

Figure 4. Prediction errors: an RPM signal is received at time 0 and 33 ms. A projection is required when the phase is 1.17 which is predicted to occur at 55 ms. We issue a command to the kilovoltage imager to acquire a projection at 55 ms. However, once we receive the RPM signal at 66 ms we find that the projection was actually taken in bin 3, not bin 2.

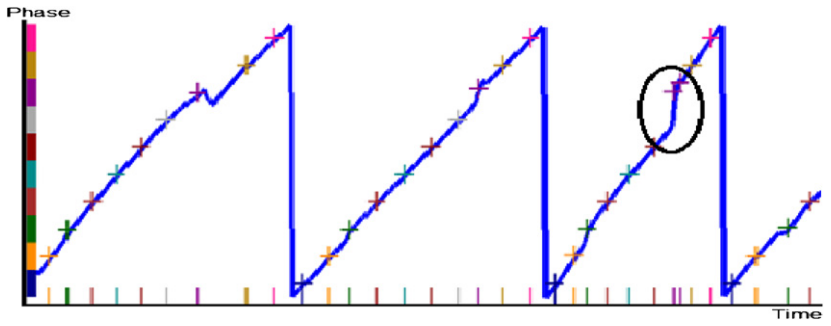

Figure 5. An example of sudden jumps in the RPM phase signal. A screen shot from the RMG-4DCBCT software showing the phase signal over three respiratory cycles (15 s). The ten colours on the left-hand side identify the respiratory bins and the crosses correspond to projections taken using RMG-4DCBCT. The area marked with the ellipse shows a region where the respiratory signal suddenly jumps. Also note that the first two breathing cycles exhibit similar, but smaller, jumps.

2.5.3. Large jumps in the real-time phase signal. On our database of breathing traces from lung cancer patients the real-time phase signal contains fast transitions or 'jumps' in the phase. Figure 5 is a screen shot from our RMG-4DCBCT software showing an example of jumps in the real-time phase signal. When a jump occurs the problems mentioned in the previous section are greatly magnified and there is no way of guaranteeing that the projection will be taken in the correct respiratory bin. In the example in figure 5 the first of the two projections allocated to the pink respiratory bin should have been taken in the preceding respiratory bin. If the imager is capable of a high frame rate, where four or five projections could be acquired between respiratory signals, the quality of the real-time phase signal can be the biggest factor influencing acquisition.

Table 1. Default parameters used for the four 4DCBCT methods. The relative dose is the radiation dose delivered from the imaging technique relative to conventional 4DCBCT. ω is the average breathing period of the patient.

	Conventional 4DCBCT	RMG-4DCBCT$^{1200}_{240}$	RMG-4DCBCT$^{1200}_{-}$	RMG-4DCBCT$^{600}_{-}$
Gantry velocity	1.5°/s	Varies	Varies	Varies
Gantry acceleration	0°/s^2	Varies	Varies	Varies
Projections/bin	NA	120	120	60
Total projections	1200	1200	1200	600
Imaging time	240 s	$\approx$ 240 s	120 $\times$ ω	60 $\times$ ω
Relative dose	1	1	1	0.5

There are two options on what we can do with the projection if a jump occurs:

(i) Allocate the projection to the respiratory bin that the projection was taken (i.e. we allocate both projections in figure 5 to the pink respiratory bin).
(ii) Because the phase signal is changing rapidly, the resulting projection can be allocated to the target, or expected, respiratory bin (i.e. we allocate the first projection to the blue respiratory bin in figure 5).

Throughout this study we will use option i because it represents the worst case scenario as far as the angular separation of projections is concerned. Option ii will produce better angular separation between projections, but further studies of clinical images will be needed to assess the impact on image quality.

2.5.4. Alternative phase signals. As an alternative to the phase signal computed by the RPM sensor, we have implemented the method of Ruan *et al* (2009) to compute a real-time phase estimate. To further reduce the high frequency oscillations in the respiratory signal we have also applied a low pass filter to the respiratory data when implementing the Ruan real-time phase estimation.

3. Method

Four different 4DCBCT algorithms have been studied. Figure 6 gives a screen shot from the RMG-4DCBCT software showing the differences between the four 4DCBCT algorithms with the parameters used for the 4DCBCT methods summarized in table 1. Each algorithm will be discussed in more detail below.

In the following discussion we will use the word *time window* to refer to the time between the entry and exit of a respiratory bin in a single breathing cycle. Each respiratory bin is made up of a number of time windows; one time window for each breathing cycle. Unless the gantry is moving rapidly, if multiple projections are acquired in a time window the projections are likely to be clustered together.

3.1. Conventional 4DCBCT

The conventional 4DCBCT algorithm is used to simulate current generation 4DCBCT devices. In current generation commercial systems the gantry is rotated at around 1.5°/s, taking 240 s to complete one full revolution of the patient. A projection pulse rate of between 5Hz–10 Hz is commonly employed. We will use a pulse rate of 5 Hz, or, 0.2 s in this study for a total of 1200 projections. Using conventional 4DCBCT, we expect to see projection clustering as

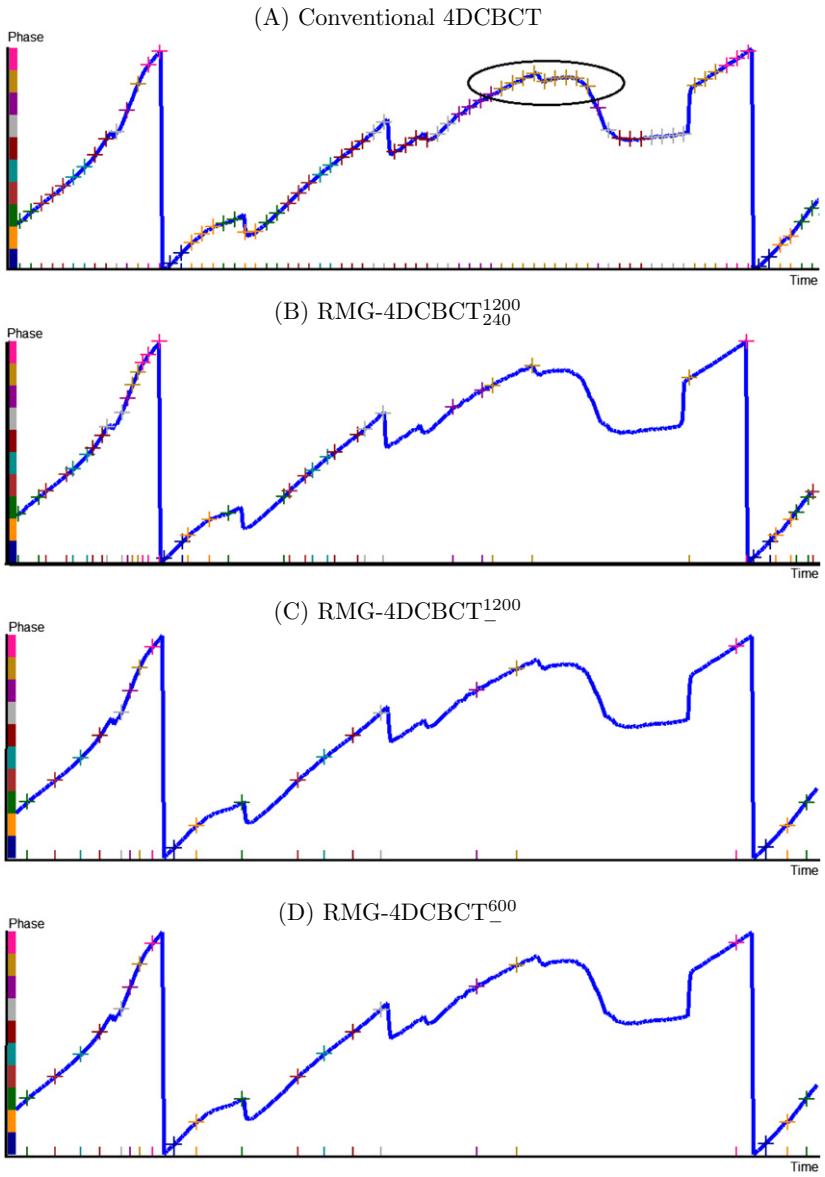

Figure 6. Screen shots of the four different 4DCBCT algorithms studied over a 15 s time period. The coloured marks on the *x*-axis, and the associated coloured crosses on the breathing signal represent the 10 phase bins. (A) Conventional 4DCBCT: constant gantry velocity 4DCBCT collecting 1200 projections in 240 s. This example gives a worst case scenario with a cluster of nine consecutive projections in one bin. (B) RMG-4DCBCT$^{1200}_{240}$: RMG-4DCBCT collecting 120 projections per bin in 240 s. (C) RMG-4DCBCT$^{1200}_{_}$: RMG-4DCBCT collecting 120 projections per bin in 120 respiratory cycles. (D) RMG-4DCBCT$^{600}_{_}$: RMG-4DCBCT collecting 60 projections per bin in 60 respiratory cycles.

multiple projections are acquired in each time window. This is demonstrated in figure 6(A) where we have marked a region where nine consecutive projections are taken in a single time window.

3.2. RMG-4DCBCT$^{1200}_{240}$

Figure 6(B) demonstrates RMG-4DCBCT$^{1200}_{240}$ which attempts to acquire 1200 projections in 240 s; the same number of projections as for conventional 4DCBCT. Some level of projection clustering is expected with RMG-4DCBCT$^{1200}_{240}$ because a patient with a 4 s breathing cycle will acquire, on average, two projections per time window. When comparing conventional 4DCBCT to RMG-4DCBCT$^{1200}_{240}$ it is important to remember that there are two significant differences: (1) RMG-4DCBCT$^{1200}_{240}$ will acquire 120 projections per respiratory bin, conventional 4DCBCT rarely acquires the same number of projections in each respiratory bin, (2) RMG-4DCBCT is based on a representative breathing trajectory, so if the patient breaths faster, or slower, then image acquisition will take less, or more, than 240 s respectively.

3.3. RMG-4DCBCT$^{1200}_{_}$

The remaining variations of the RMG-4DCBCT algorithm collect only one projection in each time window. We use RMG-4DCBCT$^{1200}_{_}$ to represent the case where one projection is taken in each time window with the aim of collecting 120 projections per respiratory bin. This requires a total of 120 respiratory cycles per patient. For a patient with a 4 s breathing period this will take at least 480 s. Figure 6(C) demonstrates this method of acquisition in more detail. We expect very good projection separation but increased image acquisition time.

3.4. RMG-4DCBCT$^{600}_{_}$

One of the aims of RMG-4DCBCT is to reduce the imaging dose to the patient. With better projection separation there is no need to acquire 120 projections per respiratory bin. RMG-4DCBCT$^{600}_{_}$ represents the case where we only acquire 60 projections per respiratory bin in 60 breathing cycles. This is likely to halve the imaging time and radiation dose when comparing RMG-4DCBCT$^{1200}_{_}$ to RMG-4DCBCT$^{600}_{_}$.

3.5. Lung cancer patient breathing traces

We use the 112 free breathing traces from 24 lung cancer patients from a study at Virginia Commonwealth University (VCU) (George *et al* 2006). We have performed a variety of simulations using different values of maximum velocity, acceleration and imaging frequency with the values summarized in table 2.

3.6. Projection clustering metrics

The primary projection clustering metric is the RMS as defined by equation (2) with a smaller value indicating better image quality. We average the RMS for each simulation across the 112 breathing traces to generate the results in our tables. Another important metric is the number of projections collected in each respiratory bin. Conventional 4DCBCT does not guarantee 120 projections in each respiratory bin and for irregular breathers there can be a large range between the respiratory bin with the least and most projections. For RMG-4DCBCT we expect to collect 120 projections per respiratory bin, but due to the jumps in the respiratory signal, section 2.5.3, this is not always the case. For each simulation we record the respiratory bin

Table 2. Maximum velocity, acceleration and imaging frequency used in RMG-4DCBCT simulations. It should be noted that only the values in the three rows are available mechanically possible on existing linac based 4DCBCT systems.

Simulation Name	Max Hz	Max Vel	Max Accel	Justification
Linac low	10	6°/s	1.8°/s^2	Velocity IEC limited. Acceleration lower limit of Boylan *et al* (2011).
Linac mid	10	6°/s	4.3°/s^2	Velocity IEC limited. Acceleration upper limit of Boylan *et al* (2011).
Linac high	10	6°/s	12°/s^2	Velocity IEC limited. Acceleration from TrueBeam.
Linac highest	10	9°/s	12°/s^2	50% increase on IEC velocity. Acceleration from TrueBeam.
C-arm	80	100°/s	200°/s^2	Kuka robot mounted Siemens Zeego.

with the fewest projections and then average this number across the 112 breathing traces. We do the same for the respiratory bin with the most projections. We record these numbers as the average minimum number of projections and the average maximum number of projections.

Although not a projection clustering metric the total imaging time, or the total time that the patient spends on the couch during imaging, is an important metric. If the imaging time is increased with RMG-4DCBCT then clinical acceptance of the method will be hindered.

3.7. Image quality metrics

To test projection clustering and the number of projections on image quality we have used the Catphan phantom to reconstruct CBCT images using Cobra[7]. The reconstruction gives 160 slices (256×256 pixels per slice) spaced 1 mm apart, see figure 7 for examples of the Catphan images. The Catphan phantom allows us to examine the image quality without the added complication of patient to patient variations and enables ground truth comparisons. The full data set of the Catphan phantom consists of 608 half fan projections which were sampled to reconstruct the images for each respiratory bin. For each projection in our simulation, the projection with the closest gantry angle from the Catphan dataset was selected. Images were then reconstructed for each of the 10 respiratory bins and each of the 112 breathing traces giving a total of 1120 CBCT reconstructions.

Our first image quality metric is the streak ratio (Leng *et al* 2008). The streak ratio for a slice, i, is calculated using

$$\mathrm{SR}_i = (\mathrm{TV}(\mathrm{Image}_i) - \mathrm{TV}(\mathrm{GT}_i))/\mathrm{TV}(\mathrm{GT}_i).$$

where $\mathrm{TV}(\mathrm{Image}_i)$ is the total variation for slice i in the reconstructed image and $\mathrm{TV}(\mathrm{GT}_i)$ is the total variation for slice i in the ground truth image. The average streak ratio was obtained by averaging over the 160 slices, 10 respiratory bins and 112 breathing traces (i.e. we computed the mean and standard deviation for the streak ratio over 179 200 slices).

Our second image quality metric is the signal to noise ratio, SNR. We calculate the SNR from two rectangles in slice 55 of the reconstructed Catphan image. The two rectangles are on different intensity disks in the image and are shown in figure 7. The SNR is calculated by dividing the mean intensity by the standard deviation of the intensities of the pixels in each rectangle. A higher value indicates better image quality. The SNR calculation was performed for the 10 respiratory bins and 112 breathing traces to give 1120 SNR values from which the mean and standard deviation in the SNR was calculated.

[7] COBRA, Exxim Computing Corporation, 3825 Hopyard Road, Suite 220, Pleasanton, CA 94588, USA.

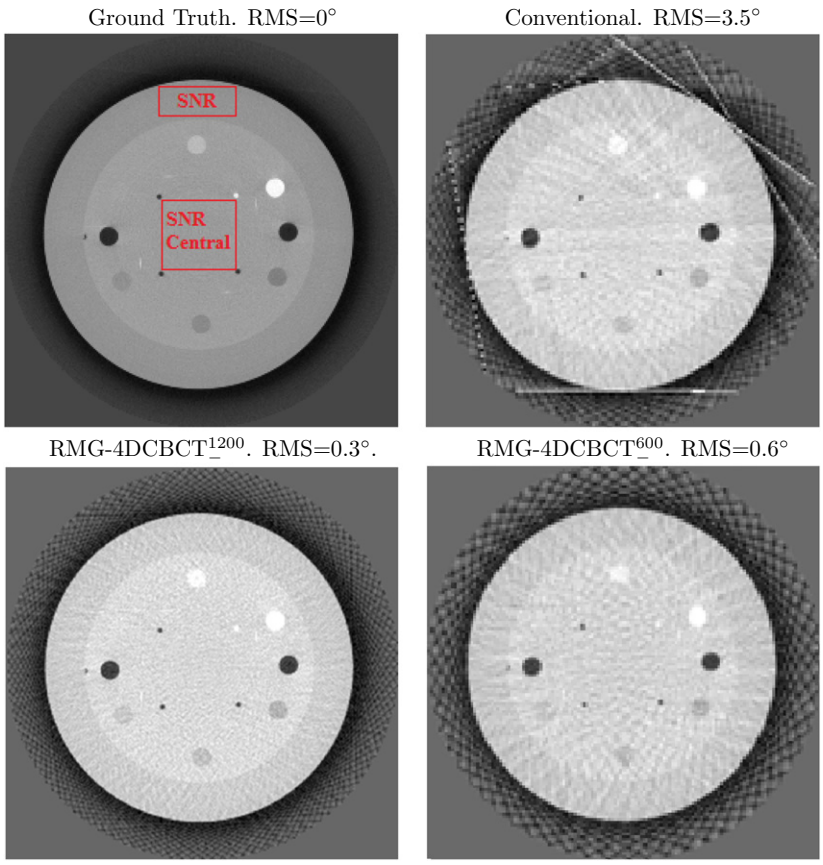

Figure 7. Reconstructed images of the Catphan phantom for the ground truth (608 projections), conventional 4DCBCT (120 projections), RMG-4DCBCT$^{1200}_{_}$ (120 projections), RMG-4DCBCT$^{600}_{_}$ (60 projections) (slice 55 is shown). The two red rectangles in the ground truth image represent the regions used to calculate the signal to noise ratio.

Our final image quality metric is the normalized difference. We calculate a difference image by subtracting the reconstructed image from the ground truth image. We then sum the absolute value of the pixel intensity and divide this number by the sum of the pixel intensity in the ground truth image. The normalized difference is averaged over the 10 respiratory bins and 112 breathing traces (1120 reconstructions in total) and the standard deviation in the normalized difference is calculated.

4. Results

Examples of images reconstructed using the four 4DCBCT methods are given in figure 7. It should be noted that RMG-4DCBCT$^{600}_{_}$ was reconstructed using half the number of projections, and half the imaging dose, than conventional 4DCBCT while the image quality is similar. We will examine both the projection clustering and image quality metrics in the remainder of this section.

Table 3. Comparison between different 4DCBCT algorithms: average of key projection clustering metrics for different 4DCBCT methods across the 112 breathing traces using linac low. These values represent a lower bound of performance that all linacs can achieve.

4DCBCT Algorithm	RMS	Imaging time (sec)	Minimum projections	Maximum projections
RPM phase				
Conventional	3.5°	240	109	134
RMG-4DCBCT$^{1200}_{-}$	0.3°	546	115	126
RMG-4DCBCT$^{600}_{-}$	0.6°	273	57	63
RMG-4DCBCT$^{1200}_{240}$	2.6°	260	111	133
Ruan phase				
Conventional	3.9°	240	81	205
RMG-4DCBCT$^{1200}_{-}$	0.0°	580	120	120
RMG-4DCBCT$^{600}_{-}$	0.0°	290	60	60
RMG-4DCBCT$^{1200}_{240}$	3.0°	243	118	122

Table 4. Comparison between different linac models: average of key projection clustering metrics for RMG-4DCBCT$^{1200}_{240}$ across the 112 breathing traces using a variety of different linac models and the RPM phase signal.

Linac	RMS	Imaging time (sec)	Minimum projections	Maximum projections
Linac low	2.6°	260	111	133
Linac mid	2.6°	260	110	134
Linac high	2.4°	260	111	133
Linac highest	2.4°	260	111	133
C-arm 80 Hz	1.1°	264	108	130

4.1. Projection clustering metrics

Table 3 gives a comparison of the projection clustering metrics using the linac low settings. The RMS is significantly improved for RMG-4DCBCT$^{1200}_{-}$ and RMG-4DCBCT$^{600}_{-}$ when compared to conventional 4DCBCT. However, for RMG-4DCBCT$^{1200}_{-}$ the imaging time is more than double that of conventional 4DCBCT. With both the RPM and Ruan phase, the minimum and maximum number of projections using RMG-4DCBCT has a lower spread than for conventional 4DCBCT so we expect more consistent image quality from bin to bin using RMG-4DCBCT. Using the Ruan phase, which does not have the jumps in the phase signal, the RMS for RMG-4DCBCT$^{1200}_{-}$ and RMG-4DCBCT$^{600}_{-}$ are lower than using the RPM phase indicating that the method used to calculate the real-time phase signal is important. The much larger spread between the minimum and maximum number of projections with the RPM phase signal is also caused by the jumps in the phase signal.

In table 3 the RMS using RMG-4DCBCT$^{1200}_{240}$ is not significantly improved over conventional 4DCBCT. With RMG-4DCBCT$^{1200}_{240}$ on average two projections are required per time window and with the linac low settings for acceleration and velocity the projections cannot be separated enough to reduce the RMS. Table 4 gives a comparison with different linac models using RMG-4DCBCT$^{1200}_{240}$. We can see improvements with increased acceleration of the linac. However, the improvements are small for linac highest and only become significant for the C-arm system.

Table 5. Reducing the imaging time with the C-arm system: average of key projection clustering metrics for RMG-4DCBCT$_T^{1200}$ across the 112 breathing traces using the C-arm and the RPM phase signal. T is the total time allowed in the optimization to acquire 1200 projections.

Imaging time (T sec)	RMS	Minimum projections	Maximum projections
240	1.1°	108	130
200	1.5°	102	137
160	1.9°	94	144
120	3.1°	95	142
80	4.7°	99	139
60	5.5°	103	136

Table 6. Image quality metrics for different 4DCBCT algorithms: mean and standard deviation of key image quality metrics for different 4DCBCT methods across the 10 respiratory bins and 112 breathing traces (1120 reconstructions) using linac low for acceleration and velocity. The results in this table are for the same simulations as in table 3.

4DCBCT algorithm	Streak ratio	Signal to noise ratio—upper	Signal to noise ratio—central	Normalized difference
RPM phase				
Conventional	5.2 ± 3.3	189 ± 55	179 ± 53	1.0 ± 0.9
RMG-4DCBCT$_{-}^{1200}$	1.6 ± 0.2	300 ± 13	291 ± 13	0.3 ± 0.0
RMG-4DCBCT$_{-}^{600}$	2.9 ± 0.9	192 ± 23	172 ± 20	0.5 ± 0.4
RMG-4DCBCT$_{240}^{1200}$	4.3 ± 2.7	194 ± 47	194 ± 47	0.7 ± 0.7
Ruan phase				
Conventional	6.5 ± 3.6	157 ± 65	152 ± 63	1.4 ± 1.1
RMG-4DCBCT$_{-}^{1200}$	1.5 ± 0.0	305 ± 5	296 ± 2	0.2 ± 0.0
RMG-4DCBCT$_{-}^{600}$	2.6 ± 0.0	200 ± 4	179 ± 3	0.4 ± 0.0
RMG-4DCBCT$_{240}^{1200}$	4.2 ± 2.8	206 ± 49	197 ± 48	0.7 ± 0.7

As the C-arm system has a much higher imaging frequency, maximum velocity and maximum acceleration than current generation linacs, we can reduce the total imaging time required to collect 1200 projections. In table 5 we list the projection clustering metrics using the C-arm system and different total imaging times. As we reduce the total imaging time, RMG-4DCBCT is forced to take projections closer together with a much higher gantry velocity and acceleration. As one would expect the RMS increases as the imaging time is reduced because the gantry has less time to move into position for the next projection and more projections are acquired before a jump in the real-time phase signal is detected. The high spread between the minimum and maximum projections indicates that the jumps in the RPM phase signal have a significant impact on projection acquisition and further research on real-time phase estimation will be necessary if C-arm systems are to be used.

4.2. Image quality metrics

Although the projection clustering metrics are useful it is important to establish that a lower RMS leads to better image quality. Table 6 compares the image quality metrics for linac low with different 4DCBCT algorithms. This table confirms that the RMS is a good indicator of

image quality with similar trends to those observed in table 3 also occur in table 6. The most significant result in table 6 is that the signal to noise ratio for RMG-4DCBCT$^{600}_{-}$ is comparable to both conventional 4DCBCT and RMG-4DCBCT$^{1200}_{240}$. This suggests that we can achieve similar image quality with approximately half the projections.

5. Discussion and limitations

We have simulated RMG-4DCBCT using breathing traces from 112 lung cancer patients. Our software has been designed so that once we have an imager where projection acquisition and gantry velocity can be controlled it is relatively easy to replace our simulated imager and gantry with a real imager and gantry.

We have compared RMG-4DCBCT to conventional 4DCBCT using both image quality metrics and projection clustering metrics to demonstrate that RMG-4DCBCT shows promise for improving image quality and reducing radiation dose for both current generation linear accelerators and high end 4DCBCT systems. For current generation linear accelerators the radiation dose can be halved using RMG-4DCBCT$^{600}_{-}$ for similar image quality when compared to conventional 4DCBCT. With the C-arm system, which is capable of much higher gantry acceleration and velocity, the imaging time can be reduced using RMG-4DCBCT.

Active 4DCBCT and respiratory triggered 4DCBCT have recently been published (Fast *et al* 2013) and (Cooper *et al* 2013) respectively. Active 4DCBCT regulates the projection pulse rate but not the gantry speed and has been experimentally implemented by Fast *et al* (2013). Respiratory triggered acquisition maintains a fixed projection pulse rate but discards, or does not take a projection, if a projection has already been acquired in the current respiratory bin (Cooper *et al* 2013). The advantage in controlling the gantry for RMG-4DCBCT is that image acquisition can be completed faster with better projection clustering than methods where just the projection pulse rate are regulated.

This paper has focused on phase binning rather than displacement binning because phase binning is currently used clinically. Displacement binning suffers from baseline drifts and shallow breathing. However, in our previous study, (O'Brien *et al* 2013), we demonstrated that displacement binning has the potential to reduce the total imaging time and improve projection clustering in comparison to phase binning. Overcoming the problems mentioned above with displacement binning would be an advantage for 4D acquisition in general.

The main limitation of RMG-4DCBCT is that it puts more emphasis on real-time estimation of the phase. Although we have demonstrated that the Ruan phase produces a smooth phase signal, the Ruan phase has not been tested clinically. More work on real-time phase estimation is necessary if phase based binning is to be used clinically.

It was demonstrated by O'Brien *et al* (2013) using a more complicated heuristic solution method to compute the gantry trajectory and projection pulse rate interval, that better gantry trajectories are available when the gantry acceleration and velocity are high (e.g. for the C-arm system). Unfortunately, the more complicated heuristic solution method takes several days to find a better solution than the simpler heuristic solution used in this paper. Further work developing a method to optimize the gantry trajectory and projection time interval schedule would further reduce projection clustering for the C-arm system.

6. Conclusions

This is the first study to simulate respiratory motion guided 4DCBCT (RMG-4DCBCT) using breathing traces from lung cancer patients. We have demonstrated that RMG-4DCBCT can be

used to reduce imaging dose and improve image quality when acquiring four dimensional cone beam computed tomography (4DCBCT) images. It has been shown that there is a trade-off between image quality, imaging dose and acquisition time that needs to be balanced for a particular application. For example, for the same image quality RMG-4DCBCT can reduce the imaging dose by up to 50% when compared to conventional 4DCBCT and for the C-arm system studied the imaging time can be reduced to as low as 60 s.

Acknowledgments

Professor PJK would like to acknowledge the support of a National Health and Medical Research Council (NHMRC) Australia Fellowship. This project was supported in part by NHMRC project grant 1034060.

References

Berbeco R I, Mostafavi H, Sharp G C and Jiang S B 2005 Towards fluoroscopic respiratory gating for lung tumours without radiopaque markers *Phys. Med. Biol.* **50** 4481–90

Boylan C J, Rowbottom C G and Mackay R I 2011 The use of a realistic VMAT delivery emulator to optimize dynamic machine parameters for improved treatment efficiency *Phys. Med. Biol.* **56** 4119–33

Cooper B J, O'Brien R T, Balik S, Hugo G D and Keall P J 2013 Respiratory triggered 4D cone-beam computed tomography: a novel method to reduce imaging dose *Med. Phys.* **40** 041901

Fast M, Wisotzky E, Oelfke U and Nill S 2013 Actively triggered 4d cone-beam CT acquisition *Med. Phys.* **40** 091909

Feldkamp L A, Davis L C and Kress J W 1984 Practical cone-beam algorithm *J. Opt. Soc. Am.* A **1** 612–9

George R, Chung T D, Vedam S S, Ramakrishnan V, Mohan R, Weiss E and Keall P J 2006 Audio-visual biofeedback for respiratory-gated radiotherapy: impact of audio instruction and audio-visual biofeedback on respiratory-gated radiotherapy *Int. J. Radiat. Oncol. Biol. Phys.* **65** 924–33

Kavanagh A, Evans P M, Hansen V N and Webb S 2009 Obtaining breathing patterns from any sequential thoracic x-ray image set *Phys. Med. Biol.* **54** 4879–88

Krauss A, Nill S and Oelfke U 2011 The comparative performance of four respiratory motion predictors for real-time tumour tracking *Phys. Med. Biol.* **56** 5303–17

Leng S, Zambelli J, Tolakanahalli R, Nett B, Munro P, Star-Lack J, Paliwal B and Chen G H 2008 Streaking artifacts reduction in four-dimensional cone-beam computed tomography *Med. Phys.* **35** 4649–59

O'Brien R T, Cooper B J and Keall P J 2013 Optimizing 4D cone beam computed tomography acquisition by varying the gantry velocity and projection time interval *Phys. Med. Biol.* **58** 1705–23

Ruan D, Fessler J A, Balter J M and Keall P J 2009 Real-time profiling of respiratory motion: baseline drift, frequency variation and fundamental pattern change *Phys. Med. Biol.* **54** 4777–92

Sonke J J, Zijp L, Remeijer P and van Herk M 2005 Respiratory correlated cone beam CT *Med. Phys.* **32** 1176–86

Sweeney R A, Seubert B, Stark S, Homann V, Muller G, Flentje M and Guckenberger M 2012 Accuracy and inter-observer variability of 3D versus 4D cone-beam CT based image-guidance in SBRT for lung tumors *Radiat. Oncol.* **7** 81

Taguchi K 2003 Temporal resolution and the evaluation of candidate algorithms for four-dimensional CT *Med. Phys.* **30** 640–50

Van Herk M, Zijp L, Remeijer P, Wolthaus J and Sonke J 2007 On-line 4D cone beam CT for daily correction of lung tumour position during hypofractionated radiotherapy *Int. Conf. on the Use of Computer in Radiation Therapy* (Toronto: ICCR)

Vergalasova I, Cai J and Yin F F 2012 A novel technique for markerless, self-sorted 4D-CBCT: feasibility study *Med. Phys.* **39** 1442–51

Zijp L, Sonke J and Herk M 2004 Extraction of the respiratory signal from sequential thorax cone-beam x-ray images *Int. Conf. on the Use of Computer in Radiation Therapy* (Toronto: ICCR) pp 507–9